# Thermodynamic and Kinetic Modeling of Evolution of Mn-Ni-Si-rich Precipitates in Low-Cu Reactor Pressure Vessel Steels

by

Huibin Ke

*A dissertation submitted in partial fulfillment of*

*the requirements for the degree of*

Doctor of Philosophy

(Materials Science and Engineering)

at the

University of Wisconsin- Madison

2017

Date of final oral examination: 04/14/2017

The dissertation is approved by the following members of the Final Oral Committee:

| | | |
|---|---|---|
| Dane Morgan, | Professor, | Materials Science and Engineering |
| Donald Stone, | Professor, | Materials Science and Engineering |
| G. Robert Odette, | Professor, | University of California – Santa Barbara |
| Izabela Szlufarska, | Professor, | Materials Science and Engineering |
| Kumar Sridharan, | Professor, | Engineering Physics |
| Todd Allen, | Professor, | Engineering Physics |

# Abstract

Formation of large volume fractions of Mn-Ni-Si precipitates (MNSPs) causes excess irradiation embrittlement of reactor pressure vessel (RPV) steels at high, extended-life fluences. Thus, a new and unique, semi-empirical cluster dynamics model was developed to study the evolution of MNSPs in low-Cu RPV steels. The model has been developed based on experimental data under irradiation conditions and validated against data on post-irradiation annealing conditions. The model is based on CALPHAD thermodynamics and radiation enhanced diffusion kinetics. The thermodynamics dictates the compositional and temperature dependence of the free energy reductions that drive precipitation. The model treats both homogeneous and heterogeneous nucleation, where the latter occurs on cascade damage, like dislocation loops. The model has only four adjustable parameters that were fit to an atom probe tomography (APT) database. The model predictions are in semi-quantitative agreement with systematic Mn, Ni and Si composition variations in the alloys characterized by APT, including a sensitivity to local tip-to-tip variations even in the same steel. The model predicts that heterogeneous nucleation plays a critical role in MNSP formation in lower alloy Ni contents. Single variable assessments of compositional effects show that Ni plays a dominant role, while even small variations in irradiation temperature can have a large effect on the MNSP evolution. Within typical RPV steel ranges, Mn and Si have smaller effects. The delayed but then rapid growth of MNSPs to large volume fractions at high fluence is well predicted by the model. For purposes of illustration, rather than prediction, the effect of MNSPs on transition temperature shifts are presented based on well-established microstructure-property and property-property models. Solubility of Fe in MNSPs is also investigated with *ab initio* method and is found that the solubility of Fe is less than 1.0% in G-phase formed in typical RPV steels.

## List of Publications

1. **H. Ke**, P. Wells, P. D. Edmondson, N. Almirall, L. Barnard, G. R. Odette and D. Morgan, "Thermodynamic and kinetic modeling of Mn-Ni-Si-rich precipitates evolution in low-Cu RPV steels", *Acta Materialia*, **138** (2017), 10-26. doi:http://dx.doi.org/10.1016/j.actamat.2017.07.021
2. W. Xiong, **H. Ke**, R. Krishnamurthy, P. Wells, L. Barnard, G.R. Odette and D. Morgan, "Thermodynamic models of low-temperature Mn–Ni–Si precipitation in reactor pressure vessel steels", *MRS Communications*, (2014), 101-105. doi: http://dx.doi.org/10.1557/mrc.2014.21
3. P. Wells, **H. Ke**, N. Almirall, D. Morgan, T. Yamamoto and G. R. Odette, "On the thermal stability of features formed in highly irradiated reactor pressure vessel steels", (*in preparation*)
4. X. Bai, **H. Ke**, Y. Zhang and B. W. Spencer, "Modeling copper precipitation hardening and embrittlement in a dilute Fe-0.3 at.% Cu alloy under neutron irradiation", (*submitted to Journal of Nuclear Material*)
5. J. H. Ke, **H. Ke** and D. Morgan, "Cluster dynamics modeling of Mn-Ni-Si-rich precipitates in ferritic-martensitic alloy T91 under irradiation", (*submitted to Journal of Nuclear Material*)
6. M. Mamivand, P. Wells, **H. Ke**, G. R. Odette and D. Morgan, "Cluster dynamics modeling of coupling of Cu-rich and Mn-Ni-Si-rich precipitates in RPV steels", (*in preparation*)

## List of Conference Presentations

1. **H. Ke**, L. Barnard, D. Morgan, P. Wells, N. Almirall and G. R. Odette, "*Thermodynamic and kinetic modeling of Mn-Ni-Si precipitates in low-Cu RPV steels*", **invited** talk to be presented in Fall MRS Meeting and Exhibit, (Boston, MA, November, 2017)
2. **H. Ke**, L. Barnard, D. Morgan, P. Wells, N. Almirall and G. R. Odette, "*Thermodynamic and kinetic modeling of Mn-Ni-Si precipitates in low-Cu RPV steels*", **invited** talk presented in ATR-2 meeting, (Santa Barbara, CA, January, 2017)
3. **H. Ke**, L. Barnard, D. Morgan, P. Wells and G. R. Odette, "*Thermo-kinetics modeling of Mn-Ni-Si precipitates in low-Cu RPV steels*", talk presented in the 19th International Group of Radiation Damage Mechanism (IGRDM), (Asheville, NC, April 2016)
4. **H. Ke**, L. Barnard, D. Morgan, P. Wells and G. R. Odette, "*Thermo-kinetics modeling of multi-phase Mn-Ni-Si precipitates in low Cu RPV steels*", poster presented in TMS Annual Meeting & Exhibition, (Nashville, TN, February 2016)
5. **H. Ke**, L. Barnard, D. Morgan, P. Wells and G. R. Odette, "*Cluster dynamics modeling of multi-phase Mn-Ni-Si-Rich precipitation evolution in low Cu RPV steels*", talk presented in Spring MRS Meeting and Exhibit, (San Francisco, CA, April 2015)
6. **H. Ke**, L. Barnard, D. Morgan, P. Wells and G. R. Odette, "*Cluster dynamics modeling of multi-phase Mn-Ni-Si-Rich precipitation evolution in low Cu RPV steels*", talk presented in TMS Annual Meeting & Exhibition, (Orlando, FL, March 2015)
7. **H. Ke**, W. Xiong, L. Barnard, D. Morgan, P. Wells, N. Almirall and G. R. Odette, "*Mn-Ni-Si-rich precipitation modeling in reactor pressure vessel (RPV) steels*", talk presented in the 18th International Group of Radiation Damage Mechanism (IGRDM), (Tokyo, Japan, November 2014)

8. **H. Ke**, W. Xiong, L. Barnard, D. Morgan, P. Wells, N. Almirall and G. R. Odette, "*Combined first-principle and CALPHAD modeling of Mn-Ni-Si-rich precipitation in RPV steels*", talk presented in TMS Annual Meeting & Exhibition, (San Diego, CA, February 2014)
9. **H. Ke**, W. Xiong, L. Barnard, D. Morgan, P. Wells, N. Almirall and G. R. Odette, "*CALPHAD and cluster dynamics modeling of Mn-Ni-Si rich precipitates in RPV steels*", talk presented in the 17th International Group of Radiation Damage Mechanism (IGRDM), (Les Embiez, France, May 2013)
10. **H. Ke**, W. Xiong, G. R. Odette and D. Morgan, "*Modeling of Mn-Ni-Si precipitation in reactor pressure vessel steels*", poster presented in TMS Annual Meeting & Exhibition, (San Antonio, TX, March 2013)

# Acknowledgement

First and foremost, I would like to express my deepest gratitude to my advisor Prof. Dane Morgan, who has always been patient and supportive during my 5+ years of Ph.D. study, who gave me advice not only on how to progress with my research project, but also on my career plan and how to work more professionally. I really appreciate his guidance on preparing myself to transit from a student to an independent researcher. Prof. Morgan's abilities to quickly see the key parts of problems, to estimate the order of a physical value in seconds, and to manage his time so efficiently have always impressed me.

I would also like to express my sincere gratitude to Professor G. Robert Odette from University of California - Santa Barbara (UCSB), who gave me invaluable guidance on almost every piece of this work and tremendous encouragements during my research. This work could not have been done without his knowledge and insights in the area based on his study in this area for tens of years. I'm grateful that I could have this opportunity to work closely with Prof. Odette during my Ph.D. study.

I would also like to thank Prof. Izabela Szlufarska. As a woman in engineering and academic world, she sets a perfect model for me to learn from, from her dedication to research to her great appetite of dressing.

I would also like to thank Dr. Leland Barnard, who mentored me tremendously during the first three years of my Ph.D. study. Without his help, I could not have entered the role of a graduate student that smoothly when I first came to UW-Madison.

I would also like to thank Dr. Peter Wells and Nathan Almirall from UCSB, and Dr. Philip Edmondson and Dr. Randy Nanstad from Oak Ridge National Laboratory (ORNL) for providing the experimental data shown in this work, without which this model could not have been

developed. I really appreciate their timely and patient explanations to every question I had. I would also like to thank Dr. Takuya Yamamoto from UCSB for discussions on radiation enhanced diffusion model and precipitate hardening model. I would also like to thank my previous and current team members, Dr. Wei Xiong, Dr. Jia-hong Ke, Dr. Mahmood Mamivand and Dr. Shipeng Shu for their fruitful discussions with me and warm encouragements to me.

I greatly appreciate the time and support from my thesis committee, Prof. Dane Morgan, Prof. Donald Stone, Prof. G. Robert Odette, Prof. Izabela Szlufarska, Prof. Kumar Sridharan and Prof. Todd Allen.

This work could not have been done without the funding support by the US Department of Energy Office of Nuclear Energy's Light Water Reactor Sustainability Program, Materials Aging and Degradation Pathway and the DOE Office of Nuclear Energy's Integrated Research Project (IRP) under contract DE-NE0000639.

Finally, I would like to express my sincere gratitude to my family and friends. It is their love and encouragements that has been keeping me persisting on what I do.

# List of Figures

# List of Tables

# List of Terminology

| | |
|---|---|
| APT | Atom probe tomography |
| BWR | Boiling Water Reactor |
| CALPHAD | CALculation of PHAse Diagram |
| CD | Cluster dynamics |
| CNGT | Classical nucleation and growth theory |
| CNT | Classical nucleation theory |
| LWR | Light water reactor |
| MNS | Mn-Ni-Si |
| MNSP | Mn-Ni-Si precipitates |
| PF | Phase field |
| PIA | Post irradiation annealing |
| PSD | Particle size distribution |
| PWR | Pressurized Water Reactor |
| RIS | Radiation induced segregation |
| RPV | Reactor pressure vessel |

# Table of Contents

# Chapter 1 Introduction

## 1.1 Reactor Pressure Vessel

Nuclear power contributes about 19.5% of the electricity supply in the United States [1], and about 13% worldwide [2]. Figure 1-1 shows the number of reactors by age in United States as of 2016. As can be seen from the figure, the age of a majority of the nuclear reactors are of 30-50 years, and there are only 4 new reactors currently under construction [3]. Therefore, if this major source of carbon-free energy is to be sustained, life extension of the current fleet of light water reactors will be required to bridge the gap to new builds [4]. Life extension will require clear demonstration of large safety margins and reliable and economic long-term plant operation. A key challenge is understanding and managing a large number of materials aging and degradation issues, ranging from concrete and cables to reactor internals to pressure boundary steels [5–9]. Thus extensive aging research is being conducted to support extending plant life from 40 (the original license) and 60 years (the first license extension), and now to 80 years, or more, based on a second license extension.

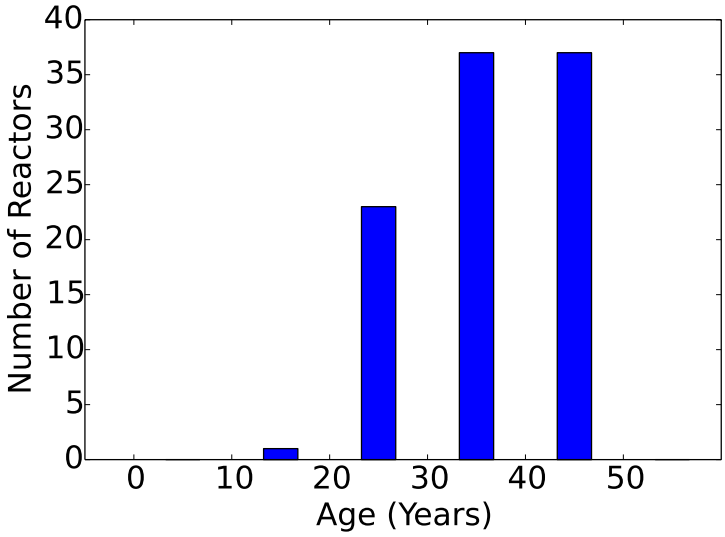


Figure 1-1 Number of reactors by age in United States as of 2016

One critical life extension issue is neutron irradiation embrittlement of reactor pressure vessels (RPVs). RPVs are massive, thick-walled, permanent structures, whose primary function is to pressurize water to 7 (Boiling Water Reactors, BWRs) to 14 MPa (Pressurized Water Reactors, PWRs), thereby permitting reactor operating temperatures around 290°C [10].

Typical RPV base metals used in USA are A302B, A533B plates, or A508 forgings, which are quenched and tempered, low-alloy steels with primarily tempered bainitic microstructures. Other vessel materials in common use include 22NiMoCr37 and 20MnMoNi55 in Germany, and 16MnD5 in France [11]. Compositions of these materials are listed in Table 1-1.

Table 1-1 Chemical requirements - main ferritic materials for reactor components in western countries [11]

| Designation | Elements (wt. %) | | | | | | | | | |
|---|---|---|---|---|---|---|---|---|---|---|
| | C | Si | Mn | P | S | Cr | Mo | Ni | V | Cu |
| ASTM A 302B | max | 0.15 | 1.15 | max | max | | 0.45 | | | |
| | 0.25 | 0.30 | 1.50 | 0.035 | 0.040 | | 0.60 | | | |
| ASME A 508 Cl | max | 0.15 | 0.50 | max | max | 0.25 | 0.55 | 0.50 | max | |
| 2 (1971) | 0.27 | 0.35 | 0.90 | 0.025 | 0.025 | 0.45 | 0.70 | 0.90 | 0.05 | |
| ASME A533 GR | max | 0.15 | 1.15 | max | max | | 0.45 | 0.40 | | |
| B (1971) | 0.25 | 0.30 | 1.50 | 0.035 | 0.040 | | 0.60 | 0.70 | | |
| ASME A508 Cl 2 | max | 0.15 | 0.50 | max | max | 0.25 | 0.55 | 0.50 | max | max |
| (1989) | 0.27 | 0.40 | 1.00 | 0.015 | 0.015 | 0.45 | 0.70 | 1.00 | 0.05 | 0.15 |
| ASME A 508 Cl | max | 0.15 | 1.20 | max | max | max | 0.45 | 0.40 | max | |
| 3 (1989) | 0.25 | 0.40 | 1.50 | 0.015 | 0.015 | 0.25 | 0.60 | 1.00 | 0.05 | |
| 16 MnD5 RCC-M | max | 0.10 | 1.15 | max | max | | 0.45 | 0.40 | | |
| 2111 | 0.22 | 0.30 | 1.60 | 0.02 | 0.012 | 0.25 | 0.57 | 0.80 | 0.01 | 0.20 |
| 18 MnD5 RCC-M | max | 0.10 | 1.15 | max | max | max | 0.45 | 0.50 | max | max |
| 2112 (1988) | 0.20 | 0.30 | 1.55 | 0.015 | 0.012 | 0.25 | 0.55 | 0.80 | 0.01 | 0.20 |
| 20 Mn Mo Ni 5 5 | 0.17 | 0.15 | 1.20 | max | max | max | 0.40 | 0.50 | max | max |
| (1983, 1990) | 0.23 | 0.30 | 1.50 | 0.012 | 0.008 | 0.20 | 0.55 | 0.80 | 0.02 | 0.12 |
| 22Ni Mo Cr 3 7 | 0.17 | 0.15 | 0.50 | max | max | 0.25 | max | 0.60 | max | max |
| (1991) | 0.23 | 0.35 | 1.00 | 0.012 | 0.008 | 0.50 | 0.60 | 1.20 | 0.02 | 0.12 |

Two basic methods of RPV fabrication have been used [12]. The first method used rolled and welded plates to form separate shell courses. Thus, an RPV fabricated in this manner has both

longitudinal (axial) and circumferential (girth) weld seams. In some of the older (pre-1972) PWR RPVs, these longitudinal seams are of particular concern for RPV integrity due to high levels of Cu in the welds. All BWR and most of the PWR RPVs used this rolled and welded plate construction. The second fabrication method used large ring forgings. Due to its smaller size, the PWR RPV can be constructed entirely from forge rings, flanges and nozzles. This method provides improved component reliability because of the lack of longitudinal welds. Newer PWRs (post-1972) were fabricated by this method.

Weld compositions differ from the base metal, and may vary significantly even within the same weld. Representative chemical analyses of the plates, welds and forgings are shown in Table 1-2.

Table 1-2 Typical chemical compositions of RPV materials, wt.%

| Product | C | Mn | Si | S | P | Cu |
|---|---|---|---|---|---|---|
| Plate | 0.09-0.17 | 1.04-1.32 | 0.10-0.60 | 0.02-0.04 | 0.01-0.04 | 0.03-0.15 |
| Forgings | 0.18 | 1.30 | 0.36 | 0.024 | 0.024 | 0.10 |
| Manual metal arc weld | 0.086 | 0.91 | 0.42 | 0.022 | 0.025 | 0.08 |
| Submerged-arc weld | 0.088 | 1.49 | 0.52 | 0.037 | 0.031 | 0.23 |

RPVs are also an important barrier to the release of radioactivity in the event of a core damaging accident. Regulations require very low RPV failure probabilities by crack propagation, both for normal operation and postulated low probability accident events. In the unirradiated condition, low alloy RPV steels are very tough, and vessel fracture probabilities are negligibly small, representing no significant risk. However, neutrons leaking from the reactor core cause irradiation hardening and embrittlement, manifested as upward shifts in the ductile-to-brittle transition temperature, $\Delta T$, that may challenge continued safe vessel operation for some plants during extended life.

The embrittlement of RPVs can be classified into two categories: non-hardening and hardening. Both types shift the ductile-brittle-transition-temperature (DBTT) up [13]. Non-hardening embrittlement is usually caused by the segregation of solutes, such as P, to grain boundaries and the interfaces between precipitates and matrix. Hardening embrittlement can be caused by the evolution of defect clusters or dislocation loops caused by irradiation, the evolution of different kinds of precipitates. Modern impurity restrictions on P make the non-hardening embrittlement less relevant.

Current embrittlement regulations are based on correlations of surveillance data for a large number of RPV steels irradiated at low flux in operating reactors[1]. However, current $\Delta T$ models are valid only up to about one half the peak neutron fluence that would be experienced by some vessels in the PWR fleet under extended life operation, which is about $1x10^{24}$ $n \cdot m^{-2}$ at 80 years (for a flux of $\approx 5 \times 10^{14} n \cdot m^{-2} s^{-1}$). Notably, current regulatory models under-predict test reactor $\Delta T$ for these extended-life fluences in high flux test reactor experiments [14,15].

### 1.2 Mn-Ni-Si-rich precipitates

It has been proposed that the under-prediction of $\Delta T$ by current regulatory models is due to the emergence of slowly developing hardening and embrittlement mechanisms at high fluence [14]. The most important mechanism is nucleation and growth of Mn-Ni-Si precipitates (MNSPs), as long ago predicted by Odette and co-workers [16–19]. This early work extended previous studies by Odette that demonstrated and modeled hardening and embrittlement mechanisms associated with the rapid formation of nm-scale coherent Cu precipitates that act as obstacles to

[1] RPVs are basically one-of-a-kind individually built structures, with a wide range of steel metallurgical variables (composition, start of life microstructure and product form) that are exposed to a range of irradiation variables (neutron flux, fluence, spectrum and temperature). Embrittlement is controlled by synergistic interactions between these variables acting in combination.

dislocation glide [20]. Researchers soon recognized that the copper rich precipitates (CRPs) are highly alloyed with Mn and Ni [16,17]. Mn-Ni synergisms rationalized the strong effects of the alloying element Ni, as well as impurity Cu, on hardening and embrittlement [18]. In the early 1990s Odette and coworkers carried out CALPHAD [16] based thermodynamic calculations, suggesting that Mn-Ni precipitates could form even in low Cu steels, which would otherwise be relatively insensitive to embrittlement. The Mn-Ni precipitates were predicted to be slow to nucleate and grow, thus they were dubbed late blooming phases (LBP) at that time.

These models equilibrated Mn, Ni and Cu in solution with these solutes in a specified number density of CRPs and included the effects of composition on the interface energy [16]. At sufficiently high Ni and at lower temperatures, the precipitates contain more Mn and Ni than Cu. This mean-field thermodynamic modeling was later extended to include Si in Lattice Monte Carlo (LMC) simulations, based on pair-bond energy estimates extracted from CALPHAD, that predicted Cu-rich core and Mn-Ni-Si-rich shell precipitate structures [18]. Such core shell structures were also observed in atom probe tomography studies [21–24]. The early models predicted that low irradiation temperatures, high Ni and even small amounts of Cu enhance the formation of Mn-Ni and MNSPs. It was also envisioned that MNSPs heterogeneously nucleate on small Cu-Mn-Ni-Si-defect cluster complexes that form in displacement cascades. These complexes are referred to as stable matrix features (SMF). The SMF, that are thought to be precursors to MNSPs, are responsible for low-to-intermediate fluence embrittlement in low Cu (< 0.07 wt.%) steels prior to the development of well-formed MNSPs which evolve from them. Since there is much more Mn + Ni + Si (typically > 2.5 at.%) in RPV steels than Cu (effectively less than 0.25 at%), large mole fractions ($f$) of MNSPs can produce correspondingly large amounts of hardening and embrittlement, that roughly scale with $\sqrt{f}$.

The early models led to a systematic search for MNSPs, especially as part of the UCSB IVAR program [25]. Further, Auger and Pareige et al. [26–28] observed dilute solute-defect clusters (Cu, Ni, Mn, Si, P, …) in French RPV steels at fluence as low as $2.5\times10^{23}m^{-2}$. As noted above, Odette has long argued that these clusters are the likely precursors to well-formed precipitates [29]. An important advance, reported by Odette in 2004, was the first observation MNSPs in a Cu-free split-melt RPV steel [30]. However, MNSPs are now widely observed in test reactor [21,23,24,31,32] and surveillance [33,34] irradiations. It is no longer a question of if LBP MNSPs will develop, but rather to what extent they will develop as a function of flux, fluence, temperature, and alloy composition. Remarkably, however, MNSPs are not accounted for in current regulatory models [15].

Some aspects of the formation of these MNSPs are still under debate. In particular, the issues include: 1) whether these MNSPs are irradiation *induced* or *enhanced*; 2) whether these precipitates should be called *late* blooming phases (LBP). Regarding the first issue, simulations [35,36] and experiments [37–42] show the segregation of Mn, Ni, and Si elements to sinks, including both defect clusters produced by cascades and network dislocations. For example, Meslin [43] observed a high number density of Mn-rich clusters in an under-saturated Fe-1at.%Mn alloy after ion irradiation. These results seem to indicate the Mn clusters are irradiation *induced*, and driven by radiation induced segregation (RIS), especially the known strong enhancement of Mn transport via interstitials [44,45]. However, it is important to point out that RIS is highly rate dependent, due to the balance of solute fluxes to and from the sink. Thus RIS clusters that form under ion irradiation may not be present in lower dose rate neutron conditions. Further, defect accumulation would occur at the precipitates if vacancies and self-interstitial atoms (SIA) do not accumulate at the MNSPs in equal numbers, leading to observable loops or nanovoids at these

sites. Such features are not observed in association with large mole fractions (*f*), average sizes $\bar{r}$ and number densities (*N*) of MNSPs.

In support of the MNSPs being radiation *enhanced*, we note that a large volume fraction of MNSPs is indeed predicted at thermodynamic equilibrium by a CALPHAD database [46], and identified as G and $\Gamma_2$ diffracting phases in x-ray scattering studies at high fluence [47]. Moreover, these precipitates also survive long term post-irradiation annealing at 425°C, which is much higher than the irradiation temperature around 290°C, where they are obviously much more stable [48]. These factors indicate the large volume fractions of precipitates are thermally stable phases and are irradiation *enhanced*.

Nevertheless, the fact that the large volume fractions of precipitates found at high fluence are enhanced does not mean RIS is unimportant, or that associated radiation induced mechanisms are not active. Due to the small driving force to form MNSPs, segregation to sinks is likely to play an important role in nucleation stage, especially in low and intermediate solute content alloys. Messina [49] recently proposed that dislocation loops generated in cascade might act as nucleation sites for Mn-Ni precipitates. The key hypothesis is that solute segregation at loops reduces their mobility, with the result that the loop number density is similar to those of the MNSPs. However, Messina's work does not treat either segregation or solute clustering directly, so the model does not predict the observed sizes and mole fractions of MNSPs. Logically, even if RIS plays an important role in MNSP nucleation, it does not mean that they are not thermally stable phases in intermediate and high solute alloys. On the other hand, the fact that the MNSPs are stable phases at high fluence in many alloys does not mean they cannot be nucleated by RIS mechanisms, particularly in lower solute alloys.

Regarding the second issue, the term LBP is used to highlight the role of MNSPs in comparison to Cu precipitates, which form and saturate at very low fluence compared to MNSPs. The scaling factor for indexing precipitation on a fluence or dpa scale ranges from 6 to more than 50 times less for CRPs than MNSPs. Thus the term LBP does not mean that MNSPs precursors are not formed at low fluences (order $10^{23}$n-m$^{-2}$), where they are observed in the form of cascade solute cluster complexes. Rather the argument is they only form large volume fraction at high fluences compared to Cu [24,32].

## 1.3 Theory on precipitation reactions and hardening

### 1.3.1 Precipitation thermodynamics and kinetics

Precipitation transformations can be expressed in reaction terms as follows

$$\beta' \rightarrow \alpha + \beta \qquad (1\text{-}1)$$

where $\beta'$ is a metastable supersaturated solid solution, $\alpha$ is a stable or metastable precipitate, and $\beta$ is a more stable solid solution with the same crystal structure as $\beta'$, but with a composition closer to equilibrium.

One can basically divide the general sequence of forming a two phase alloy from a single phase into three steps: 1) Nucleation; 2) Growth of the nuclei or particles; 3) Coarsening (Ostwald ripening). Please note such a separation into three distinct steps is artificial. Nucleation of the second phase occurs since the energy of the single phase system can be reduced by forming regions of the second phase. Nanometer-sized precipitates of the new phase thus appear. Growth of nuclei then proceeds due to heat diffusion away from the nucleus into the matrix or mass diffusion from the matrix to the nuclei. This results in dispersion of second phase particles in a matrix. Coarsening, also called Ostwald ripening or competitive growth, then occurs when large particles grow at the expense of small particles [50].

The formation energy of a precipitate is given by

$$\Delta G = -V\Delta G_V + \sum \gamma_i A_i \quad (1\text{-}2)$$

where $V$ is the volume of the precipitate, $-\Delta G_V$ is the bulk formation energy of the precipitate per unit volume, $\gamma_i$ is the surface energy of surface $i$ of the precipitate and $A_i$ is the area of surface $i$.

If we ignore the variation of γ with interface orientation and assume the precipitate is spherical with a radius of curvature $r$, then Eq. ( 1-2 ) becomes

$$\Delta G = -\frac{4}{3}\pi r^3 \Delta G_V + 4\pi r^2 \gamma \quad (1\text{-}3)$$

This is shown as a function of $r$ in Figure 1-2. Differentiation of Eq. ( 1-3 ) yields the critical radius $r^*$

$$r^* = \frac{2\gamma}{\Delta G_V} \quad (1\text{-}4)$$

Precipitates are at unstable equilibrium state when they are at the size of critical radius, which means a small disturbing can cause the nucleus either grow or shrink. When the size of a precipitate is larger than critical radius, its formation energy will decrease as it grows, thus it will tend to grow. When the size of a precipitate is smaller than critical radius, its formation energy will decrease as it shrinks, thus it will tend to shrink.

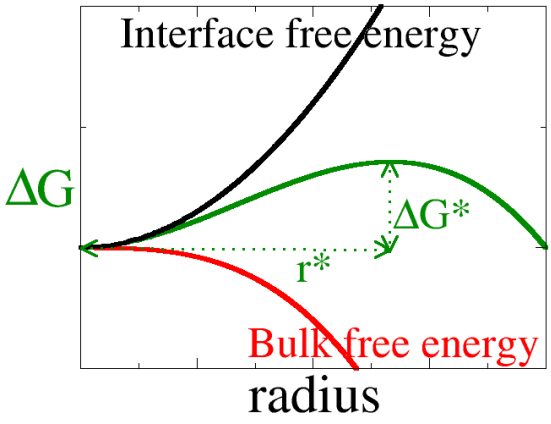


Figure 1-2 Formation energy of a nucleus as a function of nucleus radius [51]

1.3.2 Precipitation hardening

Precipitates can cause hardening of alloys by impeding the motion of dislocations, which manifests as an increase in the yield stress. Depending on the critical resolved shear stress, the dislocations can interact with precipitates with two different mechanisms. Usually, for a certain material, when the precipitates are small, the dislocation lines will cut through the precipitates, as shown in Figure 1-3 a), while when the precipitates are large enough, the dislocation lines will loop around the precipitates, as shown in Figure 1-3 b). The critical resolved shear stress at which the dislocation overcomes the precipitates depends on the one hand highly on the nature of the precipitates. Its size, coherency with associated with coherency strains, crystal structure and chemical characteristics determine the ease and also the manner of the passage. On the other hand, the distribution and concentration of precipitates is also relevant.

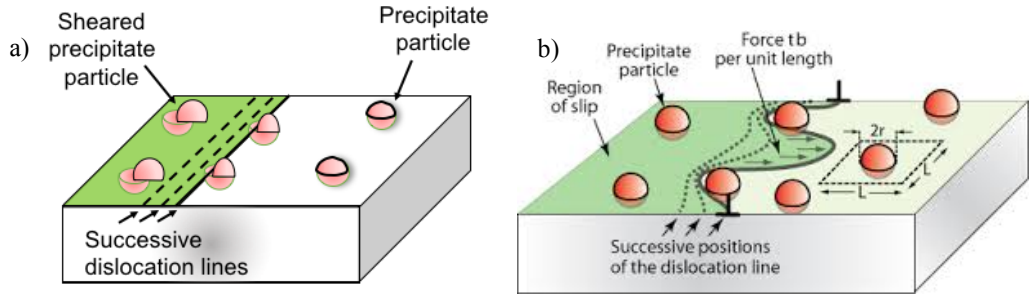


Figure 1-3 Schematic plot of two different interaction mechanisms between precipitates and dislocations. a) Particle shearing; b) Particle by-pass (Orowan) [52]

For a certain material, depending on the interaction mechanisms between dislocation lines and precipitates, the increase of the yield stress will relate to the precipitates size and volume fraction via different equations. As shown in Figure 1-4, when the precipitates are small, the cutting mechanism dominates, and the yield stress increases as the radius of precipitates increases, however, when the precipitates are large, the bowing mechanism will dominate, thus the yield stress decreases as the radius of precipitates increases. And there will be a critical radius at which

maximum strengthening occurs. The governing equations for these different mechanisms are summarized in the following paragraphs.

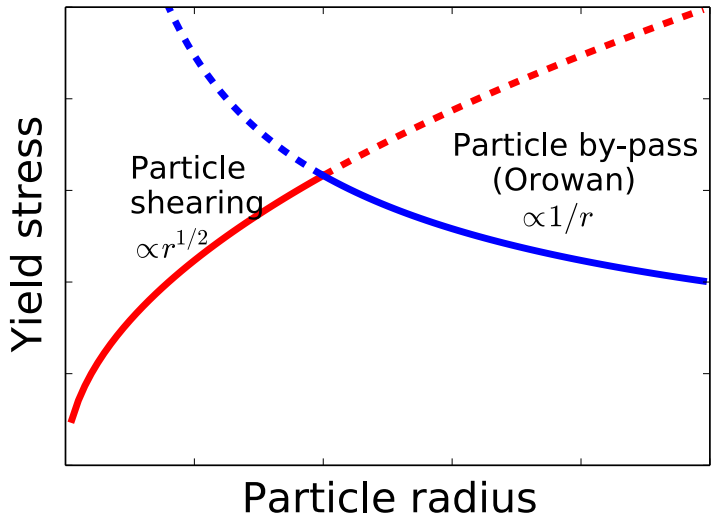


Figure 1-4 Schematic plot of increase of yield stress caused by precipitates as a function of particle size by different mechanisms: a) particle shearing; b) particle by-pass by glide dislocations

1.3.2.1 Particle shearing

When the precipitates are small, they will be sheared by dislocations when dislocations glide through. The yield stress in this case can be expressed by

$$\Delta\sigma_y = \frac{F^{\frac{3}{2}}}{bL}(2T)^{1/2} \quad (1\text{-}5)$$

where F is the obstacle strength, b is Burger's vector, T is the dislocation line tension, which is usually taken as $1/2\mu b^2$, and L is square lattice spacing between the particles, which is equal to $N_s^{-1/2}$, and $N_s$ is the number of particles per unit are of slip plane, which is calculated by Friedel statistics [53]

$$N_s = \frac{3f}{2\pi r^2} = 2N_v r \quad (1\text{-}6)$$

Thus, combining Eq. (1-5) and Eq. (1-6), the yield stress can be expressed as

$$\Delta\sigma_y = \frac{2F^{\frac{3}{2}}}{b}(TN_v r)^{1/2} \quad (1\text{-}7)$$

1.3.2.2 Orowan hardening mechanism

When the particle size is large enough, these particles can't be sheared by dislocations, instead they will be bypassed and looped around by dislocations, which is called the Orowan mechanism. Wagner [54] summarized several models that were proposed to relate hardening with the characteristics of the cluster distribution. These include the dispersed-barrier hardening (DBH) model [55] in the simplest version, Eq. ( 1-8 ), and in the advanced version according to Bacon, Kocks and Scattergood (BKS) [56], Eq. ( 1-9 ), and the Russell-Brown model [17,57], Eq. ( 1-10) for strong obstacles.

$$\Delta\sigma_y = \alpha MGb\sqrt{Nd} \qquad (1\text{-}8)$$

$$\Delta\sigma_y = \frac{MGb}{2\pi L}\left[\ln\left(\frac{L}{b}\right)\right]^{-1/2}\left[\ln\left(\frac{d'}{b}\right)+0.7\right]^{3/2} \qquad (1\text{-}9)$$

with $L = \frac{1}{\sqrt{Nd}}$ and $d' = \frac{dL}{d+L}$

$$\Delta\sigma_y = \frac{MGb}{L}\left\{1-\left[C_1 - C_2\ln\left(\frac{d}{b}\right)\right]^2\right\}^{3/4} \qquad (1\text{-}10)$$

with $L = \frac{\sqrt{\pi}}{2}\frac{d}{\sqrt{f_v}}$

Here, $M$=3.06 is the Taylor factor [58], $G$=83GPa the shear modulus and $b$=0.248nm the Burgers vector [57]. $C_1$ and $C_2$ are two parameters related to the inner and outer cut-off radius used to calculate the energy of the dislocation, and the energy per unit length of a dislocation in infinite media. And $L$ is the spacing between precipitates, $d$ is the diameter of precipitates and $N$ is the number density of precipitates.

By all these relations above, the increase of yield stress can be summarized as

$$\Delta\sigma_y \propto MGb\frac{\sqrt{f}}{r} \qquad (1\text{-}11)$$

An alternative hardening relationship was also developed by Friedel-Kroupa-Hirsch (FKH) for weak obstacles [58,59], Eq. (1-12), where the effective interparticle spacing is increased

compared to planar geometric spacing due to less extensive dislocation bowing prior to obstacle breakaway.

$$\Delta\sigma_y = \frac{MGb}{8} dN^{2/3} \quad (1\text{-}12)$$

Hardening caused by precipitates increases the strength of alloys, and it is one of the common ways in alloy design. However, as the strength of the alloy increases, the ductility of the alloy will decrease. Thus, in some cases, as for the formation of Mn-Ni-Si precipitates in RPV steels, hardening caused by the precipitates can cause the embrittlement of material.

## 1.4 Overview of this thesis

The motivation for this study is to develop a rigorous physical model for LBP MNSPs in low-Cu RPV steels based on the underlying thermodynamics and kinetics. The model can be used to better understand the factors controlling MNSPs evolution and support prediction of alloy embrittlement under light water reactor (LWR) life-extension conditions.

A cluster dynamics (CD) master equation model of the evolution of the size ($r$), number density ($N$) and mole fraction ($f$) of MNSPs as a function of fluence, flux, temperature and alloy composition has been built. The thermodynamic terms in the master equation coefficients are extracted from a CALPHAD database. The model assumes that the MNSPs have the equilibrium compositions of either G ($Ni_{16}Si_7Mn_6$) or $\Gamma_2$ ($Mn(Ni,Si)_2$) phases. These are the two stable phases in the Mn-Ni-Si ternary projection of the Fe-Mn-Ni-Si quaternary system that are predicted by the CALPHAD database for the compositions studied in this work at around 300°C. The kinetic terms in the CD model are based on radiation-enhanced adjustments of the estimated thermal solute diffusion coefficients, as determined by conventional reaction diffusion equations and semi-empirical flux scaling. Heterogeneous MNSP formation on the cascade cluster complexes, as noted above, is included adding to homogeneous nucleation. The results of the CD model are compared

to detailed atom probe tomography (APT) data. The interface energies, heterogeneous nucleation site size and cascade cluster production efficiency factor are the main fitting parameters.

The model can be used to interpolate and extrapolate the experimental database on RPV steels, which is both sparse and not well distributed in the high dimensional space of potentially relevant variables. The CD models also provide a foundation for more realistic but complex models, e.g., including Cu and MNSPs, and simpler, but still physical, reduced order models like Avrami-based treatments of the MNSPs evolution as a function of fluence.

The thesis is organized as follows. Chapter 2 describes the computational models and sub models. In this chapter, we also briefly introduce other meso-scale computational methods besides cluster dynamics model and compare the advantages and disadvantages of each method. Chapter 3 presents the experimental database, including APT data under irradiation, and APT data and hardening data under post-irradiation annealing. Chapter 4 presents the thermodynamic results of the study by CALPHAD method. Chapter 5 shows the investigation of Fe solubility in MNSPs forming in bcc-Fe with *ab initio* method. Chapter 6 presents the CD results for under irradiation conditions, which compares the CD model predictions to the APT results, applies the model to predict the effects of selected variations in alloy composition and irradiation temperature on the fluence dependence of the evolution of MNSPs, analyzes the corresponding effects of composition and temperature on MNSP mole fraction at specified fluences and temperatures in terms of composition cross-plots for the entire CD database, and illustrates the effects of MNSPs on hardening and embrittlement for typical RPV steels during life-extension based on existing microstructure-property-property models. Chapter 7 presents the results from CD under pos-irradiation annealing conditions and compares to available experimental data. A brief summary and conclusions and suggestions for future work are presented in Chapter 8.

# Chapter 2 Computational Methods and Techniques

## 2.1 Introduction on mesoscale modeling

It is well known that many materials processes take place over a wide range of length and time scales. Although innovative multiscale modeling approaches have been proposed for modeling multiple scale processes in many complex multicomponent materials systems, the straightforward information passing from one scale to another is still the main approach in the foreseeable future. The formation of precipitates usually goes through different stages that are generally artificially separated into nucleation (appearance) of new particles, growth (increase of particle size at constant number per unit volume), and coarsening (diminution of the number of particles at constant volume fraction). Practically, these stages are inter-related and a complete description of precipitation requires also considering other processes such as shrinkage, heterogeneous nucleation and competition between different forming phases that can be stable or metastable [60].

Mesoscale modeling can provide the critical link between the atomic level fundamental calculations and the macroscopic constitutive modeling. They generally take formation energy of precipitates, interfacial energy between precipitates and matrix, and diffusivity of solute in matrix as input, and give size distribution of precipitates as a function of time. In this section, typical mesoscale modeling methods, including classical nucleation and growth theory (CNGT), cluster dynamics (CD) method and phase field (PF) method, will be demonstrated briefly, with a focus on comparing the advantages and disadvantages of these methods.

2.1.1 Classical nucleation and growth method

Classical nucleation theory (CNT) is based on the changes in Gibbs energy $\Delta G$ associated with the formation of a precipitate in a supersaturated solid solution. The evolution of precipitates at different stages are solved with different equations.

In the case of spherical precipitates of radius $R$, recall Eq. ( 1-3 ), $\Delta G(R)$ is given by

$$\Delta G(R) = -\frac{4}{3}\pi R^3 \Delta G_v + 4\pi R^2 \gamma \qquad (2\text{-}1)$$

where $-\Delta G_v$ is the driving force for precipitation per unit volume and $\gamma$ is the specific interfacial energy. The radius at which $d\Delta G/dR=0$ is called critical radius $R^*$, and formation energy of critical radius is the nucleation barrier $\Delta G^*$.

Classical nucleation and growth theory (CNGT) deals with (i) the rate at which stable nuclei ($R > R^*$) appear and (ii) the time evolution of the precipitate size distribution.

With evolution of CNT [61–64], the nucleation rate is calculated by

$$\left.\frac{dN}{dt}\right|_{nucl} = N_0 Z \beta^* \exp\left(-\frac{\Delta G^*}{kT}\right) \exp\left(-\frac{\tau}{t}\right) \qquad (2\text{-}2)$$

where $N_0$ is the number of nucleation sites per unit volume, $Z$ is the Zeldovich factor, $\beta^*$ is the condensation rate of solute atoms in a cluster of critical size $R^*$, and $\tau$ is the incubation time for nucleation. More details about how to calculate each of these can be found from [65].

In binary alloys, the diffusion controlled growth rate of precipitates (molar composition $X^p$, radius $R$) embedded in supersaturated solid solution (mean solute mole fraction in the matrix $X$, equilibrium solute mole fraction $X^e$ at the precipitate/matrix interface) has been provided by Zener [66] under the assumption of small supersaturation ($X^0$-$X^e$<<$\alpha X^p$-$X^e$):

$$\left.\frac{dR}{dt}\right|_{growth} = \frac{D}{R}\frac{X - X^e(R)}{\alpha X^p - X^e(R)} \qquad (2\text{-}3)$$

Small precipitates are less stable than large ones. At a constant volume fraction, small precipitates will then shrink (until complete dissolution) to the benefit of large ones, which will

grow. This is the so-called coarsening mechanism that was investigated simultaneously by Lifchitz and Slyosov [67] and Wagner [68]. They proved that the particle size distribution (PSD) tends to a self-similar form (Lifshitz-Slyozov-Wagner (LSW) distribution) and managed to predict the mean radius evolution of a PSD from the Zener growth equation and a linearized form of the Gibbs-Thomson equation. The coarsening rate is calculated by

$$\left.\frac{d\bar{R}}{dt}\right|_{coars} = \frac{4}{27}\frac{X^e}{\alpha X^p - X^e}\frac{R_0 D}{\bar{R}^2} \quad (2\text{-}4)$$

where $R_0 = 2\gamma V^P/(kT)$, in which $V^P$ is the atomic volume of precipitates.

CNGT shares some advantages and disadvantages with CD when comparing to other mesoscale methods. They both treat nuclei as bulk material with macroscopic properties, which becomes unreasonable when considering a nucleus of only several atoms or molecules; the center of the cluster is far from the thermodynamic limit, and the sharp curvature of the cluster significantly increases the free energy of its surface [69]. However, their low computational cost and the sophisticated physics included in the growth of the precipitates make them very powerful to make long term quantitative predictions. The differences between CNGT and CD will be discussed in Sec. 2.1.2 after we introduce CD.

### 2.1.2 Cluster dynamics

Cluster dynamics (CD) is another mesoscale modeling method that is usually used to study the evolution of precipitates. Unlike in CNGT where different equations will be solved regarding to the different stages of precipitates, e.g. nucleation, growth and coarsening, CD gives the time evolution of the particle size distribution of all stages seamlessly with only one question [70–73]:

$$\frac{\partial f(n,t)}{\partial t} = J_{n-1\to n} - J_{n\to n+1} \quad (2\text{-}5)$$

where $f(n,t)$ is the concentration of clusters containing $n$ atoms at time $t$, $J_{n-1\to n}$ and $J_{n\to n+1}$ describe the transition rates into and out of cluster size $n$ from and to adjoining clusters in cluster size space, respectively. And they are calculated by

$$J_{n\to n+1} = \omega_{n,n+1}^{(+)} f(n,t) - \omega_{n+1,n}^{(-)} f(n+1,t) \quad (2\text{-}6)$$

where $\omega_{n,n+1}^{(+)}$ are the rates at which clusters of size $n$ absorb single atoms to grow to size $n$+1. Similarly, the coefficients $\omega_{n+1,n}^{(-)}$ are the rates at which clusters of size $n$+1 emit single particles to shrink to size $n$. They are related to the diffusion coefficients of solutes in matrix, formation energy of precipitates. More details on how these are obtained will be illustrated in Sec. 2.4.

As mentioned in Sec. 2.1.1, CD shares some advantages and disadvantages with CNGT. However, they also have their own advantages and disadvantages which will make researchers choose one over the other given a specific problem. While CNGT can be used to deal with more situations, both dilute and dense systems, CD is usually only suitable for dilute systems. Unlike CD that calculates the particle size distribution over the whole size space, CNGT assumes a steady state size distribution when the cluster size is smaller than critical radius of precipitates. Another difference is that, as mentioned above, CD treats all three stages of precipitation (nucleation, growth and coarsening) seamlessly with just one equation, and can calculate the number density of each cluster size continuously, while in CNGT, different equations need to be solved for each stage of precipitates, and one needs to be careful when choosing the size of each class of precipitates. In summary, CD is much easier to be implemented for dilute systems while CNGT can deal with more systems that CD might not be suitable.

### 2.1.3 Phase field method

Phase field is a common method in mesoscale modeling of microstructure evolution of precipitation. It's extremely powerful in the visualization of microstructure development. In the

phase-field method, the state of the entire microstructure is represented continuously by a single variable known as the *order parameter* $\varphi$. For example, $\varphi$=1, $\varphi$=0 and $0<\varphi<1$ represent the precipitate, matrix and interface, respectively. The latter is therefore located by the region over which $\varphi$ changes from its precipitate-value to its matrix-value. The range over which it changes is the width of the interface. The set of values of the order parameter over the whole microstructure is the *phase field*.

The evolution of the microstructure with time is assumed to be proportional to the variation of the free energy functional with respect to the order parameter:

$$\frac{\partial \varphi}{\partial t} = M \frac{\partial g}{\partial \varphi} \quad (2\text{-}7)$$

$$\frac{\partial C}{\partial t} = \nabla \left( M \nabla \frac{\delta g}{\delta C} \right) \quad (2\text{-}8)$$

where $\varphi$ is non-conserved order parameter [74,75], $C$ is conserved order parameter [76,77], and $M$ is a mobility. The term $g$ describes how the free energy varies as a function of the order parameter. More details can be found in [74–78].

The simulation grid size is pre-defined that it needs to be small enough to capture the growth of precipitates accurately, but it also needs to be large enough that the simulation process is computationally efficient. For simulation of precipitates, a nucleation rate will be calculated and random grains will be chosen as transforming to precipitates, thus the nucleation process won't be simulated precisely in phase field.

Given the advantage of phase field that it's suitable for the visualization of microstructural development and is a flexible method with phenomena such as morphology changes, particle coalescence or splitting and overlap diffusion fields naturally handled, it can also include a variety of physical effects such as the composition dependence of mobility, strain gradients, soft impingement, hard impingement anisotropy etc. There are some disadvantages. It is more

challenging to do quantitative comparisons between experiments and phase field simulations, and most applications are limited to the study of morphological evolution. Interface width is an adjustable parameter which may be set to physically unrealistic values. Indeed, in most simulations the thickness is set to values beyond those known for the system modelled. This may result in a loss of detail and unphysical interactions between different interfaces. The definition of the free energy density variation in the boundary is somewhat arbitrary and assumes the existence of systematic gradients within the interface. In many cases there is no physical justification for the assumed forms. A variety of adjustable parameters can therefore be used to fit an interface velocity to experimental data or other methods [79].

## 2.2 CALPHAD and thermodynamics calculations

CALPHAD (CALculation of PHAse Diagram) is a powerful tool for thermodynamic calculations of a complicated system based on Gibbs energy description of individual phases. It can predict the phase behavior of higher-order properties from their lower-order binary and ternary systems. The equilibrium state of the system as a function of various conditions, such as temperature, pressure and composition, can be obtained by minimizing its Gibbs energy. The Gibbs energy of a system can usually be written as [80]

$$\mathrm{G} = \sum_i x_i G_i^0 + \mathrm{G}_{mix}^{ideal} + \mathrm{G}_{mix}^{xs} + G^{mag} \quad (2\text{-}9)$$

where $x_i$ is the composition of each component, $G_i^0$ is the Gibbs energy of each pure component, $\mathrm{G}_{mix}^{ideal}$ is the mixing energy for ideal solution, $\mathrm{G}_{mix}^{xs}$ is the contribution due to non-ideal interactions between components, also known as the Gibbs excess energy of mixing, and $G^{mag}$ is the magnetic contribution to Gibbs energy. $\mathrm{G}_{mix}^{ideal}$ and $\mathrm{G}_{mix}^{xs}$ can generally be written in the following forms.

$$\mathrm{G}_{mix}^{ideal} = RT \sum_i x_i \ln x_i \quad (2\text{-}10)$$

$$\mathrm{G}_{mix}^{xs} = \sum_i \sum_{j>i} x_i x_j \sum_v \Omega_{ij}^v \left(x_i - x_j\right)^v + \sum_i \sum_{j>i} \sum_{k>j} x_i x_j x_k L_{ijk} \quad (2\text{-}11)$$

Here, $R$ is the gas constant, $T$ is temperature, $\Omega_{ij}^v$ is the binary interaction parameter dependent on the value of $v$, and $L_{ijk}$ is the ternary interaction parameter. The above equation for $\mathrm{G}_{mix}^{xs}$ becomes

regular when $\upsilon = 0$ and sub-regular when $\upsilon = 1$. In practice, the value for $\upsilon$ does not usually rise above 2, and $L_{ijk}$ is usually zero.

Currently, there are a few commercial software that are based on CALPHAD, such as Thermo-Calc [81], CompuTherm [82], MatCalc [83] et al., which makes the application of CALPHAD more accessible. The major difference between these different software is the different database they focus on. Thus, depending on the specific system one is interested in, one software may be better than the other.

For the MNSPs evolution in RPV steels, the thermodynamic calculations were done with TCAL2 database [84] implemented in Thermo-Calc. Although it is an Al-based database, it contains a comprehensive thermodynamic description of all binaries and ternaries in the Fe-Mn-Ni-Si system over the entire range of relevant compositions and temperatures. Equilibrium phases and mole fractions of MNSPs were predicted, and the equilibrium solute product were calculated for all temperatures studied. When doing the calculation, bcc_B2 and B2_bcc phases were excluded since RPV steel is believed not ordered phase. Detail results will be provided in 0.

2.3 *Ab initio* calculation

*Ab initio* calculations were performed in the general framework of density functional theory (DFT) [85,86] using the Vienna *Ab initio* Simulation Package (VASP) [87–90] to study the solubility of Fe in MNSPs forming in bcc Fe. Within DFT, the total energy is expressed in terms of the total electron density rather than the wavefunction. In this type of calculation, there is an approximate Hamiltonian and an approximate expression for the total electron density. The key advantage of DFT methods is a high computational accuracy but without the additional increase in computing time associated with more rigorous methods.

One of the main disadvantages of DFT methods is the challenge in determining the most appropriate method for a particular application. For the exchange correlation energy, Local Density Approximation (LDA) [91] is the basis of all approximations of it, by which for any small region, the exchange-correlation energy is approximated by that for jellium of the same electron density. The accuracy of the LDA for the exchange energy is typically within 10%, this moderate accuracy is insufficient for most applications. A more sophisticated approximation is Generalized Gradient Approximation (GGA) [92], which estimates the contribution of each volume element to the exchange-correlation based upon the magnitude and gradient of the electron density within that element. Therefore, for all calculations in this thesis GGA will be used for the exchange-correlation energy.

## 2.4 Cluster dynamics and sub models

In this thesis, the evolution of Mn-Ni-Si precipitates (MNSPs) will be studied with cluster dynamics method. The reason that CD was chosen here is because the concentration of Mn, Ni and Si in RPV steels are very low that it can be treated as a dilute system, and we are more interested in the long term evolution of MNSPs on the hardening of RPV steels to decide if the life of current nuclear reactors can be extended to 80 years or more. The code is available online at https://github.com/uw-cmg/MNS_CD, access available upon request prior to public release.

### 2.4.1 Cluster dynamics

As mentioned in Sec. 2.1.2, CD gives the time evolution of particle size distribution by solving a series of master equations. Besides homogeneous nucleation, we also introduced a heterogeneous nucleation term into the model (details regarding heterogeneous nucleation will be presented in Sec. 2.4.2), which made the equation become:

$$\frac{\partial f(n,t)}{\partial t} = R_{het}(n,t) + \omega_{n-1,n}^{(+)} f(n-1,t) - \omega_{n,n-1}^{(-)} f(n,t) + \omega_{n+1,n}^{(-)} f(n+1,t) - \omega_{n,n+1}^{(+)} f(n,t) \quad (2\text{-}12)$$

where $R_{het}$ is the rate of heterogeneous nucleation.

For the nucleation and growth of a phase containing a single component and for clusters up to size $n_{max}$, the PDE in Eq. (2-12) may be solved by discretizing it into $n_{max}$ coupled ODEs, one for each cluster size class. However, when considering the nucleation and growth of a phase containing multiple components, the cluster size distribution becomes a function of the number atoms of each precipitating component. In other words, for a system with $j$ precipitating components, Eq. (2-12) becomes

$$\frac{\partial f(n_1,n_2n_3,\ldots,n_j,t)}{\partial t} = R_{het}(n,t) + \sum_{i=1}^{j} \begin{Bmatrix} \left[\omega_{n_i-1;n_i}^{(+)} f(n_i-1,t) - \omega_{n_i;n_i+1}^{(-)} f(n_i,t)\right] - \\ \left[\omega_{n_i;n_i+1}^{(+)} f(n_i,t) - \omega_{n_i-1;n_i}^{(-)} f(n_i+1,t)\right] \end{Bmatrix} \quad (2\text{-}13)$$

Solving Eq. (2-13) by discretization into coupled ODEs requires a set approximately $\sum_{n=1}^{n_{max}} \frac{(n+j-1)!}{n!(j-1)!}$ equations. Thus, for even a small number of components, the solution of Eq. (2-13) by this approach quickly becomes computationally intractable. In particular, for 3 components this becomes

$$\sum_{i=1}^{n_{max}} \frac{(i+2)!}{i!\cdot 2!} = \frac{1}{2}\sum_{i=1}^{n_{max}} (i+1)(i+2) = n_{max} + \frac{n_{max}(n_{max}+1)(n_{max}+2)}{6} \sim O(n_{max}^3)$$

equations.

The formalism presented by Slezov and Schmelzer in refs [70–73] provides an alternative solution method whereby the cluster size distribution may be evaluated as a function of only the total number of atoms in the cluster $n$ for a system of an arbitrary number of precipitating components. This approach is based upon the assumption that clusters travel along a trajectory of minimum free energy through composition space as they grow or shrink. The coefficients $\omega_{n,n+1}^{(+)}$ in Eq. (2-12)

then become effective absorption rates as clusters travel along this trajectory. For a system containing *j* precipitating components, these rates are given by

$$\omega_{n,n+1}^{(+)} = \left[\sum_{i=1}^{j}\left(\frac{\nu_{i\alpha}^2}{\omega_{n_i;n_i+1}^{(+)}}\right)\right]^{-1} \quad (2\text{-}14)$$

where $\omega_{n_i;n_i+1}^{(+)}$ is the rate at which clusters of size *n* gain one atom of species *i*. The parameter $\nu_{i\alpha}$ accounts for the change in the composition of component *i* as the cluster grows from size *n* to *n*+1. $\nu_{i\alpha}$ is defined by the following expression:

$$\nu_{i\alpha} = x_{i\alpha} + n\frac{d\nu_{i\alpha}}{dn} \quad (2\text{-}15)$$

where $x_{i\alpha}$ is the atomic fraction of component *i* in clusters of size *n*. Here we assume that $x_{i\alpha}$ doesn't change with *n*, thus $\nu_{i\alpha}$ equals to $x_{i\alpha}$.

For diffusion-limited growth of the clusters, the absorption rate becomes

$$\omega_{n,n+1}^{(+)} = 4\pi c_\beta a_\alpha D_{eff}^d n^{1/3} \quad (2\text{-}16)$$

$$\frac{1}{D_{eff}^d} = \sum_{i=1}^{j}\frac{\nu_{i\alpha}^2}{x_{i\beta}D_i} \quad (2\text{-}17)$$

where $c_\beta$ is the total volume concentration of the particles of the different components in the ambient phase, $x_{i\beta}$ is the molar fraction of the different components in the ambient phase. $c_\beta$ is equal to $1/\Omega_a$, where $\Omega_a$ is the atomic volume of matrix.

The emission rate is given by

$$\omega_{n+1,n}^{(-)} = \omega_{n,n+1}^{(+)} exp\left(\frac{\Delta G(n+1)-\Delta G(n)}{k_B T}\right) \quad (2\text{-}18)$$

where $\Delta G(n)$ is the formation energy of clusters with *n* atoms from the matrix, which can be written as

$$\Delta G(n) = n\left(g_p - \sum_i x_{i\alpha}\mu_i\right) + \sigma(n) \quad (2\text{-}19)$$

where $g_p$ is the free energy per atom of the precipitate phase, $\mu_i$ is the chemical potential of component *i* in the matrix, and $\sigma(n)$ is the interfacial energy of a cluster of size *n*. With this form, the difference $\Delta G(n+1)$-$\Delta G(n)$ reduces to

$$\Delta \mathrm{G}(n+1) - \Delta \mathrm{G}(n) = \mathrm{g}_p - \sum_i x_{i\alpha}\mu_i + [\sigma(n+1) - \sigma(n)] \quad (2\text{-}20)$$

The chemical potentials in the matrix can be written as:

$$\mu_i = \mu_i^0 + kT[ln\delta_i + lnc_i] \quad (2\text{-}21)$$

Here the matrix is assumed to behave as a dilute alloy and the solute activity follows Henry's law such that $\delta_i$ is constant. When the matrix phase is in equilibrium with the precipitate phase, we may write

$$\mathrm{g}_p - \sum_i x_{i\alpha}\mu_i = 0$$

$$\mathrm{g}_p - \sum_i x_{i\alpha}[\mu_i^0 + kTln\delta_i] = kT\sum_i x_{i\alpha} lnc_i \quad (2\text{-}22)$$

In dilute alloys, the emission rate can be written as

$$\omega_{n+1,n}^{(-)} = \omega_{n,n+1}^{(+)} \frac{\overline{\prod_i c_i^{x_{i\alpha}}}}{\prod_i c_i^{x_{i\alpha}}} \exp\left(\frac{\sigma(n+1)-\sigma(n)}{k_B T}\right) = \omega_{n,n+1}^{(+)} \frac{\overline{K_{sp}}}{K_{sp}} \exp\left(\frac{\sigma(n+1)-\sigma(n)}{k_B T}\right) \quad (2\text{-}23)$$

where

$$K_{sp} = \prod_i c_i^{x_{i\alpha}} \quad (2\text{-}24)$$

is defined as the solute product of a certain phase. $\overline{K_{sp}}$ is the value of the solute product in equilibrium.

The distribution function $f(n=1, t)$ at $n$=1 is described as

$$f(n=1,t) = c_\beta \prod_{i=1}^{j} x_{i\beta}^{x_{i\alpha}} \quad (2\text{-}25)$$

The physical parameters that must be determined to apply to above model are diffusion coefficients, interfacial energies, and equilibrium solute products of all precipitate phases.

2.4.2 Heterogeneous nucleation

Dislocations and grain boundaries are usually considered as common heterogeneous nucleation sites. There are also some experimental data showing the nucleation of MNSPs on these sinks [32,34]. However, as will be shown in Table 2-1, the upper limit of available nucleation sites by these mechanisms are inadequate to match the high concentrations seen in experimental data ($\sim 10^{24} m^{-3}$) [24]. Therefore, these sources of heterogeneous nucleation, while they may be present, cannot be playing a significant role in the typically observed precipitate density (although they may play a major role for very low solute alloys or under some conditions where only low number of density of precipitates is observed). Heterogeneous nucleation of MNSPs on Cu precipitates has also been observed [24], but since the alloys studied here have such low Cu content that no Cu precipitation occurs [24,33] or the number density of Cu clusters observed is much smaller than that of MNSPs [34], the effect of Cu on nucleation of MNSPs will be effectively incorporated into the heterogeneous nucleation model we developed here.

Table 2-1 Estimation of the upper limit of number density of nucleation sites on dislocations and grain boundaries. All values are approximate.

| Nucleation types | Typical parameters | | | Nucleation sites ($m^{-3}$) |
|---|---|---|---|---|
| Dislocation | Density $\rho$ ($m^2$) | Typical precipitate diameter d (nm) | | $\rho/d \approx 10^{22}$-$10^{23}$ |
| | $(1\text{-}10)\times 10^{14}$ | 1-5 | | |
| Grain Boundary | Grain size D (m) | Grain boundary thickness $\delta$ (m) | lattice sites $C_0$ ($m^{-3}$) | $C_0\delta/D \approx 10^{23}$ |
| | $10^{-5}$ | $10^{-10}$ | $10^{28}$ | |

Although heterogeneous nucleation on grain boundaries and dislocations is not likely to play a significant role in the precipitates studied here, heterogeneous nucleation on cascade damage is a possible mechanism and thus we have developed an approach to include it in our model. The high concentrations of point defects generated in the cascades, during both formation and much longer time aging periods, lead to defect-solute cluster complex formation due to corresponding

defect-solute binding energies and local RIS. The first model for solute-defect complex formation (Cu-coated nanovoids) was first proposed by Odette [17] and later confirmed by a number of Kinetic Lattice Monte Carlo models of cascade aging [19,93]. These defect-solute cluster complex are called unstable matrix defects (UMDs). According to Monte Carlo simulations [35,36,49,94] as well as indirect experimental measurements [95–99], there will be a high density of UMDs that form in cascades (the impact of these UMDs on RED will be discussed in Sec. 2.4.3). These UMDs can serve as nucleation sites for larger stable matrix features (SMF) such as loose aggregates of solutes [10]. Also nanometric dislocation loops have been observed by TEM in VVER steels [95–97] and PWR steels under high dose with ions or electrons [98,99]. Recent Monte Carlo study showed that these small dislocation loops may act as points for heterogeneous nucleation of solute precipitates [36,49,94].

To implement the heterogeneous nucleation on damage into CD model, we assume that clusters of size $n$ are generated in displacement cascades at a rate $R_{het}(n,t)$, which has units of number of clusters generated per unit volume and per unit time. $R_{het}$ is proportional to the cascade production rate per atom, $\sigma_{cas}\phi/\Omega$, where $\sigma_{cas}$ is the cascade production cross section, $\phi$ is the neutron flux, and $\Omega$ is the atomic volume. $R_{het}$ also depends on the amount of the remaining dissolved solute, which we represent by the ratio of the instantaneous triple product $K_{sp}$ to a reference $K_{sp}^0$. Finally, the fact that at a given $K_{sp}$ only a fraction of cascades produce a large cluster of defined size $n$, is represented by a cascade cluster production efficiency factor, $\alpha$, at $K_{sp}$. While there is a distribution of $n$ that can contribute to heterogeneous nucleation, for simplicity assume that only clusters of size $n_{het}$ are generated. Thus $R_{het}$ is given by

$$R_{het}(n_{het},t) = \alpha \cdot \frac{\sigma_{cas}\phi}{\Omega} \cdot \frac{K_{sp}(t)}{K_{sp}^0}, \qquad (2\text{-}26)$$

$$\text{and } R_{het}(n \neq n_{het},t) = 0$$

The efficiency factor, $\alpha$, is a fitting parameter representing the fraction of cascades that produce a cluster of size $n_{het}$ when the solute product is at equilibrium ($K_{sp}(t) = K_{sp}^0$). The physical basis for $\alpha$ is partly stochastic, and partly associated with the energy of the primary knock-on atom (PKA) that creates the cascade (note, PKAs are generated by fast neutrons over a wide range of recoil energies). However, given the complexity of forming solute-defect complexes in displacement cascades, $\alpha$ is treated as the second heterogeneous fitting parameter.

While rooted in plausable physics, this nucleation model is a surrogate for more complex mechanisms of heterogeneous nucleation that may include solute segregation to ex-cascade small loops and nanovoids. Note, this treatment does not include the role of dislocations and grain boundaries in heterogenoeus nucleation, although both are observed experimentally, especially for conditions of low solute supersaturations. Further, the present model does not treat the potential role of Cu. While the alloys studied here have low Cu contents, it has long been observed and predicted that small amounts of this element, even below the concentration for well-formed precipitates, can enhance MNSP nucleation [16]. Such effects, to the extent they are significant, are effectively renormalized into the fitting parameters in the model.

### 2.4.3 Radiation enhanced diffusion (RED)

The cluster dynamics model used in this work requires Mn, Ni, and Si diffusion coefficients under irradiation. The diffusion of these species is accelerated by excess vacancies produced under irradiation, a phenomenon generally referred to as radiation enhanced diffusion (RED). A model for RED is used in this work that accounts for flux effects with a simple power law-scaling model. We use a simplified version of a RED model developed by Odette et al. that accounts for solute vacancy trap enhanced recombination and extra annihilation of vacancies and self-interstitial atoms at transient sinks formed in cascades [100–102].

The RED coefficient, $D^*$, can most simply be expressed as [102]

$$D^* \approx D_v X_v \frac{D^{th}}{D^{sd}} + D^{th} \quad (2\text{-}27)$$

where $D^*$ is the diffusion coefficient under irradiation, $D_v$ is the diffusion coefficient of vacancies, $X_v$ is the vacancy concentration under irradiation, $D^{th}$ is the solute thermal diffusion coefficient of solute under thermal aging condition, and $D^{sd}$ is the self-diffusion coefficient of Fe in the matrix.

Defect conservation balances, treating vacancy and SIA production, transport and fate, were used to establish the steady-state vacancy concentration ($X_v$) under irradiation, which can be expressed from rate theory models as a function of the fraction of vacancies and self-interstitials (SIA) that escape recombination and reach fixed dislocation sinks ($g_s$), which is given as:

$$X_v = \frac{g_s \xi \sigma_{dpa} \phi}{D_v Z_t} \quad (2\text{-}28)$$

Here, $\phi$ is irradiation flux, $\sigma_{dpa}$ is the displacement-per-atom (dpa) cross-section[2], $\xi$ is the cascade surviving defect production to dpa efficiency factor, .

We will assume that the precipitate growth is dominated by vacancy mediated diffusion of solutes to the precipitates, so correct modeling of the vacancy concentrations and associated RED is critical. Vacancy fates include clustering, annihilation at sinks and recombination with SIA. The dominant fixed sinks for vacancies are typically dislocations in RPVs. When the irradiation flux is low, fixed sinks are dominant, it can be shown that

$$g_s = \frac{2}{\eta}\left[(1+\eta)^{1/2} - 1\right] \quad (2\text{-}29)$$

$$\eta = \frac{16\pi r_v \xi \sigma_{dpa} \phi}{\Omega_a D_v Z_t^2} \quad (2\text{-}30)$$

Here, $r_v$ is the SIA-vacancy recombination radius, $\Omega_a$ is the atomic volume, and $Z_t$ is sink strength.

[2] The dpa rate is the neutron flux $\phi$ (with units of neutrons/area-time) times $\sigma_{dpa}$ (with units of area/neutron-atom) times $\xi$. $X_v D_v Z_t$ is the annihilation rate of defects at sinks in the absence of recombination. The $g_s$ term accounts for defects lost to recombination.

However, unstable matrix defects (UMD) also act as vacancy sinks and can be dominant at very high flux [102]. Furthermore, recombination will be greatly enhanced if vacancies are strongly bound to these UMDs. Odette et al. [102] have built a model to include the effect of UMD in the recombination-dominated regime under very high irradiation flux, which gives a more detailed model for $g_s$ that accounts for flux dependent solute-trap enhanced recombination between vacancies and interstitials, with $g_s < 1$. The expression for $g_s(\phi,T, Z_t,\ldots.)$ is complex and contains a number of parameters, like vacancy trapping energy, solute trap concentrations, and the sink strength, where the latter may evolve with irradiation. Thus we have chosen a much simpler expedient to calculate $g_s$ as a function of flux that has been empirically highly successful [101–103]. The simple model approximates $g_s$ by a scaling law as

$$\mathrm{g}_s(\phi) \approx \mathrm{g}_s(\phi_r)(\frac{\phi_r}{\phi})^p \qquad (2\text{-}31)$$

Here, $\phi_r$ is an arbitrarily selected low reference flux, taken as $3\times10^{15}\mathrm{m}^{-2}\mathrm{s}^{-1}$, and $p$ is a scaling exponential factor. $g_s(\phi_r)$ can be calculated by Eq. (2-29) and $g_s(\phi_r) \approx 1$. The effective $p$ starts at 1 in the thermal diffusion dominated regime at very low flux; $p$ is 0 in the sink-dominated regime and $p$=0.5 in the recombination-dominated regime. The $p$ again approaches 1 at high flux in the UMD sink-dominated regime. We will use this scaling law expression in our model to effectively include the effects of UMDs on the vacancy concentrations. Thus $D^*$ can be expressed as a function of flux as [102]

$$D^* = D^{th}\frac{\xi\sigma_{dpa}[g_s(\phi_r)(\phi_r/\phi)^p]}{Z_t D^{sd}}\phi = k(\phi,\ldots)\phi \qquad (2\text{-}32)$$

Given the approximate estimates of $D^{th}$ and the additional complexity of RED treated by a simple model, there is no reason to expect that the $D^*$ would be accurate within the very precise constraints that would be needed for perfect agreement of the CD model with the data. However, if we allow $D^*$ to vary so as to fit the experimental mole fraction data points exactly, the resulting

values fall within a factor of two of the standard fixed CD values for all alloys except Ginna (where the difference is only a factor of three), as can be seen from Figure 6-5 shown in Sec.6.5. Finally, we note that there may be some evolution of the sink density at high fluence. However, there is insufficient information to treat this in the model. The most extreme estimates of the dislocation loop density at high fluence might double the initial network value. However, the effects of increases in the sink density at high flux are reduced by corresponding decreases in recombination rates.

The effective time evolution of the model is set by both the diffusion rates and the homogeneous and heterogeneous nucleation rates. Ignoring the nucleation rate effects for the moment, the scaling in Eq. (2-31) means that the time evolution of the system is controlled by an effective time $t_e = t(\phi_r/\phi)^p$. This time scaling allows us to define an effective fluence,

$$\phi t_e = \phi t(\phi_r/\phi)^p \qquad (2\text{-}33)$$

Here $\phi t$ is the actual fluence. The effective fluence accounts for how flux affects the excess irradiation induced vacancies that accelerate diffusion. In the $g_s = 1$ sink-dominated limit there is no flux effect on $D^*t$, while in the recombination dominated limit $g_s$ is proportional to $(\phi_r/\phi)^{0.5}$. Thus higher flux delays MNSP (and CRP) evolution. Independent analysis has shown $p$ typically varies between ≈ 0.15 and 0.35 over a wide range of higher flux (or equivalent dpa rates for charged particle irradiations) [31]. Thus a nominal value of $p = 0.2$ was used in this work. We also selected a reference flux $\phi_r = 3\text{x}10^{15}$ n·m$^{-2}$s$^{-1}$ [102]. Note, the low flux is consistent with being in a nearly sink dominated regime with $g_s \approx 1$ [102].

This very simple model for the effect of flux on RED, however, does not account for flux effects on heterogeneous nucleation rates. In particular, we note that in our model the heterogeneous nucleation term, $R_{het}$, depends directly on flux (as described in Sec. 2.4.2), therefore

reflects the flux independent number of cascades at a given fluence, that scales with $\phi t$ rather than with $\phi t_e$. The CD model directly accounts for both homogeneous and heterogeneous effects on nucleation, and the *p*-flux scaling approach is only used to account for radiation enhanced diffusion. We also note that the $k(\phi)$ in Eq. (2-32) is almost certain to vary somewhat from alloy to alloy, and for different irradiation conditions, in a way that is not fully modeled by the multi element $D^{th}$ and *p*-flux scaling approach. Thus the predictions of the precipitate size distribution, *r*, *N* and *f* would be expected to move to higher or lower positions on the fluence scale depending on the individual case. While it could be argued that each particular set of alloy-irradiation conditions (say CM6 and ATR-1 – see 0) should be individually fit for $D^*$, we chose to use only one calculated $D^*(\phi_r)$ along with the *p*-scaling flux adjustment, so that the model can be applied across many alloys and used to model new situations where fitting $D^*$ is not possible. In spite of its approximate nature and simplicity, as shown below, the unfitted treatment of $D^*$ works remarkably well within the context of the current objectives of the model.

# Chapter 3 Experimental database

## 3.1 Chapter Abstract

In this chapter, the experimental database will be summarized. To separate the effect of Cu on the evolution of MNSPs, all the experimental data used in this thesis are from low-Cu (<0.07at.%) RPV steels. Experimental data from two techniques have been used for the model building and validation. One is the microstructural experimental data from atom probe tomography (APT), the other is yield stress data from micro-hardness measurements. Microstructural experimental data includes the number density, mean radius, mole fraction as well as the particle size distribution (PSD) of precipitates under different conditions. Number density, mean radius and mole fraction of precipitates under irradiation were used to fit CD model parameters that are not available in literature. All other information, including PSD under irradiation, microstructural information and yield stress at post-irradiation annealing condition were used to further validate the model.

## 3.2 Microstructure experimental data

In this section, the microstructural experimental data from APT will be summarized. Since there is still no standard on APT data analysis, people from different research groups will give different results even given the same data set, we will first introduce the analysis method and parameters used for the experimental data provided by our collaborators from Professor Odette's group in University of California - Santa Barbara and Dr. Philip Edmondson in Oak Ridge National Laboratory.

### 3.2.1 Techniques and analysis method

Details of the APT analysis can be found from [24,34], we will just briefly summarize some key information here for the readers' convenience. The cluster analysis was performed using a

modified version of the maximum separation method, also referred to as the density-based clustering algorithm; here, instead of finding the distance ($d$) between a solute, defined as Cu, Ni, Mn and Si, and its nearest solute neighbor, the corresponding distance between a solute and its fifth nearest solute neighbor is found [104]. If $d$ is less than a defined distance ($d_{max}$), the solute is considered to be a core atom. After all core atoms have been found, any solute atom within $d_{max}$ of a core atom is considered to be in the same cluster. Any cluster with less than $N_{min}$ atoms is excluded from the analysis. Here, $d_{max}$ = 0.50–0.60 nm and $N_{min}$= 15–30. Morover, the excess Fe in precipitates was treated as an artifact. Thus the analysis assumes the precipitates found in this study do not contain a significant amount of Fe.

The precipitate sizes were calculated by determining the spherical radius, $r_p$, of the volume of the total number of solute atoms in a cluster, corrected for the detection efficiency, assuming the solute atomic volume is the same as for Fe, as

$$r_p = \sqrt[3]{\frac{3N_{sol}\Omega}{4\pi\eta}} \qquad (3\text{-}1)$$

Here $N_{sol}$ is the number of Cu, Ni, Mn and Si atoms in a given cluster, Ω is the atomic volume of Fe, and $\eta$ is the efficiency of the LEAP (0.37 in the case of a reflectron-equipped instrument). The possible intermetallic phases that exist in these steels have atom densities that vary from those of Fe within ±10%, so the corresponding effect on $r_p$ is less than ~±3%. The corresponding cluster mole fraction, $f$, is estimated by dividing the total number of solutes in the precipitates by the total number of atoms in the sample.

In the case that multiple APT measurements were carried out on one alloy, the mean bulk, matrix and precipitate compositions, as well as precipitate <r>, N and f were determined for each tip for a given alloy nominal condition. The ion-weighted mean and standard deviation of the

measurements were calculated for a given alloy from the means of all runs. The expression for the weighted mean and weighted standard deviation are given by:

$$\bar{x} = \frac{\sum_{i=1}^{n} \omega_i x_i}{\sum_{i=1}^{n} \omega_i} \quad (3\text{-}2)$$

$$S = \sqrt{\frac{n}{n-1} \frac{\sum_{i=1}^{n} \omega_i (x_i - \bar{x})^2}{\sum_{i=1}^{n} \omega_i}} \quad (3\text{-}3)$$

Here $\bar{x}$ is the mean value for a set of given alloy condition runs, $x_i$ is the calculated value for the *i*th run for a single alloy condition, *S* is the standard deviation of the mean for the alloy, $\omega_i$ is the total number of atoms for the *i*th measurement, and *n* is the total number of measurements on a single alloy condition.

3.2.2 APT data under irradiation

Five RPV steels irradiated in four reactors were studied. The irradiations included the high flux test reactors, Advanced Test Reactor (ATR) and Belgian Reactor 2 (BR2), and low flux reactor surveillance capsules from the Ringhals and Ginna power plants. Flux and fluence varied from $5.9\times10^{14}$n·m$^{-2}$s$^{-1}$ to $2.3\times10^{18}$n·m$^{-2}$s$^{-1}$ and $3.3\times10^{23}$n·m$^{-2}$ to $1.1\times10^{25}$n·m$^{-2}$ (or dose from 0.0495 to 1.65dpa [30]), respectively. The nominal temperature ranged from 284°C to 300°C. However, a recent as-run reevaluation placed the ATR-1 temperature at ≈320°C, so this adjusted value was used in this work. The test reactor irradiations included Cu free plate (LG) and forging (CM6) that contain ≈ 0.75 to 0.85 wt% Ni and 1.35 to 1.65 wt.% Ni, respectively. These steels have bainitic microstructures and properties characteristic of in-service steels. The steels in the surveillance irradiations were all low Cu (< 0.07 wt.%) steels with intermediate (Ginna) and high (Ringhals) Ni contents, respectively. The data sets are identified by the irradiation condition and alloy designation. However, since the main variables are the Ni content, flux and fluence, in addition to the identification cited above, a parenthetical notation is added to designate a low (L), medium (M) or high (H) category, for these compositional and irradiation variables, respectively.

The parenthesis gives a 3-tuple whose order corresponds to Ni content, flux, and fluence. For example, Ringhals N is categorized as (HLM), meaning high Ni, low flux and medium fluence, while ATR-1 LG as (MHH), meaning medium Ni, high flux and high fluence. Note that these designations do not account for variations in alloy Mn and Si contents.

It was previously shown that nano-scale MNSPs respond to local alloy compositions of individual APT tips [24]. The database used in this study included up to nine APT tips per alloy, yielding a total of 36 different compositions. The average APT measured compositions and irradiation conditions are shown in Table 3-1. The local compositions, when more than one tip was measured, as well as the corresponding number density, mean radius and mole fraction measured in each tip are shown in Table 3-2. The precipitate composition as measured by APT is provided in Table 3-3. Previously published APT on Ringhals welds [33] and Ginna forging [34] were reanalyzed by Edmondson in a way that is consistent with [24] to provide a maximal consistent data set.

Table 3-1 The average alloy compositions and irradiation conditions of low-Cu RPV steels under irradiation.

| Name (Ni, flux, fluence) | Composition (at.%) | | | Irradiation Condition | | | Reference |
|---|---|---|---|---|---|---|---|
| | Mn | Ni | Si | Temperature (°C) | Flux ($\times 10^{16}$ $n \cdot m^{-2} s^{-1}$) | Fluence ($\times 10^{23}$ $n \cdot m^{-2}$) | |
| Ringhals E (HLM) | 1.25 | 1.50 | 0.41 | 284 | 0.147 to 0.166 | 6.39 | [33], |
| Ringhals N (HLM) | 1.14 | 1.68 | 0.28 | | | 3.3, 6.03 | |
| Ginna Forging (MLM) | 0.57 | 0.92 | 0.67 | 290 | 0.0592 | 5.80 | [34], this work |
| BR2-TU LG (MMH) | 1.18 | 0.73 | 0.44 | 300 | 30 | 25 | This work |
| BR2-TU CM6 (HMH) | 1.16 | 1.63 | 0.35 | | | | |
| BR2-G2 CM6 (HHM) | 1.07 | 1.46 | 0.34 | 300 | 100 | 6.67 | This work |
| BR2-G1 LG (MHH) | 1.09 | 0.86 | 0.49 | | | 13.3 | [24] |
| BR2-G1 CM6 (HHH) | 1.09 | 1.34 | 0.33 | | | | |
| ATR-1 LG (MHH) | 0.87 | 0.71 | 0.43 | 320 | 230 | 110 | |
| ATR-1 CM6 (HHH) | 1.42 | 1.69 | 0.39 | | | | |

Table 3-2 Composition and experimental data of different tips measured by APT. The alloy names follow the structure of "irradiation reactor (-irradiation condition name) original alloy name" and the alloy numbers are the original tip numbers used to differentiate different tips for each alloy.

| Alloy Name | Alloy No. | Compositions (at.%) | | | | | | | | Results | | |
|---|---|---|---|---|---|---|---|---|---|---|---|---|
| | | Ni | Mn | Si | (Cu) | Cr | Mo | P | C | Number density ($\times 10^{23}$ $m^{-3}$) | Mean radius (nm) | Mole fraction (%) |
| BR2-TU LG | 5500 | 0.76 | 1.23 | 0.45 | 0.01 | 0.05 | 0.24 | 0.002 | 0.02 | 2.83 | 1.11 | 0.21 |
| | 5805 | 0.72 | 1.15 | 0.44 | 0.01 | 0.05 | 0.16 | 0.004 | 0.03 | 2.38 | 1.08 | 0.16 |
| | 5593 | 0.73 | 1.29 | 0.44 | 0.01 | 0.06 | 0.26 | 0.004 | 0.01 | 2.20 | 1.27 | 0.18 |
| BR2-TU CM6 | 5501 | 1.74 | 1.22 | 0.38 | 0.00 | 0.01 | 0.22 | 0.004 | 0.07 | 15.6 | 1.13 | 1.03 |
| | 5591 | 1.50 | 1.20 | 0.32 | 0.00 | 0.01 | 0.21 | 0.001 | 0.02 | 6.34 | 1.25 | 0.51 |
| | 5592 | 1.62 | 1.27 | 0.35 | 0.00 | 0.01 | 0.24 | 0.003 | 0.03 | 8.65 | 1.24 | 0.71 |
| | 5623 | 1.75 | 0.98 | 0.37 | 0.00 | 0.01 | 0.11 | 0.002 | 0.03 | 11.6 | 1.20 | 0.84 |
| | 5804 | 1.67 | 1.02 | 0.35 | 0.00 | 0.01 | 0.14 | 0.003 | 0.02 | 10.3 | 1.20 | 0.81 |
| BR2-G2 CM6 | 4958 | 1.40 | 1.15 | 0.35 | 0.00 | 0.01 | 0.19 | 0.002 | 0.06 | 4.14 | 0.73 | 0.07 |
| | 5004 | 1.38 | 1.17 | 0.32 | 0.00 | 0.01 | 0.23 | 0.002 | 0.01 | 3.38 | 0.73 | 0.05 |
| | 5005 | 1.53 | 0.93 | 0.34 | 0.00 | 0.01 | 0.12 | 0.000 | 0.04 | 5.23 | 0.71 | 0.08 |
| | 5006 | 1.55 | 1.13 | 0.35 | 0.00 | 0.01 | 0.19 | 0.002 | 0.01 | 3.01 | 0.85 | 0.08 |
| BR2-G1 LG | 4036 | 0.71 | 1.15 | 0.41 | 0.00 | 0.05 | 0.21 | 0.002 | 0.03 | 4.25 | 0.63 | 0.04 |
| | 5201 | 0.83 | 1.15 | 0.47 | 0.01 | 0.05 | 0.18 | 0.000 | 0.02 | 2.72 | 0.77 | 0.05 |
| | 5225 | 0.87 | 1.24 | 0.52 | 0.01 | 0.06 | 0.18 | 0.002 | 0.05 | 9.59 | 0.63 | 0.10 |
| | 5226 | 0.97 | 0.83 | 0.52 | 0.01 | 0.02 | 0.10 | 0.005 | 0.04 | 6.95 | 0.74 | 0.12 |
| BR2-G1 CM6 | 4054 | 1.34 | 1.09 | 0.33 | 0.00 | 0.01 | 0.17 | 0.000 | 0.013 | 4.58 | 0.70 | 0.07 |
| ATR-1 LG | 1789 | 0.72 | 1.00 | 0.38 | 0.00 | 0.04 | 0.21 | 0.00 | 0.09 | 18.4 | 1.21 | 1.28 |
| | 1790 | 0.71 | 0.93 | 0.47 | 0.00 | 0.04 | 0.19 | 0.00 | 0.06 | 18.8 | 1.19 | 1.32 |
| | 1795 | 0.71 | 0.77 | 0.42 | 0.00 | 0.02 | 0.17 | 0.00 | 0.06 | 16.2 | 1.26 | 1.35 |
| | 1796 | 0.67 | 1.15 | 0.44 | 0.01 | 0.05 | 0.24 | 0.00 | 0.06 | 14.0 | 1.30 | 1.32 |
| | 1800 | 0.71 | 0.74 | 0.43 | 0.00 | 0.02 | 0.17 | 0.00 | 0.07 | 16.4 | 1.23 | 1.30 |
| ATR-1 CM6 | 2179 | 1.62 | 1.34 | 0.38 | 0.00 | 0.01 | 0.25 | 0.003 | 0.23 | 19.0 | 1.53 | 2.77 |
| | 2180 | 1.76 | 1.42 | 0.44 | 0.00 | 0.01 | 0.22 | 0.006 | 0.31 | 23.0 | 1.44 | 2.92 |
| | 2185 | 1.90 | 1.37 | 0.43 | 0.00 | 0.01 | 0.31 | 0.009 | 0.22 | 21.2 | 1.43 | 2.82 |
| | 2186 | 1.42 | 1.19 | 0.32 | 0.00 | 0.01 | 0.22 | 0.005 | 0.26 | 16.6 | 1.51 | 2.31 |
| | 2493 | 1.74 | 1.43 | 0.39 | 0.00 | 0.02 | 0.24 | 0.004 | 0.32 | 20.1 | 1.55 | 2.86 |
| | 2495 | 1.71 | 1.37 | 0.40 | 0.00 | 0.01 | 0.26 | 0.006 | 0.20 | 20.3 | 1.51 | 2.81 |
| | 2496 | 1.73 | 1.52 | 0.38 | 0.00 | 0.01 | 0.24 | 0.002 | 0.17 | 17.4 | 1.61 | 2.97 |
| | 2497 | 1.57 | 1.40 | 0.38 | 0.00 | 0.01 | 0.25 | 0.002 | 0.16 | 19.5 | 1.51 | 2.68 |
| | 2498 | 1.69 | 1.50 | 0.40 | 0.00 | 0.01 | 0.27 | 0.003 | 0.08 | 19.5 | 1.54 | 2.89 |
| Ringhals E | E6 | 1.50 | 1.25 | 0.41 | 0.05 | 0.26 | 0.11 | 0.01 | 0.02 | 4.34 | 1.30 | 0.4 |

| | | | | | | | | | | | | |
|---|---|---|---|---|---|---|---|---|---|---|---|---|
| Ringhals N | N110 | 1.97 | 1.09 | 0.28 | 0.06 | 0.13 | 0.14 | 0.02 | 0.01 | 5.79 | 1.55 | 0.9 |
| | N270 | 1.63 | 1.21 | 0.29 | 0.04 | 0.18 | 0.23 | 0.020 | 0.02 | 4.80 | 1.37 | 0.52 |
| | N180 | 1.43 | 1.12 | 0.26 | 0.03 | 0.04 | 0.25 | 0.037 | 0.01 | 3.81 | 1.50 | 0.54 |
| Ginna Forging | - | 0.92 | 0.57 | 0.67 | 0.07 | 0.64 | 0.19 | 0.025 | 0.11 | 4.86 | 1.05 | 0.24 |

Table 3-3 Precipitate composition in each tip measured by APT. The alloy names follow the structure of "irradiation reactor (-irradiation condition name) original alloy name" and the alloy numbers are the original tip numbers used to differentiate different tips for each alloy by the UCSB researchers.

| Alloy Name | Alloy No. | Compositions (at.%) | | | | | | | | |
|---|---|---|---|---|---|---|---|---|---|---|
| | | Ni | Mn | Si | Cu | Cr | Mo | P | C | Fe |
| BR2-TU LG | 5500 | 15.70 | 9.10 | 10.70 | 0.37 | 0.21 | 0.36 | 0.257 | 0.222 | 63.07 |
| | 5805 | 15.93 | 9.64 | 10.68 | 0.09 | 0.07 | 0.19 | 0.543 | 0.057 | 62.79 |
| | 5593 | 13.20 | 8.56 | 8.98 | 0.23 | 0.11 | 0.21 | 0.323 | 0.203 | 68.17 |
| BR2-TU CM6 | 5501 | 19.16 | 9.21 | 5.75 | 0.04 | 0.02 | 0.58 | 0.048 | 0.183 | 64.99 |
| | 5591 | 19.53 | 9.85 | 6.30 | 0.04 | 0.01 | 0.12 | 0.012 | 0.015 | 64.12 |
| | 5592 | 19.55 | 9.70 | 6.10 | 0.07 | 0.02 | 0.21 | 0.106 | 0.050 | 64.18 |
| | 5623 | 21.56 | 8.18 | 6.84 | 0.05 | 0.01 | 0.10 | 0.022 | 0.025 | 63.21 |
| | 5804 | 21.78 | 8.59 | 7.07 | 0.04 | 0.01 | 0.12 | 0.094 | 0.020 | 62.25 |
| BR2-G2 CM6 | 4968 | 24.70 | 15.03 | 7.73 | 0.00 | 0.05 | 0.05 | 0.097 | 0.000 | 52.34 |
| | 5004 | 23.82 | 15.50 | 8.29 | 0.03 | 0.00 | 0.19 | 0.237 | 0.016 | 51.91 |
| | 5005 | 25.85 | 11.90 | 9.19 | 0.02 | 0.00 | 0.05 | 0.011 | 0.043 | 52.92 |
| | 5006 | 23.48 | 14.23 | 8.13 | 0.00 | 0.00 | 0.24 | 0.151 | 0.030 | 53.73 |
| BR2-G1 LG | 4036 | 17.65 | 14.87 | 11.65 | 0.11 | 0.00 | 0.00 | 0.777 | 0.000 | 54.94 |
| | 5201 | 21.84 | 11.89 | 13.62 | 0.22 | 0.04 | 0.11 | 0.000 | 0.036 | 52.25 |
| | 5225 | 20.72 | 16.14 | 10.42 | 0.34 | 0.00 | 0.47 | 0.127 | 0.042 | 51.65 |
| | 5226 | 23.14 | 8.45 | 13.46 | 0.18 | 0.00 | 0.05 | 0.102 | 0.026 | 54.59 |
| BR2-G1 CM6 | 4054 | 29.47 | 12.79 | 7.74 | 0.05 | 0.00 | 0.29 | 0.000 | 0.048 | 49.57 |
| ATR-1 LG | 1789 | 18.35 | 13.63 | 7.80 | 0.15 | 0.04 | 0.21 | 0.04 | 0.07 | 59.65 |
| | 1790 | 16.45 | 11.06 | 8.53 | 0.07 | 0.04 | 0.10 | 0.03 | 0.04 | 63.65 |
| | 1795 | 16.49 | 10.55 | 8.09 | 0.07 | 0.03 | 0.12 | 0.02 | 0.04 | 64.57 |
| | 1796 | 15.53 | 12.96 | 7.25 | 0.09 | 0.05 | 0.13 | 0.04 | 0.06 | 63.87 |
| | 1800 | 18.17 | 10.90 | 9.24 | 0.06 | 0.02 | 0.13 | 0.05 | 0.06 | 61.32 |
| ATR-1 CM6 | 2179 | 20.33 | 13.95 | 4.50 | 0.04 | 0.02 | 0.23 | 0.026 | 0.244 | 60.58 |
| | 2180 | 22.49 | 15.06 | 5.26 | 0.04 | 0.02 | 0.12 | 0.055 | 0.253 | 56.66 |
| | 2185 | 21.28 | 11.87 | 4.97 | 0.04 | 0.02 | 0.26 | 0.074 | 0.230 | 61.21 |

| | | | | | | | | | | |
|---|---|---|---|---|---|---|---|---|---|---|
| | 2186 | 21.72 | 14.68 | 4.96 | 0.03 | 0.02 | 0.25 | 0.043 | 0.295 | 57.96 |
| | 2493 | 21.80 | 14.46 | 4.88 | 0.02 | 0.02 | 0.27 | 0.030 | 0.440 | 58.02 |
| | 2495 | 20.59 | 13.55 | 4.70 | 0.02 | 0.02 | 0.25 | 0.045 | 0.239 | 60.53 |
| | 2496 | 21.87 | 15.58 | 4.68 | 0.03 | 0.02 | 0.21 | 0.020 | 0.197 | 57.35 |
| | 2497 | 20.67 | 14.27 | 4.81 | 0.03 | 0.02 | 0.20 | 0.020 | 0.166 | 59.76 |
| | 2498 | 21.62 | 15.50 | 4.94 | 0.03 | 0.02 | 0.22 | 0.02 | 0.11 | 57.52 |
| Ringhals E | E6 | 21.29 | 14.83 | 6.15 | 0.39 | 0.13 | 0.05 | 0.12 | 0.01 | 57.01 |
| Ringhals N | N110 | 23.70 | 16.00 | 5.60 | 0.47 | 0.15 | 0.08 | 0.17 | 0.005 | 53.83 |
| | N270 | 18.20 | 15.59 | 4.36 | 0.39 | 0.17 | 0.14 | 0.26 | 0.03 | 60.84 |
| | N180 | 17.13 | 10.21 | 3.69 | 0.68 | 0.06 | 0.42 | 1.558 | 0.068 | 66.14 |
| Ginna Forging | - | 9.41 | 11.48 | 23.00 | 0.96 | 0.43 | 0.15 | 0.48 | 0.10 | 53.85 |

3.2.3 APT data under annealing

ATR-1 LG and CM6 alloys were annealed at 400°C up to 57 weeks and 425°C up to 29 weeks, respectively. Precipitates in LG (nominal composition 1.09at.%Mn-0.86%Ni-0.49%Si) totally dissolved after 1 week at both temperatures. Thus here, we'll only summarize data of CM6 (nominal composition 1.50at.%Mn-1.57%Ni-0.33%Si) alloy at annealing conditions, as shown in Table 3-4 and Table 3-5 show the compositions and results measured for each APT tip that is close to ATR-1 irradiated tip compositions (Table 3-1) under different temperatures for various annealing time. Again, this alloy was first irradiated at ATR-1 condition (flux of $2.3\times10^{18}m^{-2}s^{-1}$ to fluence of $1.1\times10^{25}m^{-2}$) before annealing.

Table 3-4 APT post-irradiation annealing data of CM6 at 425°C

| Time (week) | Alloy No. | Compositions (at.%) | | | Results | | |
|---|---|---|---|---|---|---|---|
| | | Ni | Mn | Si | Number density ($\times10^{23}$ $m^{-3}$) | Mean radius (nm) | Mole fraction (%) |
| 7 | 3742 | 1.64 | 1.41 | 0.36 | 1.04 | 2.06 | 0.38 |
| 17 | 3920 | 1.63 | 1.38 | 0.34 | 0.299 | 2.12 | 0.10 |
| 29 | 4328 | 1.66 | 1.34 | 0.38 | 0.247 | 2.64 | 0.14 |

Table 3-5 APT post-irradiation annealing data of CM6 at 400°C

| Time (week) | Alloy No. | Compositions (at.%) | | | Results | | |
|---|---|---|---|---|---|---|---|
| | | Ni | Mn | Si | Number density ($\times 10^{23}$ $m^{-3}$) | Mean radius (nm) | Mole fraction (%) |
| 29 | 4298 | 1.67 | 1.41 | 0.39 | 2.91 | 1.83 | 0.71 |
| 57 | 5094 | 1.67 | 1.36 | 0.41 | 1.81 | 1.79 | 0.42 |

3.3 Yield stress experimental data

Besides microstructural information, the yield stress of two alloys (LG & CM6) were also measured as irradiated at ATR-1 condition and also after annealing at various temperatures for 1 week, as shown in Table 3-6.

Table 3-6 Yield stress experimental data after 1 week post-irradiation annealing at various temperatures

| Temperature (°C) | **LG** | | **CM6** | |
|---|---|---|---|---|
| | **$\Delta\sigma_y$ (Mpa)** | Std Dev | **$\Delta\sigma_y$ (Mpa)** | Std Dev |
| ATR-1 As Irradiated | 573.6 | 34.1 | 718.0 | 37.5 |
| 350 | 496.2 | 35.3 | 658.7 | 27.6 |
| 375 | 453.3 | 36.7 | 643.7 | 38.7 |
| 400 | 350.0 | 36.8 | 549.1 | 29.6 |
| 425 | 94.8 | 23.6 | 360.0 | 24.8 |
| 450 | 54.9 | 26.9 | 54.3 | 28.1 |
| 550 | 0.0 | | 0.0 | |

# Chapter 4 Thermodynamic stability of Mn-Ni-Si precipitates in RPV steels

## 4.1 Chapter Abstract

The thermodynamic stability of MNSPs were studied with TCAL2 CALPHAD database for RPV relevant temperature of ~300°C as well as for temperature range 200-600°C. It was predicted by TCAL2 that two phases would form for RPV relevant compositions, one is the T3 or also called G-phase ($Mn_6Ni_{16}Si_7$) and the other is the T6 or also called $\Gamma_2$ phase ($Mn(Ni,Si)_2$). For some alloys, only one of them would form while for others both would form. The predicted precipitates compositions were in good agreements with APT data measured for alloys under irradiation. For these nano-size precipitates, it was found Gibbs-Thomson effect can decrease the mole fraction of MNSPs by a large percent. It was also found that the mole fraction of precipitates decreases as a function of temperature, precipitates in high Ni (1.6at.%) alloy can persist up until 500°C when increasing temperature while that in medium Ni (0.7at.%) alloy can only persist up until 400°C.

## 4.2 Introduction and motivation

To study the kinetics of MNSPs in RPV steels, the thermodynamic stability of MNSPs need to be studied first. In this chapter, CALPHAD method has been used to study the thermodynamic stability of MNSPs. CALPHAD can provide two pieces of key information for the CD model that will be used to study the kinetics of MNSPs: 1) the possible phases of MNSPs; 2) the bulk formation energy of MNSPs. Since these MNSPs are usually 1-2nm in radius, which is too small for any experimental techniques to determine the actual phases of these precipitates. Therefore, the possible phases of these precipitates have to be predicted by calculation. CALPHAD method is a good tool to make the prediction. In this thesis, the Thermo-Calc [81] Aluminum 2 (TCAL2) CALPHAD database [84] was used to establish the Fe-Mn-Ni-Si phase diagram as the thermodynamic foundation for this study.

4.3 Thermodynamic stability at ~300°C

Figure 4-1 shows the phase diagram of Mn-Ni-Si system at 550K. The TCAL2 database predicts that for typical RPV compositions, two intermetallic phases would form at equilibrium at around 300°C: the T3 or G-phase, ($Mn_6Ni_{16}Si_7$); and the T6 or $\Gamma_2$ phase, ($Mn(Ni,Si)_2$). The information of their respective crystal structures are shown in Table 4-1 [105,106], and the picture of their crystal structures are shown in Figure 4-2. Both these two phases are fcc structure. T3 is a stoichiometry phase while T6 is an ordered compound with Mn on one sublattice site while Ni and Si share the other sublattice site, as shown in Figure 4-1.

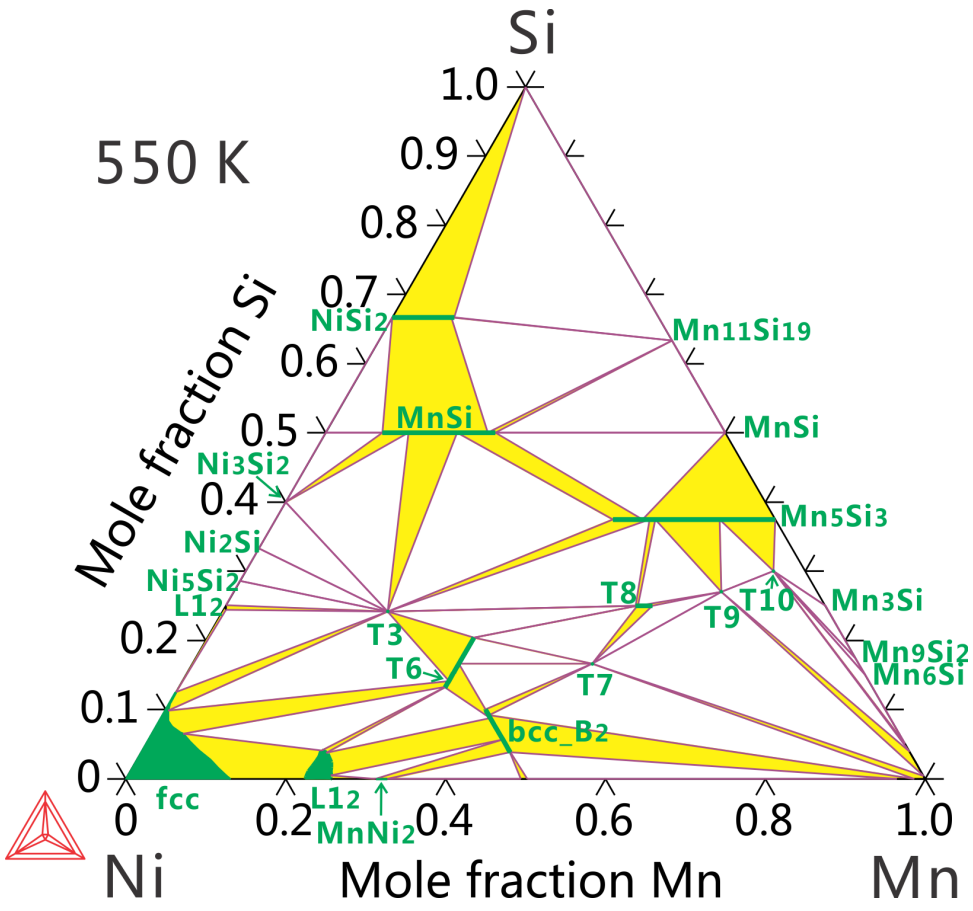


Figure 4-1 Phase diagram of Mn-Ni-Si system at 550K

Table 4-1 The crystal structures of Mn-Ni-Si phases in RPV steels at around 300°C.

| Phase | Composition | Space group | Type | Lattice constant, nm | Number of atoms in a unit cell |
|---|---|---|---|---|---|
| T3/G-phase | $Mn_6Ni_{16}Si_7$ | $Fm\bar{3}m$ | $Mg_6Cu_{16}Si_7$ | 1.108 | 116 |
| T6 | $Mn(Ni,Si)_2$ | $Fd\bar{3}m$ | $Cu_2Mg$ | 0.668 | 24 |

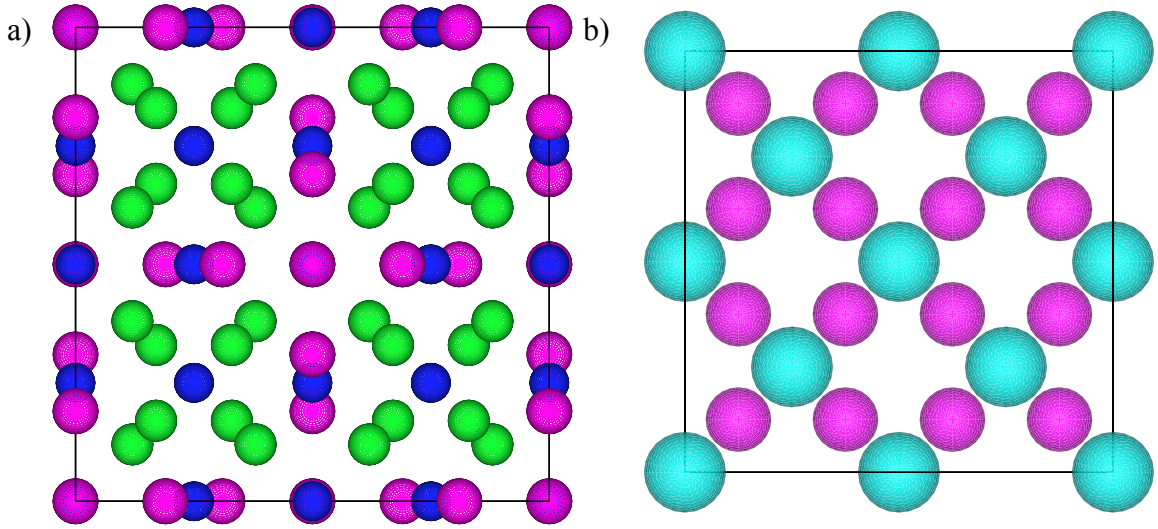


Figure 4-2 Crystal structure of a) G-phase (Magenta: Mn; Green: Ni; Blue: Si) b) T6 (Magenta: Mn; Cyan: Ni or Si)

Figure 4-3 a) shows that the predicted precipitate compositions compared to experimental results, for the average APT tip compositions and irradiation temperatures (see Table 3-1) in this study, are in good general agreements (with RMS of 5.17%, 7.54% and 6.13% for Ni, Mn and Si, respectively). The corresponding predicted equilibrium mole fraction (*f*) of each element in the MNSPs are shown in Figure 4-3 b). No comparison is made with experiment in this case, since the nm-scale MNSPs are not in equilibrium even at the highest fluence due to a significant Gibbs-Thomson effect ( see Sec. 4.4 ). Figure 4-3 c) shows the predicted MNSPs and their mole fractions for each alloy. In 6 out of the 10 cases the precipitates are the stoichiometric T6/$\Gamma_2$ phase. The T6 phase is generally associated with high Ni alloys (>1.6wt. %); however, one high Ni alloy had a

very small amount of T3/G phase. One of the intermediate Ni alloys contains stoichiometric T6 phase, one other contains stoichiometric T3 phase, while two others contain both T3 and T6 phases; one has about 62% T3 and 38% T6, and the other has about 12% T3 and 88% T6. Details aside, the major conclusion is that equilibrium MNSP intermetallic phases can readily form in the ≈ 270 to 300°C operating temperature regime of RPVs. This result is in contradiction with a number of first-principles and kinetic Monte Carlo studies arguing that MNSPs must be irradiation induced [35,36,107].

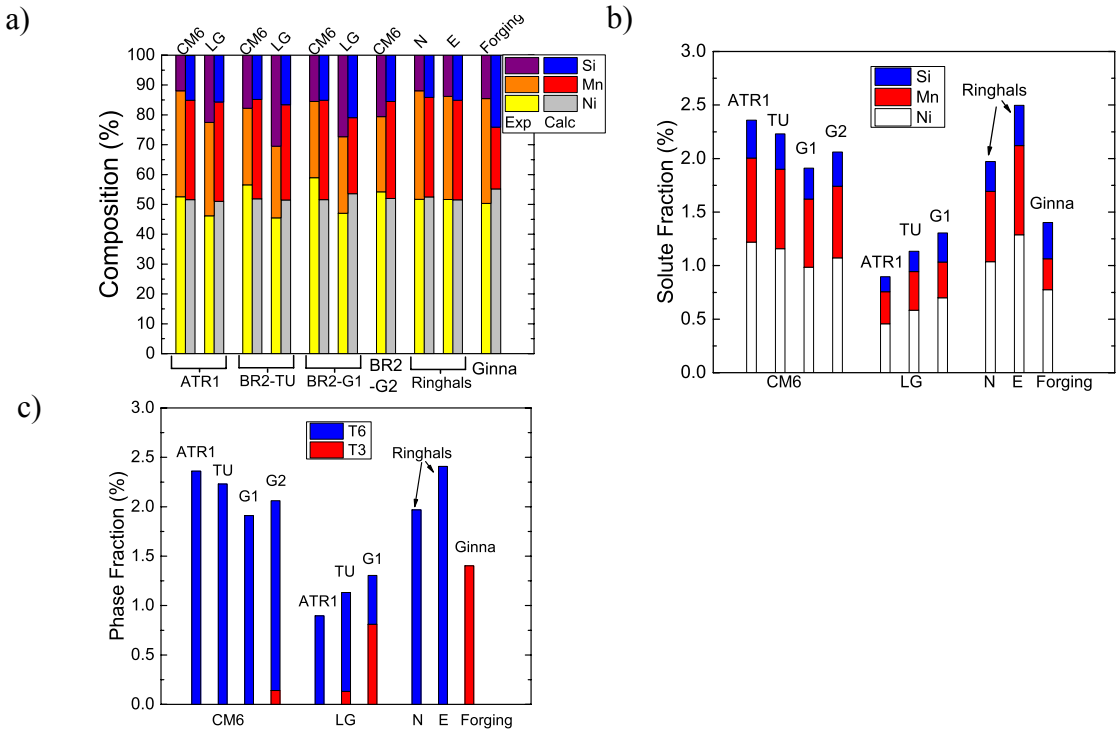


Figure 4-3 Thermodynamic equilibrium CALPHAD predictions.
a) precipitate compositions compared to APT data; b) precipitate solute mole fractions; c) phase selection fractions.

## 4.4 Gibbs-Thompson effect

Xiong et al. [46] calculated the mole fraction of MNSPs at equilibrium with two CALPHAD databases (TCAL2, UW1) and compared the results to very high fluence ATR-1 data. These alloys include both Cu-free and Cu-bearing alloys, with more information can be found in [46] and [24]. Since ATR-1 condition is irradiated to very high fluence that it can be safely assumed that it's in

the coarsening regime of the precipitates formation that almost all MNSPs have come out and Cu won't affect much the finale mole fraction of MNSPs. The mole fraction of precipitates from calculation results from both databases agree very well with experimental data. However, these calculations were done without considering the Gibbs-Thomson effect and these precipitates are all less than 2nm in radius, at which size the Gibbs-Thomson effect can be significant. Moreover, it has been recently recalibrated that the ATR-1 run-temperature is 320°C rather than 290°C as published in [24,46]. Here we updated the calculation results to 320°C and also estimated the effect of the Gibbs-Thomson effect by assuming mean radius of 1.5nm with the UW1 database. The interfacial energies chosen here are taken from the fits in Sec. 6.3.3, which are 175mJ·m$^{-2}$ for T6 phase and 185mJ·m$^{-2}$ for T3 phase. The result is shown in Figure 4-4. Calculation results at 320°C are lower than experimental data for all alloys, and a very significant impact can be seen from the Gibbs-Thomson effect, which causes the predicted mole fraction of precipitates to be much lower than experimental measured values. The origin of this lower predicted mole fraction of precipitates is not clear. One possibility is that the CALPHAD thermodynamics are not accurate at the relevant temperatures and compositions. To investigate if a change in the thermodynamics could correct the error in mole fraction the UW1 database was modified to match the experimental mole fraction at ATR-1 conditions. However, when comparisons were done for the other available experimental data at lower fluence shown in this paper, very large discrepancies for number density, mean radius and mole fraction were obtained even when using optimized fitting parameters, which result suggested that the higher mole fraction observed at the ATR-1 condition is not due to errors in the thermodynamic model. At present we believe that at least some part of the mole fraction of the precipitates are radiation induced at the experimental condition of very high flux and very high fluence, but further work is needed to verify this hypothesis.

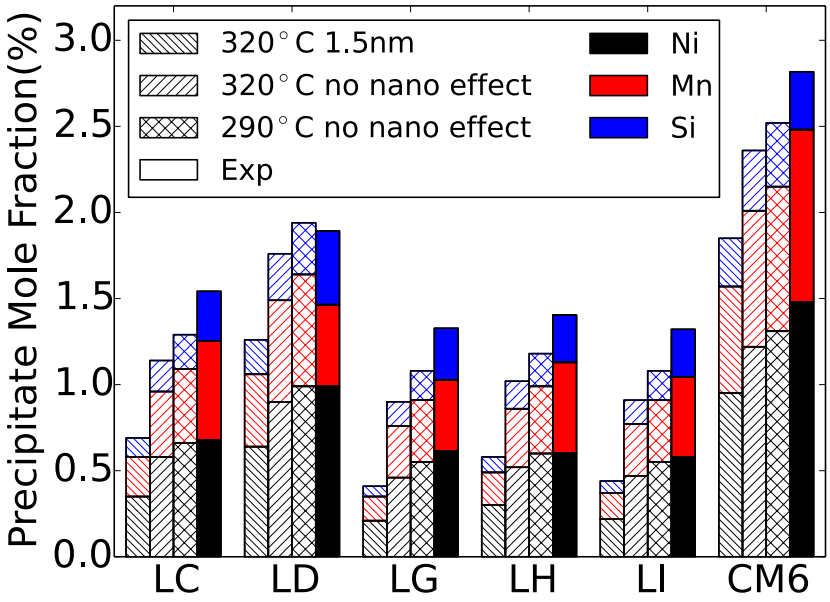


Figure 4-4 Gibbs-Thomson effect on precipitate mole fraction.

4.5 Temperature effect on the thermodynamic stability

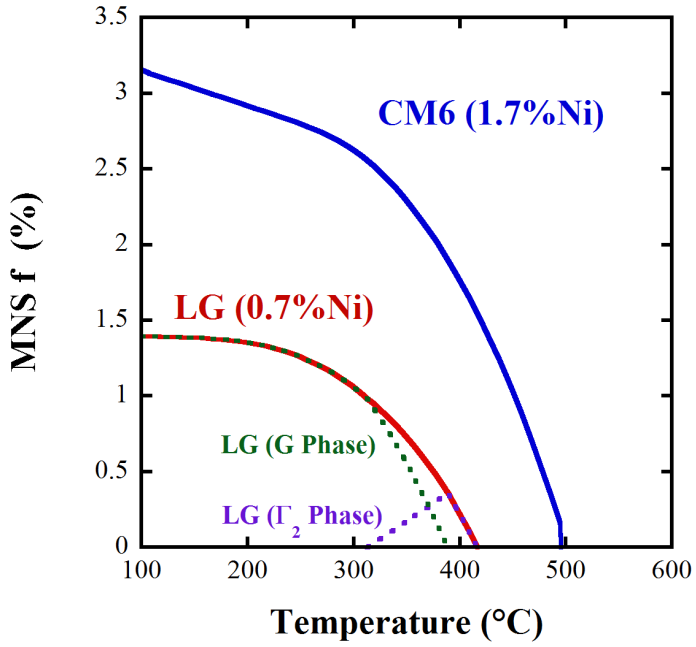


Figure 4-5 Equilibrium mole fraction of MNSPs in two Cu-free alloys as a function of temperature

In this section, we studied the effect of temperature on the formation of MNSPs in RPV steels. Figure 4-5 shows the equilibrium mole fraction of MNSPs in two Cu-free alloys with different Ni composition as a function of temperature. These two alloys, one (LG) contains medium Ni (0.7at.%) and the other contains high Ni (1.7at.%), almost cover the whole range of Ni composition in RPV steels. The mole factions of these phases decrease with increasing temperature. In high Ni CM6 alloy, only T6 phase form during the whole temperature range when precipitates form and persist up to 500°C. In medium Ni LG alloy, T3 phase forms at lower temperature up until 390°C and T6 phase forms from 310°C and up until 410°C.

In summary, the driving force of MNSPs decreases as the temperature increases. The fact that some of these precipitates dissolve during post-irradiation annealing at higher temperature doesn't necessarily mean these precipitates are irradiation induced under irradiation at around 300°C.

## 4.6 Summary

Based on the thermodynamic study of MNSPs with typical RPV alloy compositions, the major conclusions we obtained are:

1. About 1%-3% of MNSPs can form in RPV steels around 300°C at equilibrium state.
2. Two possible phases are predicted by the CALPHAD model: one is T3/G-phase ($Mn_6Ni_{16}Si_7$) and the other is T6/$\Gamma_2$ phase ($Mn(Ni,Si)_2$).
3. Gibbs-Thompson effect can decrease the mole fraction of these nm-scale MNSPs at equilibrium by a large percentage, which makes the prediction of mole fraction of precipitates even lower than what observed from experiments. It indicates either the CALPHAD database we use is not accurate enough for these dilute systems or some

radiation induced precipitates form at the very high flux and very high fluence condition the ATR-1 experimental condition.

4. The driving force of the formation of MNSPs decreases as the temperature increases. Precipitates in high Ni (1.6at.%) alloy can persist up until 500°C when increasing temperature while that in medium Ni (0.7at.%) alloy can only persist up until 400°.

# Chapter 5 Solubility of Fe in Mn-Ni-Si precipitates

## 5.1 Chapter abstract

APT analysis of MNSPs in RPV steels always show a large fraction of Fe in the precipitates, as can be seen from Table 3-3, however, there is still no common agreements in the community if Fe does exist in MNSPs or the large fraction of Fe observed is an artifact of APT. In this chapter, the solubility of Fe in G-phase ($Mn_6Ni_{16}Si_7$) forming in bcc Fe was investigated with *ab-initio* modeling as an example to study the solubility of Fe in MNSPs. Mn and Ni lattice sites were studied for the possibility of Fe to substitute. It is found that Fe has a very low solubility in G-phase forming in bcc-Fe when substituting either Mn or Ni atoms. Based on the result of this study, it can be concluded that the large fraction of Fe observed in precipitates with APT is mostly artifact of APT techniques.

## 5.2 Calculation details

To study the solubility of Fe in MNSPs, *ab initio* calculations were performed in the general framework of density functional theory (DFT) [85,86] using the Vienna *Ab initio* Simulation Package (VASP) [87–90]. The electron-ion interaction is described with the projector-augmented-wave (PAW) method [108] as implemented by Kresse and Joubert [109]. The exchange-correlation functional parameterized in the GGA [92] by Perdew, Burke and Ernzerhof (PBE) [110,111] is used. The Brillouin zone is sampled with MonkHorst-Pack [112] k-point meshes. All runs were done with spin-polarized calculations, and the magnetic moments of all elements are in ferromagnetic states.

The energies of pure elements (Mn, Ni, Si, Fe) were calculated first to be used as reference states. The cutoff energy was set to be 375 eV for Si and 410 eV for all other elements. K-point

mesh was set to be 4×4×4 for all elements. The crystal structure information and supercell size calculated are listed in Table 5-1.

Table 5-1 Crystal structure and number of atoms calculated for pure elements

| Element | Fe | Mn | Ni | Si |
|---|---|---|---|---|
| Structure name | Bcc | Cbcc | Fcc | Diamond |
| Space group | $Im\bar{3}m$ | $I\bar{4}3m$ | $Fm3m$ | $Fd\bar{3}m$ |
| Unit cell size | 2 | 58 | 4 | 8 |
| Supercell size | 54 | 58 | 108 | 64 |

Secondly, the chemical potential of Mn, Ni and Si in bcc Fe were calculated. For each element, a supercell with a total of 54 atoms (1X-53Fe, X=Mn, Ni and Si) were calculated with cutoff energy 410eV and K-point mesh of 4×4×4.

Thirdly, the formation energy of G-phase was calculated with a supercell of 116 atoms. The cutoff energy was 550eV and K-point mesh was set to be 2×2×2. The magnetic moment of Mn in G-phase is 3.5, and that for Ni is about 0.18 for atoms at position (0.169, 0.169, 0.169) and 0.08 for atoms at position (0.376, 0.376, 0.376).

Finally, the formation energy of crystal structures that Fe substitutes Mn or Ni in G-phase were calculated. Since there are two different Ni lattice sites in G-phase, thus a total of three different crystal structures were investigated, namely one when Fe substituting Mn and two when Fe substituting Ni. The magnetic moment of Fe in G-phase is 2.8, -1.0 and 0.7 when substituting Mn, Ni at position (0.169, 0.169, 0.169) and Ni at position (0.376, 0.376, 0.376), respectively.

## 5.3 Results

Table 5-2 lists the formation energy of G-phase and compared to that calculated from CALPHAD TCAL2 database at different temperatures. The reference state (here and all calculations in this chapter) is the energy of each element in their stable state at room temperature, e.g. bcc Fe, cbcc Mn, fcc Ni and diamond Si.

Table 5-2 Formation energy of G-phase calculated by VASP and compared with CALPHAD

| | **VASP** | **CALPHAD (300K)** | **CALPHAD (700K)** |
|---|---|---|---|
| Formation Energy (eV/atom) | -0.43 | -0.49 | -0.38 |

According to [113], in which it describes the crystal structure of $Mg_6Si_7Cu_{16}$, which shares the same crystal structure as G-phase, Mn occupies position (0.179, 0.0, 0.0) and Ni occupies two positions in unit cell, namely (0.169, 0.169, 0.169) and (0.376, 0.376, 0.376), respectively. Thus, the heat of solution of Fe in G-phase when Fe substitutes all these three positions were calculated. The results are shown in Table 5-3. Please note that the results shown in Table 5-3 and later in this section are for G-phase precipitates formed in bcc Fe matrix, therefore the elements being substituted (Mn or Ni) will become solutes in bcc Fe matrix rather than their stable states.

Table 5-3 Heat of solution of Fe in G-phase formed in bcc-Fe at 0K

| Lattice site label substituted by Fe | Lattice site coordinate | Energy (eV/atom) |
|---|---|---|
| Mn | (0.179, 0.0, 0.0) | 0.51 |
| $Ni_1$ | (0.169, 0.169, 0.169) | 0.65 |
| $Ni_2$ | (0.376, 0.376, 0.376) | 0.69 |

Based on the results listed in Table 5-3, the heat of solution of Fe as well as solubility of Fe in G-phase at high temperatures were calculated. At high temperatures, depending on Mn and Ni composition in bcc Fe matrix, the heat of solution of Fe and Fe solubility will also change. According to Henry's law, for dilute solution, the heat of solution of Fe in G-phase can be calculated by

$$\Delta H = \Delta H_0^i + kTln(X^i) \text{ (i=Mn, } Ni_1\text{, } Ni_2\text{)} \quad (5\text{-}1)$$

Here $\Delta H_0^i$ is the heat of solution of Fe in G-phase at 0K, which is listed in Table 5-3, *i* denotes the different lattice sites that Fe can substitutes, and $X^i$ is the composition of Mn or Ni in bcc-Fe matrix. The solubility of Fe in G-phase can be calculated by

$$S = \exp\left(-\frac{\Delta H}{kT}\right) \quad (5\text{-}2)$$

Figure 5-1 and Figure 5-2 shows the heat of solution and solubility of Fe in G-phase as a function of Mn composition in matrix when substituting Mn in G-phase at three different temperatures, namely 300°C, 500°C and 700°C. From Figure 5-2 we can see that the solubility of Fe in G-phase is very low when substituting Mn atoms, especially at RPV running temperature of 300°C. Please note the typical composition of Mn in RPV steels is 0.6-1.6at.%. From Figure 5-2 b) we can see that the solubility of Fe in G-phase (< 1%) is much lower than what observed in APT (~60%) at RPV relevant temperature and composition.

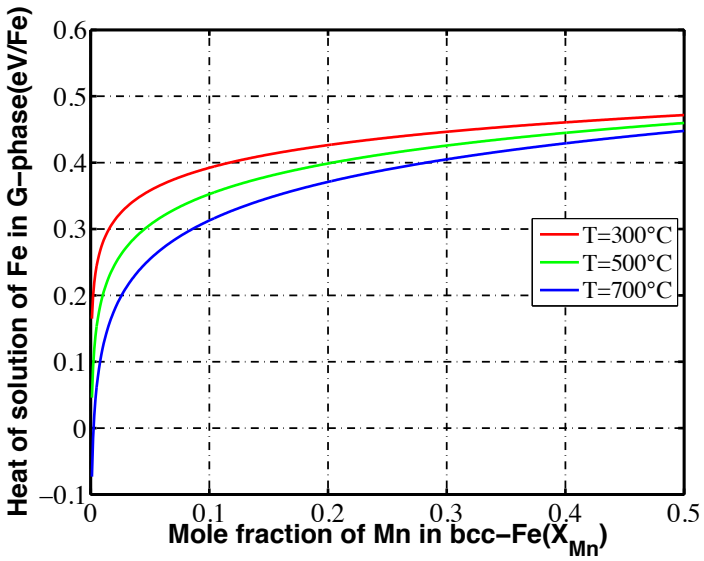


Figure 5-1 Heat of solution of Fe in G-phase as a function of Mn composition in alloys when replacing Mn

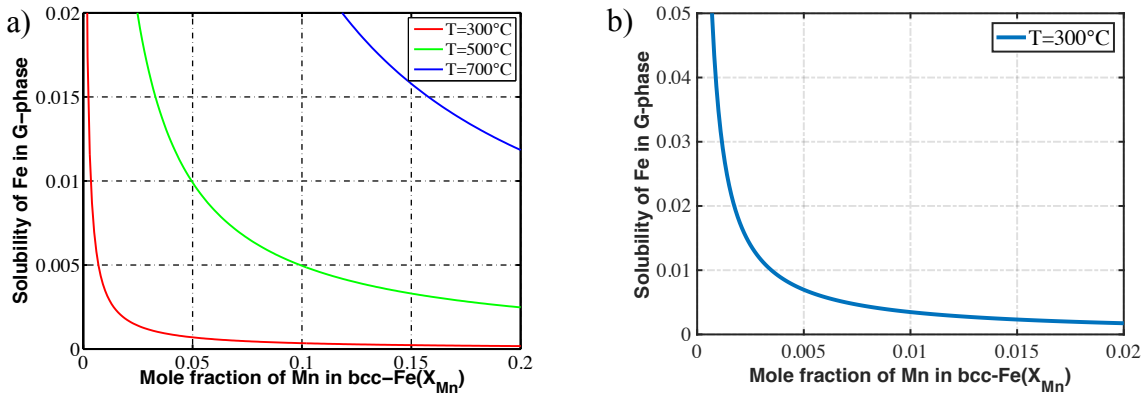


Figure 5-2 Solubility of Fe in G-phase as a function of Mn composition in alloys when substituting Mn atoms: a) Multiple temperatures; b) RPV relevant temperature and composition.

Similarly, we also explored the solubility of Fe in G-phase when substituting Ni atoms. Since the energy cost is lower at Ni position 1, thus we will do calculations regarding this position only. Figure 5-3 and Figure 5-4 shows the results. From Figure 5-4 we can see that the solubility of Fe in G-phase when substituting Ni atom (<0.1%) is also very low, and is even lower than that when substituting Mn atoms (<1%).

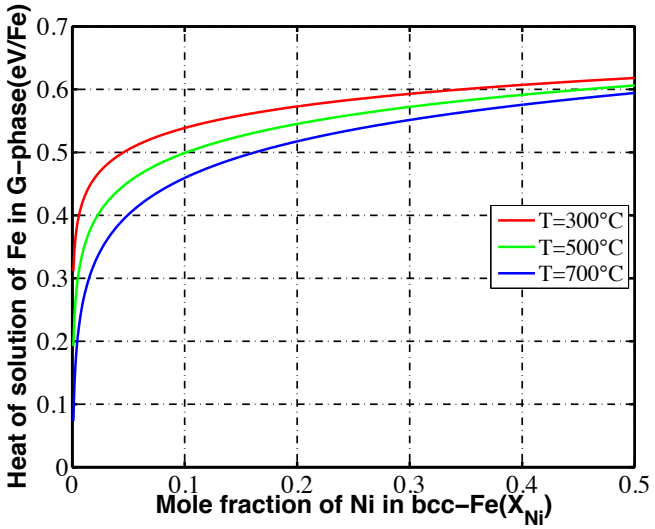


Figure 5-3 Heat of solution of Fe in G-phase as a function of Ni composition in alloys when substituting Ni

a) b)

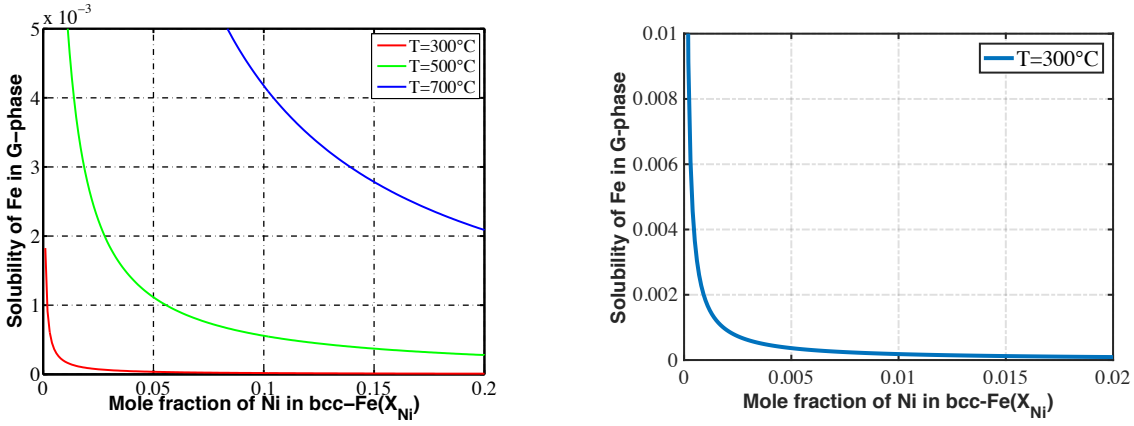


Figure 5-4 Solubility of Fe in G-phase as a function of Ni composition in alloys when substituting Ni atoms: a) Multiple temperatures; b) RPV relevant temperature and composition.

## 5.4 Summary

Based on *ab initio* calculation results, the major conclusion we obtained are:

1. Solubility of Fe in G-phase forming in bcc-Fe matrix is less than 1.0% when substituting Mn and less than 0.1% when substituting Ni atoms for typical RPV composition and temperature.
2. The solubility obtained is much less than what is observed in APT experiments, which is bout 50-70% Fe. Therefore, the large amount of Fe observed in MNSPs with APT is highly possible an artifact of APT.

# Chapter 6 Modeling of Mn-Ni-Si precipitates under irradiation

## 6.1 Chapter Abstract

A semi-empirical cluster dynamics model was developed to study the evolution of MNSPs in low-Cu RPV steels under irradiation. The model predictions are in semi-quantitative agreement with systematic Mn, Ni and Si composition variations in the alloys characterized by APT, including a sensitivity to local tip-to-tip variations even in the same steel. The model predicts that heterogeneous nucleation plays a critical role in MNSP formation at lower alloy Ni contents, and that even small irradiation temperature variations can have a large effect on the precipitate evolution. Single variable assessments of compositional effects show that Ni plays a dominant role, while within typical RPV steel ranges, Mn and Si have a finite, but smaller effect. The delayed evolution of MNSPs, which have been called late blooming phases, is reasonably predicted by the model. For purposes of illustration, rather than prediction, the effect of MNSPs on transition temperature shifts are presented based on well-established microstructure-property and property-property models.

## 6.2 Chapter overview

In this chapter, the evolution of MNSPs in low-Cu RPV steels under irradiation has been studied with cluster dynamics model. Sec.6.3 illustrates the parameters used in the model and how each of them was obtained. Sec.6.4 defines how each of the output properties (e.g. number density, mean radius, mole fraction and volume fraction) was calculated. Sec.6.5 shows the comparison between simulation results and experimental data. Sec.6.6 shows the effect of heterogeneous nucleation on cascade on the evolution of MNSPs. Sec.6.7 and Sec.6.8 studied the effect of composition and temperature on the evolution of MNSPs, respectively. And at last, Sec.6.9 shows

the effect of MNSPs on the embrittlement of RPV steels for RPV extended life of 80 years and longer.

## 6.3 Input and parameters

The parameters needed for cluster dynamics model can be generally divided into three parts:

1. Thermodynamic parameters, which includes equilibrium solute product of each precipitate phase in alloys and interfacial energies between MNSPs and the matrix. Here the equilibrium solute products will be obtained from CALPHAD database and will be illustrated in detail in Sec. 6.3.1. The interfacial energies are treated as fitting parameters and Sec. 6.3.3 will detail how we obtain them.
2. Parameters for calculating diffusion coefficients under irradiation, which includes thermal diffusion coefficients of solutes (Mn, Ni and Si) and solvent (Fe) in α-Fe matrix, and parameters for radiation enhanced diffusion model. Here the thermal diffusion coefficients will be obtained from literature experimental values, as illustrated in Sec. 6.3.2. Other parameters used for radiation enhanced diffusion model are summarized in Sec. 6.3.4.
3. Parameters for heterogeneous nucleation model, which includes equilibrium solute product, reference solute product, cascade cross section, heterogeneous nucleation size and cascade cluster production efficiency factor. The equilibrium solute product, as mentioned in thermodynamic parameters, will be illustrated in Sec. 6.3.1. The reference solute product and cascade cross section will be given in Sec. 6.3.4. And the heterogeneous nucleation size and cascade cluster production efficiency factor are fitting parameters, which will be illustrated together with other fitting parameters in Sec. 6.3.3.

### 6.3.1 Equilibrium solute product

One important parameter needed for the cluster dynamics modeling is the equilibrium solute product $K_{sp}$ in Eq. (2-23), which is defined in Eq. (2-24). It is equivalent to the bulk formation energy of precipitates. As mentioned in Sec. 4.3, two phases are predicted by CALPHAD database that will form with typical RPV compositions, one is G-phase (T3) and the other is $\Gamma_2$-phase (T6). G-phase ($Mn_6Ni_{16}Si_7$) is a stoichimetric phase with fixed composition while the composition of Ni and Si in $\Gamma_2$-phase ($Mn(Ni,Si)_2$) might change under different conditions. Here we calculated the Ni and Si composition in $\Gamma_2$-phase and the equilibrium solute products of the two phases at different temperatures corresponding to the nominal experimental conditions with TCAL2 database [84] (as described in Sec. 4.3). The equilibrium solute product of both phases and Ni composition in $\Gamma_2$-phase are listed in Table 6-1. To obtain these values, six alloy compositions (ATR-1 alloys in [46]) are calculated for each temperature. Please note, it doesn't matter what exact composition were chosen to do the calculations, as long as they cover the typical RPV steel compositions, they will give the same results shown in Table 6-1, as can be seen from the very small standard deviation of both the solute products and Ni composition in $\Gamma_2$-phase.

Table 6-1 The equilibrium solute product ($\overline{K_{sp}}$) for the G-phase (T3) and $\Gamma_2$-phase (T6) and Ni composition in T6 at different temperatures.

| Temperature (°C) | G-phase (T3) | | $\Gamma_2$-phase (T6) | | | |
|---|---|---|---|---|---|---|
| | Equilibrium solute product ($\times10^{-3}$) | Standard deviation ($\times10^{-5}$) | Equilibrium solute product ($\times10^{-3}$) | Standard deviation ($\times10^{-5}$) | Ni composition (%) | Standard deviation (%) |
| 280 | 1.96 | 2.12 | 2.33 | 1.66 | 51.2 | 0.37 |
| 284 | 2.12 | 2.56 | 2.53 | 7.54 | 52.0 | 0.70 |
| 290 | 2.21 | 3.32 | 2.56 | 6.30 | 51.5 | 0.53 |
| 300 | 2.45 | 3.93 | 2.82 | 1.57 | 51.3 | 0.36 |
| 320 | 3.02 | 4.99 | 3.42 | 2.62 | 51.0 | 0.02 |

6.3.2 Thermal diffusion coefficients

Here the thermal diffusion coefficients $D^{th}$ are given by the standard expression

$$D^{th} = D_0^{th} \exp\left(-\frac{Q}{kT}\right) \quad (6\text{-}1)$$

For the self and impurity diffusion coefficients during ferromagnetic state, Ruch et al. [114] proposed a model for $D(T)$ in which the temperature dependence is described assuming a constant value for the prefactor ($D_0$) and a temperature dependence of activation energy originating from the effect of magnetic disorder. The ferromagnetic activation energy is a function of paramagnetic activation energy with the formula

$$Q^f = Q^p(1 + \alpha s^2) \quad (6\text{-}2)$$

where $Q^f$ is the activation energy in the fully ordered ferromagnetic state at zero temperature, $Q^p$ is the activation energy in disordered paramagnetic state, $s$ is the reduced magnetization at any finite temperature, which is a function of temperature and was reported by Potter [115].

Unfortunately, there is essentially no diffusion data for Mn, Ni, and Si in Fe at the relevant LWR temperatures of about 300°C. Thus estimating $D^{th}$ requires a large extrapolation from high temperature. Furthermore, the low temperature $D^{th}$ must account for the effects of changing ferromagnetic state on the migration energetics of the solute below the Curie temperature. Although self-diffusion coefficients of Fe have been studied by a number of researchers, for example [116–122], there is very limited experimental data on the thermal diffusion coefficients of Mn, Ni, and Si solutes in ferromagnetic Fe. Indeed, to our knowledge, there is only one dataset for Mn [123], one for Ni [124], and none for Si. Although there are calculation results of diffusion coefficients at low temperature from DFT [125,126], we chose to use experimental data to avoid possible uncertainties in the DFT models. In both cases small errors in migration energies can cause large differences of diffusion coefficients at the relevant low temperatures.

Therefore, we have developed an approximate, but internally consistent, approach to estimate together the diffusion coefficient for Fe and all the solutes based on constant activation energy models fit to data for the ferromagnetic host Fe matrix. The reason we do this will be explained in the following paragraphs.

Recall Eq. (2-27) for radiation enhanced diffusion coefficients, since thermal diffusion coefficients are negligible compared to radiation enhanced diffusion coefficients, thus the radiation enhanced diffusion coefficients are proportional to the ratios of $D^{th}/D^{Fe}$. Assuming Arrhenius expressions with temperature dependent activation energies that depend on the magnetic state of Fe [115–122] for diffusion this ratio can be explicitly written in the following equation

$$\frac{D_i^{th}}{D_{Fe}} = \frac{D_{0\mathrm{i}}^{th}\, exp\left(-\frac{Q_i^p(1+\alpha_i s^2)}{RT}\right)}{D_{0Fe}\, exp\left(-\frac{Q_{Fe}^p(1+\alpha_{Fe}s^2)}{RT}\right)} = \frac{D_{0\mathrm{i}}^{th}}{D_{0Fe}} \exp\left(-\frac{Q_i^p(1+\alpha_i s^2) - Q_{Fe}^p(1+\alpha_{Fe}s^2)}{RT}\right) = \frac{D_{0\mathrm{i}}^{th}}{D_{0Fe}} \exp\left(-\frac{C}{RT}\right) \qquad (6\text{-}3)$$

where $C = Q_i(1 + \alpha_i s^2) - Q_{Fe}(1 + \alpha_{Fe}s^2)$. The best way to model radiation enhanced diffusion coefficients given approximate values of the thermal diffusion coefficients is therefore to use approximations which yield the more accurate value for the term C. More precisely, if we had all the temperature dependent activation energies and evaluated the *C* parameter at the relevant RPV temperature (which we denote $T_2$) (with the magnetic moment at this temperature $s_2(T_2)$) then we would get the correct true value of *C*, which we call $C_{true} = -[Q_i(1 + \alpha_i s_2^2) - Q_{Fe}(1 + \alpha_{Fe}s_2^2)$. Whatever approach we use should yield a *C* value as close to $C_{true}$ as possible. As mentioned above, due to limited data we are using impurity *i* diffusion coefficients with a fixed activation energy, which is taken at some temperature $T_1 > T_2$ with magnetic moment $s_1(T_1)$.

Given the partial data for the impurities, it is not clear the best approximate approach to use with respect to the Fe diffusivity, for which we have very limited data over a wide temperature range. We consider two logical approaches: (a) we use the temperature dependent activation

energy for Fe and (b) we use a temperature independent activation energy for Fe taken from data at approximately $T_1$. For case (a) we obtain a value of $C_a = [Q_i(1+\alpha_i s_1^2) - Q_{Fe}(1+\alpha_{Fe} s_2^2)]$ and for case (b) we obtain a value of $C_b = [Q_i(1+\alpha_i s_1^2) - Q_{Fe}(1+\alpha_{Fe} s_1^2)]$. The changes in $C$ from the ideal true value for the two cases are therefore $C_a - C_{true} = Q_i\alpha_i(s_1^2 - s_2^2)$and $C_b - C_{true} = (Q_i\alpha_i - Q_{Fe}\alpha_{Fe})(s_1^2 - s_2^2)$. If we make the reasonable assumption that Fe and its impurity have somewhat similar values of activation energy and $\alpha$ parameter then it is clear that $(Q_i\alpha_i - Q_{Fe}\alpha_{Fe})$ is likely to be much closer to zero than $Q_i\alpha_i$, and that therefore method (b) is likely to be significantly better than method (a). This argument can be summarized by noting that by treating the Fe activation energy as temperature independent, in a manner consistent with the approximate treatment of the impurity, we maximize cancellation of errors more that by using the more accurate temperature-dependent Fe activation energy model. Thus we use approach (b) in developing the RED model.

As for Si, since no experiments have been done for the diffusion of it in ferromagnetic state Fe, an estimation of ferromagnetic activation energy is done by using the ratio between ferromagnetic energy ($Q_c^f$) and paramagnetic energy ($Q^p$) of Ni in Fe. Ni is chosen here because both ferromagnetic and paramagnetic state diffusion are measured by the same researcher and the pre-factors given are very close to each other in these two states, as can be seen from Table 6-2. Thus, the activation energy of Si in ferromagnetic Fe will be calculated from the value measured at paramagnetic state [127] ($Q^p$(Si) = 220.5 kJ/mol) and adjusted by the ratio 1.05 given in Table 6-2.

Table 6-2 Diffusion coefficients of Ni in alpha-Fe measured in paramagnetic and ferromagnetic state

| State | $D_0$ ($cm^2/s$) | $Q_c^f$ (kJ/mol) | Ratio $Q^f/Q^p$ | Reference |
|---|---|---|---|---|
| Paramagnetic | 1.3 | 234.3 | 1.05 | [124] |
| Ferromagnetic | 1.4 | 245.6 | | |

According to discussion above, the final thermal diffusion coefficients of Mn, Ni, Si and Fe in ferromagnetic Fe used in this paper are summarized in Table 6-3.

Table 6-3 The thermal diffusion coefficients used in this study.

| Element | $D_0$ ($\times 10^{-4}$ $m^2 \cdot s^{-1}$) | Q ($kJ \cdot mol^{-1}$) | Reference |
|---|---|---|---|
| Mn | 1.49 | 234.0 | [123] |
| Ni | 1.40 | 245.6 | [124] |
| Si | 0.78 | 231.5 | [127] |
| Fe | 27.5 | 254.0 | [116] |

### 6.3.3 Parameter fitting and model optimization

There are a total of four fitting parameters in the model, namely the heterogeneous nucleation size, cascade cluster production efficiency factor and two interfacial energies. These fitting parameters are identified by the variables, $n_{het}$, $\alpha$, $\gamma_{T3}$, and $\gamma_{T6}$ in the main text, respectively. To obtain these parameters, we meshed each parameter with different values, and the simulation results of each set of parameters were compared to experimental data to obtain the optimal parameters. Optimization was done by minimizing an integrated cost function which contains a combination of root mean square deviation (RMSD) of the predictions from experimental results for mean radius, mole fraction, and number density, as described below.

The RMSD for mean radius and mole fraction is measured as a percent error vs. experiment, which is defined by

$$RMS(P) = 100\% \times \sqrt{\frac{\sum_{i=1}^{n}\left[\left(P_i^{calc} - P_i^{exp}\right)/P_i^{exp}\right]^2}{n}} \quad (6\text{-}4)$$

where $P$ is either mean radius or mole fraction, $P_i^{calc}$ is the calculation result of property $P$ for data point $i$, $P_i^{exp}$ is the experimental result of property $P$ for data point $i$, and $n$ is the total number of data points. The number density is compared by calculating the RMSD of its log with the following formula

$$RMS(logN) = \sqrt{\frac{\sum_{i=1}^{n}(\log(N_i^{Calc}) - \log(N_i^{Exp}))^2}{n}} \quad (6\text{-}5)$$

The reason that number density is compared in a different way is because number density measured by experiments cover a large range ($3\times10^{23}$-$3\times10^{24}$), and calculation results are targeted at obtaining the same order of magnitude rather than the smallest percent error for number density when compared to experimental data. For example, compare two calculation results of $2\times10^{24}$ and $2\times10^{23}$ to an experimental measured value of $1\times10^{24}$. While the percentage difference is 100% vs 80%, $2\times10^{24}$ is probably a more physical prediction better than $2\times10^{23}$).

Then the optimal set of parameters is picked by a combined cost function $RMS_{combine}$ incorporating all three properties with scaling factors for each one chosen so that the targeted error contributed about one to $RMS_{combine}$. The target errors are 2x in number density and 0.2 in fractional error of mean radius and volume.

$$RMS_{Combine} = \frac{10^{RMS(logN)}}{2} + \frac{\mathrm{RMS(R)}}{0.20} + \frac{\mathrm{RMS(V)}}{0.20} \quad (6\text{-}6)$$

Now we search the space of parameters to find the set that give the smallest value of $RMS_{Combine}$.

As described in Sec. 3.2.2, a total of 10 alloys are studied here, with a total of 36 data points. However, when we compared calculated results to experimental data for the ATR-1 condition, we either underestimated the formation of MNSPs or they did not form at all, suggesting that these data are influenced by physics not included in our model. Thus this very high temperature and high-flux condition was excluded from the parameter fitting process. Possible reasons for the observed differences between ATR-1 and other conditions are discussed in Sec.6.5. In summary, a total of 8 alloys (BR2-G1CM6 and LG, BR2-TU CM6 and LG, BR2-G2 CM6, Ringhals E and N, and Ginna Forging) with 22 tips were used in the parameter fitting process.

A grid of 10×7×8×8 points, with each number corresponding to a range of that many values for one of the parameters, was run to obtain the optimal set of parameters. More specifically,

heterogeneous nucleation size was gridded from 40-85 atoms with an increment of 5 atoms, the heterogeneous nucleation rate generation coefficient was gridded from 2.4-16.8×$10^{-3}$ clusters per cascade with an increment of 2.4×$10^{-3}$ cluster per cascade, the interfacial energy of T3 phase was gridded from 160-195mJ/$m^2$ with an increment of 5mJ/$m^2$, and the interfacial energy of T6 phase was gridded from 145-180mJ/$m^2$ with an increment of 5mJ/$m^2$. Table 6-4 shows the final values of fitting parameters that gives the minimum RMSD. The RMSD for number density ($10^{RMS(logN)}$), mean radius and mole fraction at this set is 1.85, 22.52% and 51.48%, respectively.

Table 6-4 Values of fitting parameters in CD model

| | |
|---|---|
| Heterogeneous nucleation size ($n_{het}$) | 80 |
| Cascade cluster production efficiency factor ($\alpha$) | 4.8×$10^{-3}$ |
| Interfacial energy of T3 phase ($\gamma_{T3}$, J·$m^{-2}$) | 0.185 |
| Interfacial energy of T6 phase ($\gamma_{T6}$, J·$m^{-2}$) | 0.175 |

Note that the numerical fit values are all physically reasonable. In particular, the nucleation size $n_{het}$ is relatively small, consistent with it being formed during cascade aging. Similarly, $\alpha$ is also quite reasonable, consistent with just a small fraction of cascades (~1%) producing heterogeneous nucleation sites at low supersaturations, and is a small fraction of the 5-7 interstitial loops produced by cascades. Both the T3 and T6 interfacial energies are quite similar, consistent with their similar compositions. Furthermore, both are significantly lower than the Cu-Fe interfacial energy (typically taken to be about 0.4 J·$m^{-2}$ [16]), which is consistent with the phenomena observed in experiments that Mn, Ni and Si are usually segregated to and outside the CRPs interface [21–24].

### 6.3.4 Other parameters

All other parameters used in the model are listed in Table 6-5. Most of them were obtained from two papers [102,128]. Please note here the reference solute product ($K_{sp}^0$) is an arbitrary value

picked around the equilibrium solute product around RPV running temperatures, the exact value used won't affect the model, since it will be compensated by the fitting parameter of cascade cluster production efficiency factor $\alpha$ (see Eq. (2-26)). The reason we pick a number as reference solute product here is to give $\alpha$ some physical meaning, which will mean the fraction of clusters produced per cascade at equilibrium state.

Table 6-5 The model parameters used in calculating the radiation enhanced diffusion coefficient and heterogeneous nucleation in cluster dynamics model.

| | |
|---|---|
| SIA – vacancy recombination radius ($r_v$, nm) | 0.57* [102] |
| Fraction of vacancies and SIA created per dpa ($\xi$) | 0.4 [102] |
| Displacement-per-atom (dpa) cross-section ($\sigma_{dpa}$, $m^2$) | $1.5\times10^{-25}$ [102] |
| Atomic volume ($\Omega_a$, $m^3$) | $1.18\times10^{-29}$ |
| Vacancy diffusion coefficient pre-exponential factor ($D_v$, $m^2\cdot s^{-1}$) | $1\times10^{-4}$ *[128] |
| Vacancy migration energy ( $E_v^m$, eV) | 1.3* [128] |
| Dislocation sink strength (dislocation density) ($\rho$, $m^{-2}$) | $2\times10^{14}$ [102] |
| Flux effect scaling exponential factor ($p$) | 0.2 [31, 51] |
| Cascade cross section ($\sigma_{cas}$, $m^2$) | $2\times10^{-28}$ [51] |
| Reference solute product ($K_{sp}^0$) | $2.4\times10^{-3}$ |

*These values are used in calculating $g_s(\phi_r)$. $g_s(\phi_r)$ is very close to one and largely insensitive to the exact values used.

## 6.4 Presentation of the results

The CD model predicts the precipitate number density $N$, size distribution $N(r)$, mean radius $\bar{r}$, and mole fraction $f$ as a function of fluence.

In this thesis we will define the number density of a precipitate by the formula

$$N = \sum_{i=1}^{p} N_i \qquad (6\text{-}7)$$

where $N_i$ is the number density of each phase, and $p$ is the total number of phases considered ($p$=2 here).

We determine the mean radius of a particle size distribution the way it is calculated in APT experiments by the formula

$$\overline{r_i} = \sqrt[3]{\frac{3\bar{n}V_p}{4\pi}} \quad (6\text{-}8)$$

where $V_p$ is the average atomic volume in the precipitates, and $\bar{n}$ is the average number of atoms in clusters.

$V_p$ is calculated by the formula

$$V_p = \frac{V_{cell}}{n_p} = a_p^3/n_p \quad (6\text{-}9)$$

where $a_p$ is the lattice constant of the precipitate unit cell, and $n_p$ is the number of atoms in a unit cell.

$\bar{n}$ is calculated by the formula

$$\bar{n} = \frac{\sum_{n_{min}}^{n_{max}} nN_n}{N} \quad (6\text{-}10)$$

where $n$ is the number of atoms in a cluster, $N_n$ is the number density of cluster with $n$ atoms, $n_{min}$ is the minimum cutoff size of clusters considered. And $n_{max}$ is the maximum cluster size considered in this work, which is 50000 (about 5nm in radius), and it is well beyond the largest radius observed in experiments and the number density is zero for all the calculations. The determination of $n_{min}$ is informed by experimental measurements by APT or hardening model. Based on a detection efficiency of about 37%, APT measurements do not detect solute clusters smaller than about 32-80 atoms. Therefore, based on the minimum cluster size detected for each condition, the cutoff size for CD output is 65 atoms for ATR-1, BR2-TU CM6 and Ringhals N180, 32 atoms for BR2-TU LG, BR2-G1and BR2-G2, and 43 atoms for other Ringhals and Ginna alloys, respectively. The cutoff size used for analysis of composition and temperature effects, where no direct comparison to experiment is presently being made, is simply set to be 32 atoms, which is the minimum size used in the APT analysis. Finally, we exclude clusters sizes below 40 atoms (~0.49nm in radius) for all mechanical property calculations in Sec.6.9. The cutoff size for mechanical property calculations is chosen based on that recommended in the Russell-Brown

model [57]. Please also note that the exact cutoff size (below 65 atoms) chosen here will only have some minimal effects on the number density and mean radius of precipitates, but will not affect the mole fraction of precipitates. Detail comparison regarding the effect of cutoff size will be given in Sec. 6.5.

We determine the mole fraction of a precipitate by the formula

$$f_i = \Omega_a \sum_n nN_n \times 100\% \quad (6\text{-}11)$$

where $\Omega_a$ is the atomic volume of matrix.

The volume fraction of a precipitate is determined by the formula

$$f_{V_i} = V_p \sum_n nN_n \times 100\% \quad (6\text{-}12)$$

and the mean radius of the system is defined by

$$\bar{r} = \frac{\sum_{i=1}^{p} \bar{r}_i N_i}{N} \quad (6\text{-}13)$$

where $\bar{r}_i$ is the mean radius of each phase calculated from Eq. (6-8).

The total mole fraction of the system is defined by

$$f = \sum_{i=1}^{p} f_i \quad (6\text{-}14)$$

where $f_i$ is the mole fraction of each phase calculated from Eq. (6-11).

The total volume fraction of the system is defined by

$$f_V = \sum_{i=1}^{p} f_{V_i} \quad (6\text{-}15)$$

where $f_{V_i}$ is the volume fraction of each phase calculated from Eq. (6-12).

## 6.5 Comparison with experimental results

Figure 6-1 and Figure 6-2 show the evolution of MNSPs ($N$, $\bar{r}$ and $f$) as a function of fluence for all the alloys listed in Table 3-1 and Table 3-2. The bands represent the range of outputs obtained by simulating individual APT tip compositions. Note that the CD model predicts that the number density and mole fraction of MNSPs in the lower Ni, higher temperature ATR-1 LG (MHH coding) are so low that they are not visible on scales used in Figure 6-1.

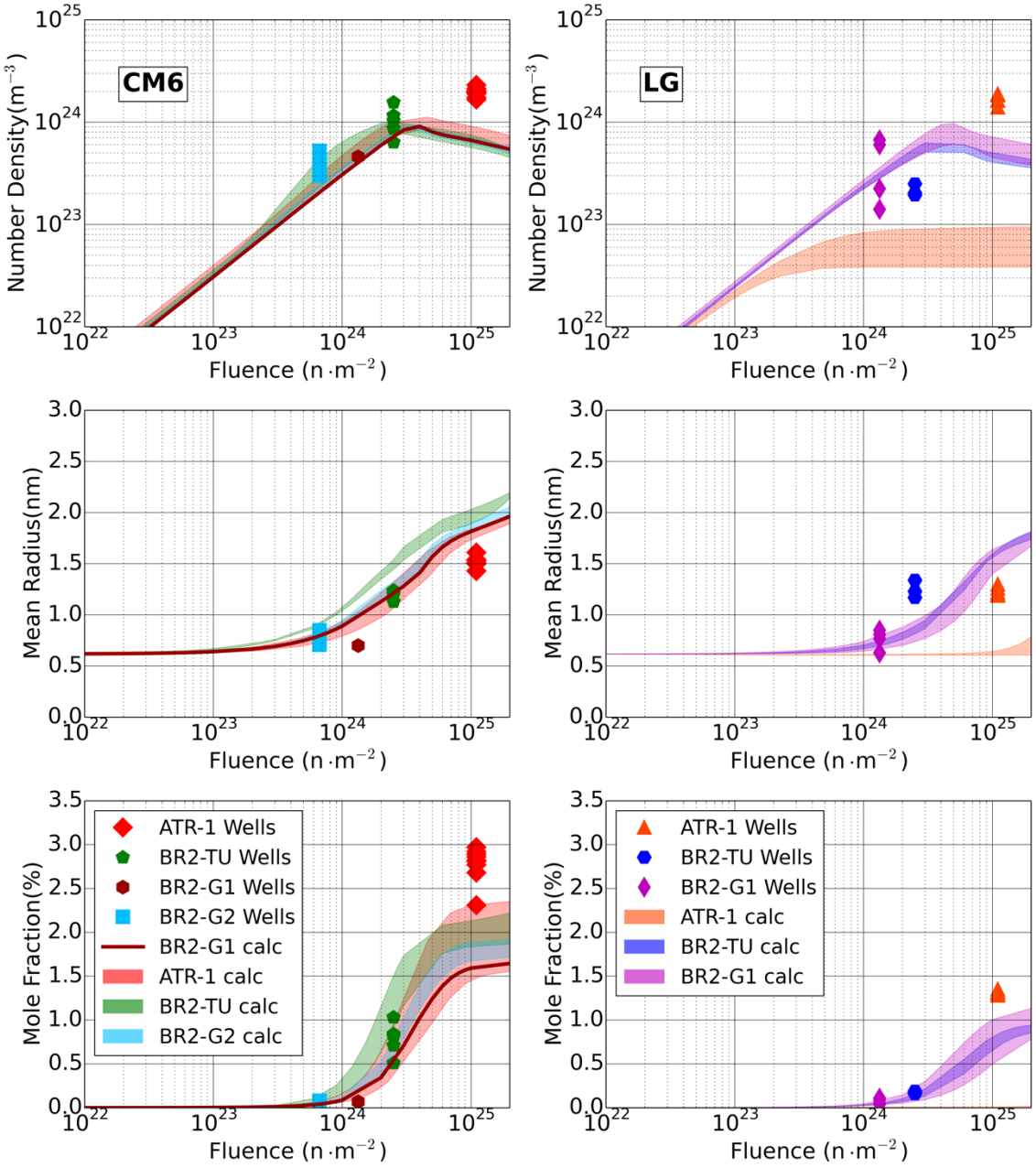


Figure 6-1 Evolution of precipitates in the high Ni CM6 and the medium Ni LG as a function of fluence compared to the APT data for the various irradiation conditions. The lines represent simulated data for single APT tip composition, while for multiple APT tips and associated compositions are shown as the shaded bands.

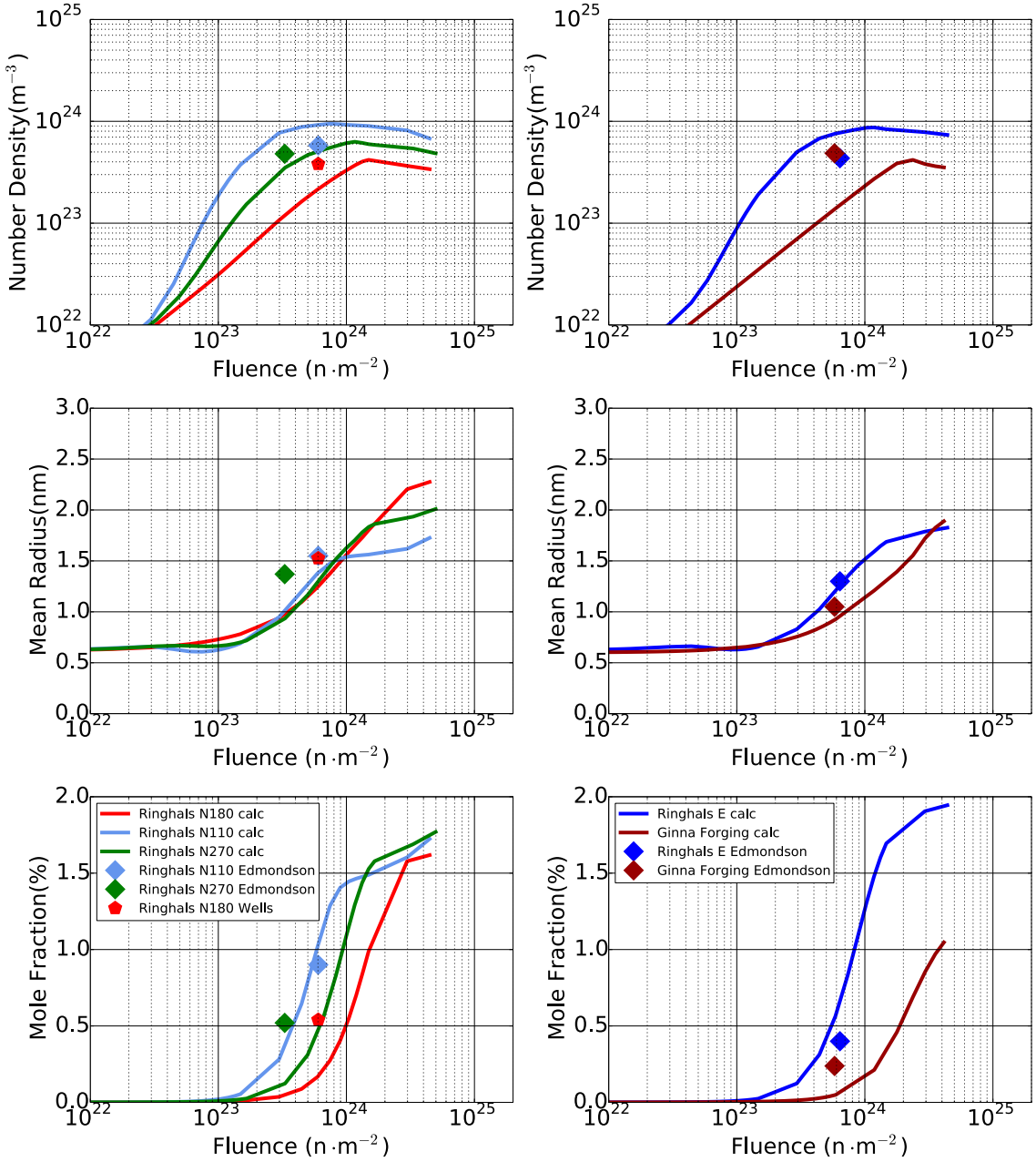


Figure 6-2 Evolution of precipitates as a function of fluence compared to the APT data for the various irradiation conditions for Ringhals and Ginna power reactors.

The corresponding evolutions of MNSPs for the average APT tip compositions are shown in Figure 6-3. The CD model predicts all the alloys are in the nucleation and growth (N&G) stages of precipitation except in the case of the high Ni ATR-1 CM6 (HHH) condition, where the early precipitation and very high fluence of $1.1\times10^{25}$m$^{-2}$ extends into the coarsening regime. Note in the

N&G regime the model-experiment comparisons are very sensitive to the accuracy of the simplified RED treatment of $D^*$, as discussed in Sec. 2.4.3.

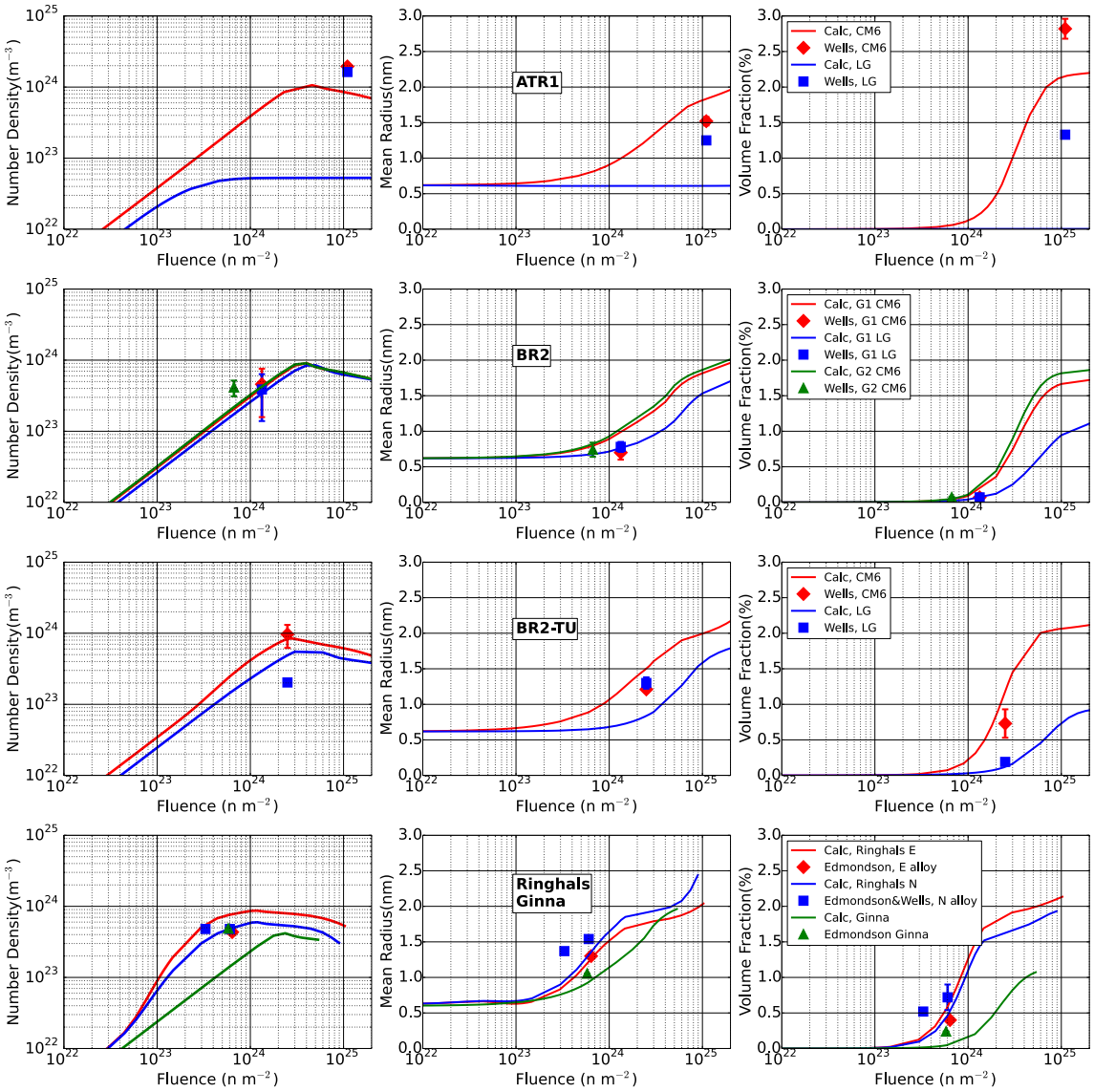


Figure 6-3 Modeling results of evolution of precipitates with average APT tip compositions as a function of fluence compared with experimental data (Some experimental data without error bars means there was only one tip measured at that condition)

Figure 6-4 shows the strong effect of higher flux on delaying precipitation by comparing CD model calculation results for nearly identical alloys (Ringhals N and CM6), both with high ≈ 1.6 at. % Ni, irradiated at widely different fluxes ($1.49\times10^{15}$m$^{-2}$s$^{-1}$ for Ringhals and up to $2.3\times10^{18}$ m$^{-}$

$^{2}s^{-1}$ for ATR-1). The BR2-TU flux ($3\times10^{17}$ $m^{-2}s^{-1}$) was chosen as the reference condition for the corresponding CM6 data (filled squares). Thus the higher flux CM6 data (unfilled circles and diamonds) for the ATR-1, G1, G2 conditions, shown in Table 3-1 and Table 3-2, are also plotted as filled symbols that have been adjusted, as indicated by the arrows, to an effective fluence for the BR2-TU reference flux, using the simple $p = 0.2$ scaling model in Eq. (2-32). The solid line shows the CD predictions for the Ringhals N average composition and the nominal low flux irradiation condition at $1.49\times10^{15}m^{-2}s^{-1}$ and 284°C. The shaded band shows the corresponding CD results for the CM6 average composition at the BR2-TU reference flux for irradiations at 300 and 320°C, covering the range of experimental temperatures.

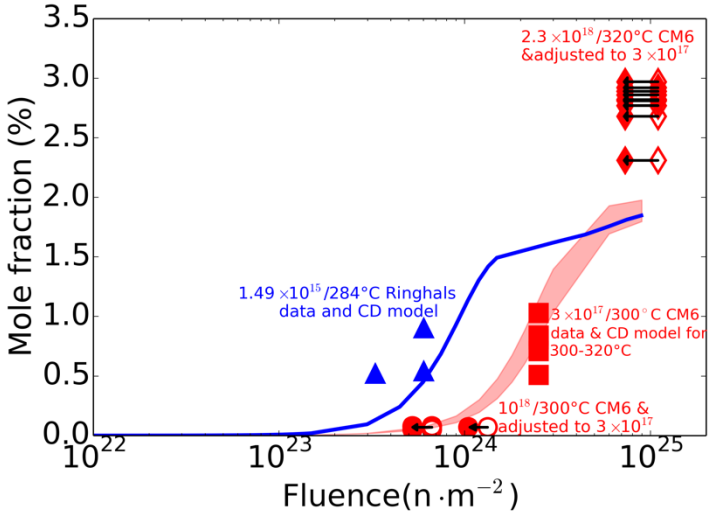


Figure 6-4 A comparison of the nearly identical Ringhals N alloy irradiated at low flux (blue triangles) and the CM6 alloy irradiated at high flux (filled and unfilled red circles, squares and diamonds). The open symbols are plotted at the actual fluence, while the filled circles and diamonds are plotted at an effective fluence corresponding to the BR2-TU flux, chosen as the CM6 reference condition. The BR2-TU square symbols are for the reference flux, hence are not adjusted. The blue solid line shows the CD prediction for the Ringhals N average composition and low flux irradiation condition, while the red band shows the CD predictions for the CM6 average composition at the BR2-TU reference flux for the actual irradiation temperatures ranging from 300 to 320°C.

Notably, the experimentally observed effect of flux is somewhat larger than calculated by the CD model, which can be seen from the fact that the difference in fluence for an approximately fixed precipitate volume fraction is larger in the experiments than the CD model. It is useful to be reminded that, as discussed in Sec. 2.4.3, the fluence scale of the two curves is largely governed by $D^*$ and that besides being oversimplified, the use of the canonical average $p = 0.2$ increases the approximate nature of the $D^*$ model. For example, it is known that the higher Ni contents in CM6 and Ringhals lead to a higher rate of solute vacancy trap recombination, which in turn corresponds to a larger effective $p$ [102]. Given the approximate estimates of $D^{th}$ and the additional complexity of RED treated by a simple model, there is no reason to expect that the $D^*$ would be accurate within the very precise constraints that would be needed for perfect agreement of the CD model with the data. However, if we allow $D^*$ to vary so as to fit the experimental mole fraction data points exactly, the resulting values fall within a factor of two of the standard fixed CD values for all alloys except Ginna (where the difference is only a factor of three), as can be seen from Figure 6-5. More generally the agreement between the CD model predictions and experiment would be enhanced if $D^*$ itself were treated as a fitting parameter for individual alloys. Figure 6-4 also shows that the precipitation plateau for CM6 predicted by CD at very high fluence is only ≈ 2/3 of experimental data, reflecting the approximate nature of the thermodynamic model.

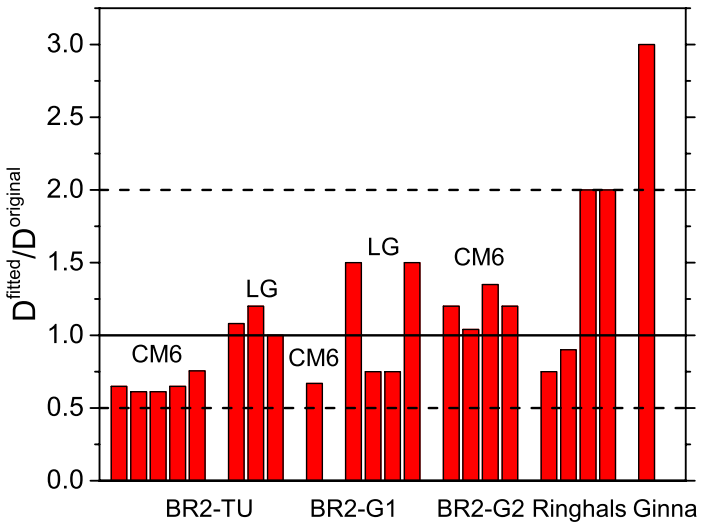


Figure 6-5 Ratio between fitted and original diffusion coefficients when matching CD calculated mole fraction of precipitates to experimental results.

Figure 6-6 provides a more detailed one-on-one comparison of the predicted cluster dynamics precipitate $\bar{r}$, $N$ and $f$ with APT measurements. If we exclude the ATR-1 experiments, the agreement is reasonable across this large range of compositions and irradiation conditions. However, the mole fractions of the MNSPs during the growth stage for the medium Ni alloys (BR2-TU MMH LG, BR2-G1 MHH LG and MLM Ginna) are all under-predicted by the model. These differences are most likely caused either by uncertainties in the thermodynamic parameterization and RED model or un-modeled physics, where the latter may include dislocation. The predicted and measured values for LG (LHH) and CM6 (HHH) under the ATR-1 irradiation conditions (using the recently updated temperature of 320°C) are shown as the open symbols. These results were not included in the parameter fitting, since the very high flux, fluence and high temperature irradiation condition is well beyond the corresponding range for LWR service and more relevant test reactor data. However, it's still useful to show the comparisons between the CD model predictions and the experimental data for this extreme condition. MNSPs are significantly under-predicted by the CD model in this case, particularly for LG. Actually, the experimentally

observed mole fractions of MNSPs for these alloys are even higher than what were predicted by CALPHAD model at equilibrium without considering the Gibbs-Thomson effect (see Sec. 4.4). Therefore, un-modeled physics might be playing a significant role, including that which is due to the very high flux used in the ATR-1 experiment. For example, this could be related to the influence of small amounts of Cu, or segregation at small, surviving, ex-cascade dislocation loops. In general, dislocation assisted nucleation is expected, especially for cases like LG with lower Ni concentration and free energy differences driving precipitation [34]. Note after the MNSPs have grown, their small loops nucleation sites would be consumed, or not apparent, making their role difficult to identify.

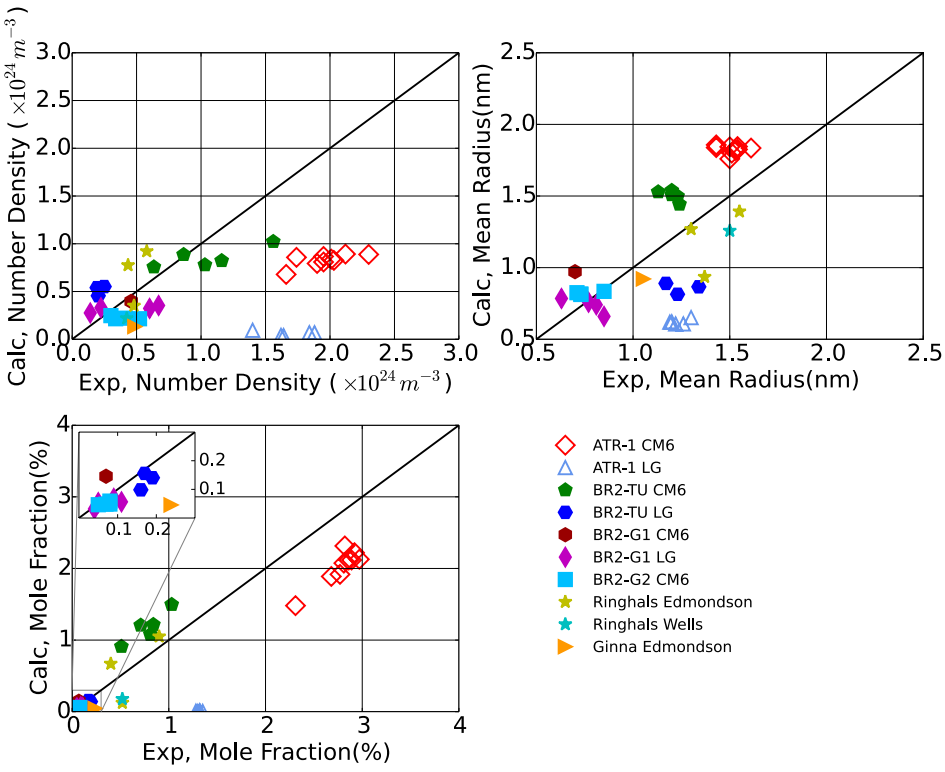


Figure 6-6 Comparison of the CD number density, mean radius and mole fraction and the APT data.

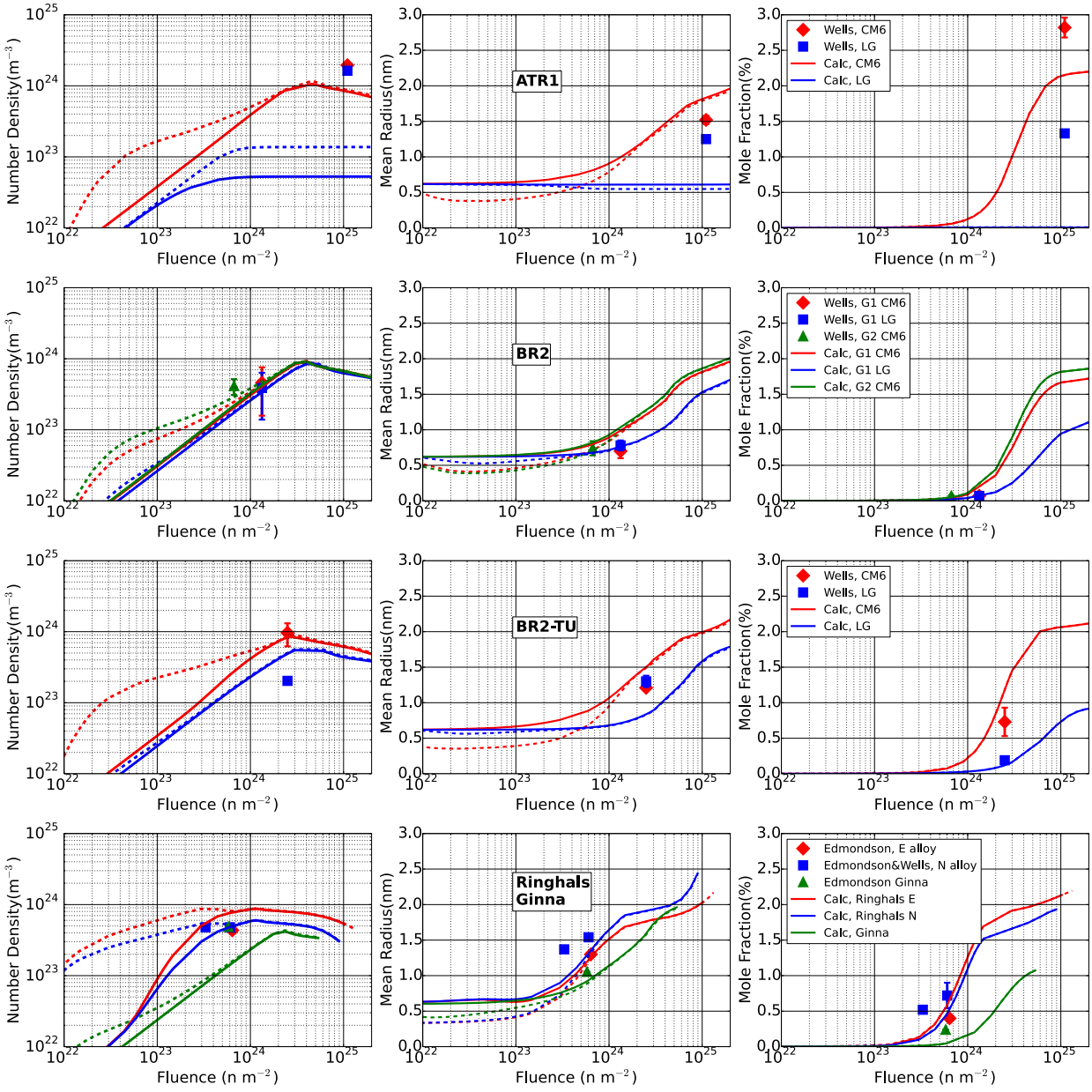


Figure 6-7 Comparison of simulation results with different cutoff size. Solid lines are calculation results with APT experimental cutoff size of 32 (BR2-TU LG, BR2-G1, BR2-G2), 43 (Ringhals and Ginna), and 65 (ATR-1, BR2-TU CM6) atoms and dashed lines are calculation results with cutoff size 10 atoms.

To show the effect of the cutoff size of CD output, all results are also calculated with a cutoff size of 10 atoms. The comparisons of results with different cutoff sizes are shown in Figure 6-7. As can be seen from the figure, there is almost no effect on the mole fraction of precipitates from

the small clusters below 65 atoms, so they are expected to have little impact on the mechanical properties of the alloy. The dip of mean radius with cutoff size 10 atoms in some alloys near irradiation fluence of $10^{22}m^{-2}$ is due to the early formation of heterogeneous nucleated clusters (~0.6nm) and later formation of smaller homogenous nucleated clusters.

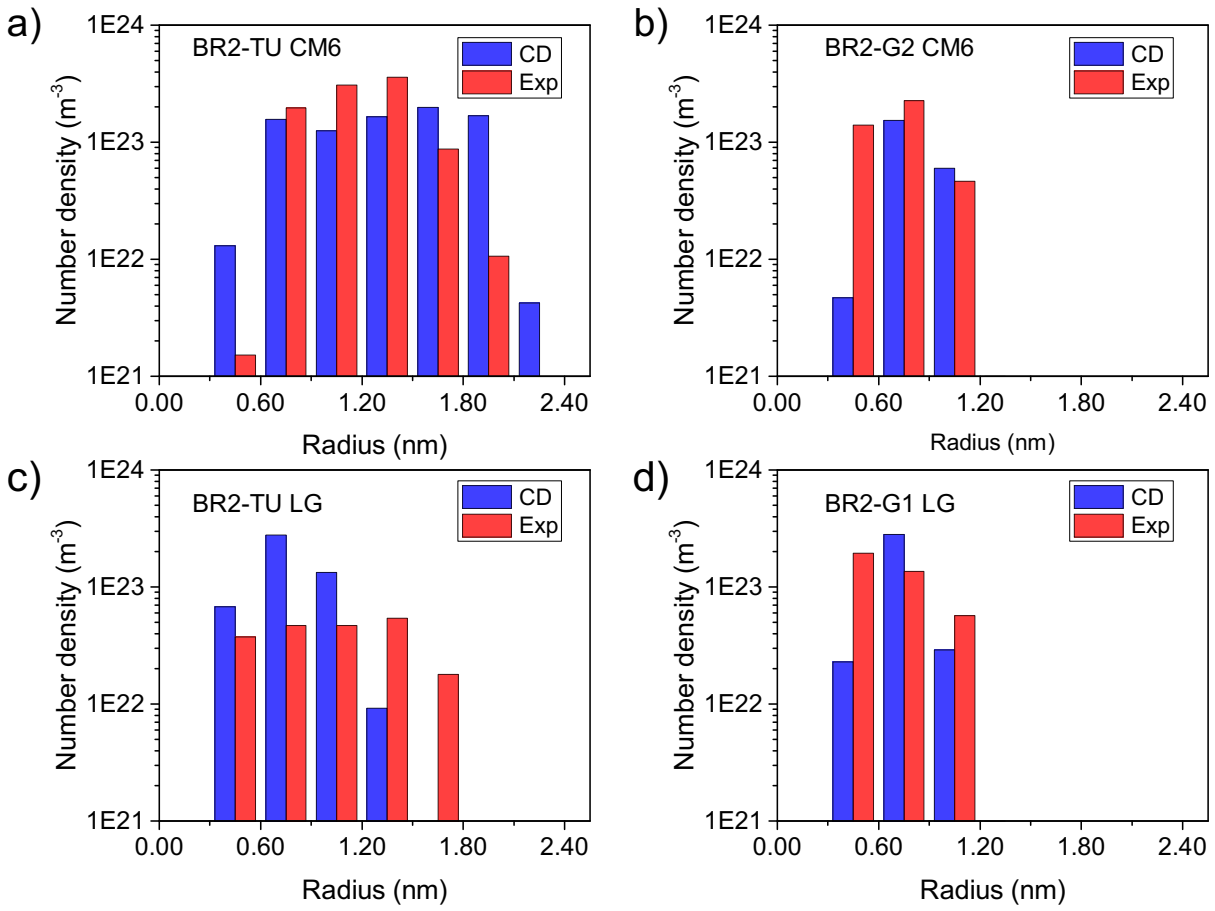


Figure 6-8 Comparison of precipitates size distribution between cluster dynamics model and experimental data.

Comparisons of the precipitate size distributions between CD model and the experimental data for selective alloys are shown in Figure 6-8. The size distributions from experiments shown here are summation results of all APT tips measured. The size distributions from CD model shown here are calculated with average APT tip compositions. The reason that size distribution of all of the alloys are not shown here is because there's very limited number of precipitates (either low

number density or only 1 tip) observed in other alloys that it's hard for the APT data to provide any meaningful size distribution. No quantitative comparisons were made between CD results and APT data for particle size distribution, but it can be seen from Figure 6-8 that qualitatively CD model gives similar shape of particle size distribution in the same radius and number density regime compared to APT results.

Overall, except for the confounded ATR-1 data, the CD model results are in semi-quantitative agreement with experimental APT measurements of MNSP $N$, $\bar{r}$ and $f$, as well as the observed MNSP size distribution. Given the complexity of multicomponent precipitation under irradiation and the wide range of compositions and irradiation conditions considered, this level of agreement suggests that the model reasonably represents the dominant underlying physics of MNSPs evolution under irradiation. Most importantly, the model can be used to better understand the role of different mechanisms, and assess the influence of key material and irradiation variables for low Cu steels under both test reactor and vessel service LWR irradiation conditions.

In summary, the success of the present model suggests that vacancy enhanced diffusion is consistent with observed MNSP growth kinetics. However, other factors may also play a role, and in fact appear to be critical in the nucleation stage, where radiation induced effects associated with cascades mediate nucleation rates for medium Ni steels associated with relatively lower driving forces for homogeneous nucleation, which will be further discussed in following Sec. 6.6.

## 6.6 Heterogeneous nucleation effect

As an example of possible mechanistic insight, Figure 6-9 shows the ratio of number density of MNSPs formed by heterogeneous nucleation to homogeneous nucleation at fluences of 1, 5 and $10 \times 10^{23}$ n·m$^{-2}$. In all cases heterogeneous nucleation is dominant at lower fluence and in 6 out of 8 cases it is dominant even at high fluence. Plots of MNSP number densities for different phases

formed by different nucleation mechanisms as a function of fluence are shown in Figure 6-10 for two of the alloys as illustration. In Ringhals E alloy, which contains high Ni composition, the number density of precipitates formed by homogeneous and heterogeneous nucleation mechanisms are comparable, while in BR-TU LG alloy as well as other similar alloys, which contains medium Ni composition, the number density of precipitates formed via heterogeneous nucleation mechanism totally dominates.

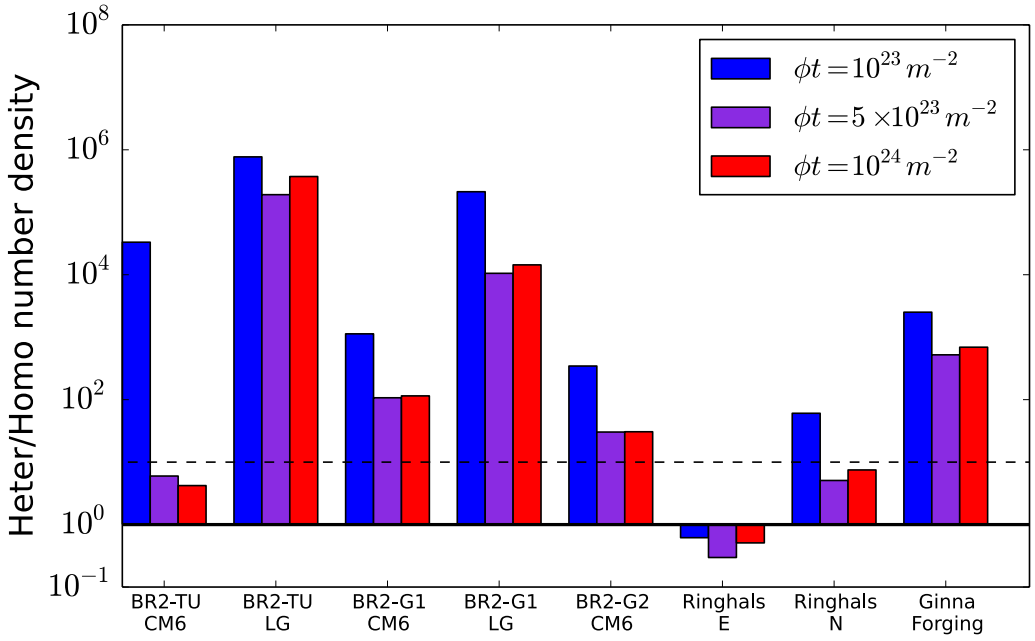


Figure 6-9 The ratio of number of precipitates created by heterogeneous to homogeneous nucleation at different fluences.

In summary, heterogeneous nucleation on cascade is a very important mechanism on the formation of MNSPs in RPV steels. Our results suggest that such radiation-induced processes play a dominant role in MNSP formation in low and medium Ni alloys. Furthermore, the discrepancies in the model predictions for medium Ni steels suggests that the simple model for heterogeneous nucleation used in this work may need refinement, e.g., to take into account more explicitly the

role of small interstitial loops formed in cascades and segregation to these loops, as discussed in Ref. [49], as well as to pre-existing network dislocations.

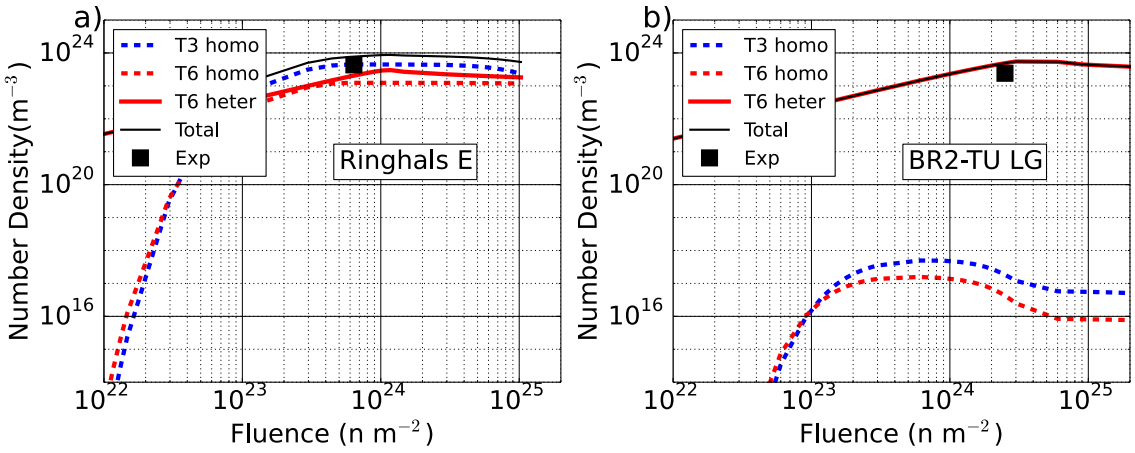


Figure 6-10 Number density of precipitates of different phases via different nucleation mechanism in the alloys of a) Combined effect of homogeneous and heterogeneous nucleation mechanism b) Heterogeneous nucleation mechanism dominated

## 6.7 Composition effect

Atom probe tomography (APT) is a powerful tool for three-dimensional nano-analytical mapping with near atomic-scale resolution [129]. However, the volume of the analyzed region is typically ≈ 1 to $4\times10^4$ nm$^3$, corresponding to ≈ 5 to $40\times10^6$ atoms and 100-200 nm in length. Such tiny volumes are subject to significant tip-to-tip composition fluctuations in typical micro-segregated steels. For example, if a particular tip contains, or is adjacent to, a large carbide, it is likely to contain significantly less than the average Mn content, which is always lower than the nominal bulk content in any event. Both Si and Ni are controlled by the specific alloy solute additions, but these also vary somewhat from tip to tip. Thus as has been shown [24] the precipitation in a tip is strongly affected by the local solute concentration. Indeed tip-to-tip chemistry variations can be exploited to establish dissolved solute-precipitate relationships [24]. In this work we used the actual measured APT Mn, Ni and Si compositions measured by APT in modeling MNSPs evolutions.

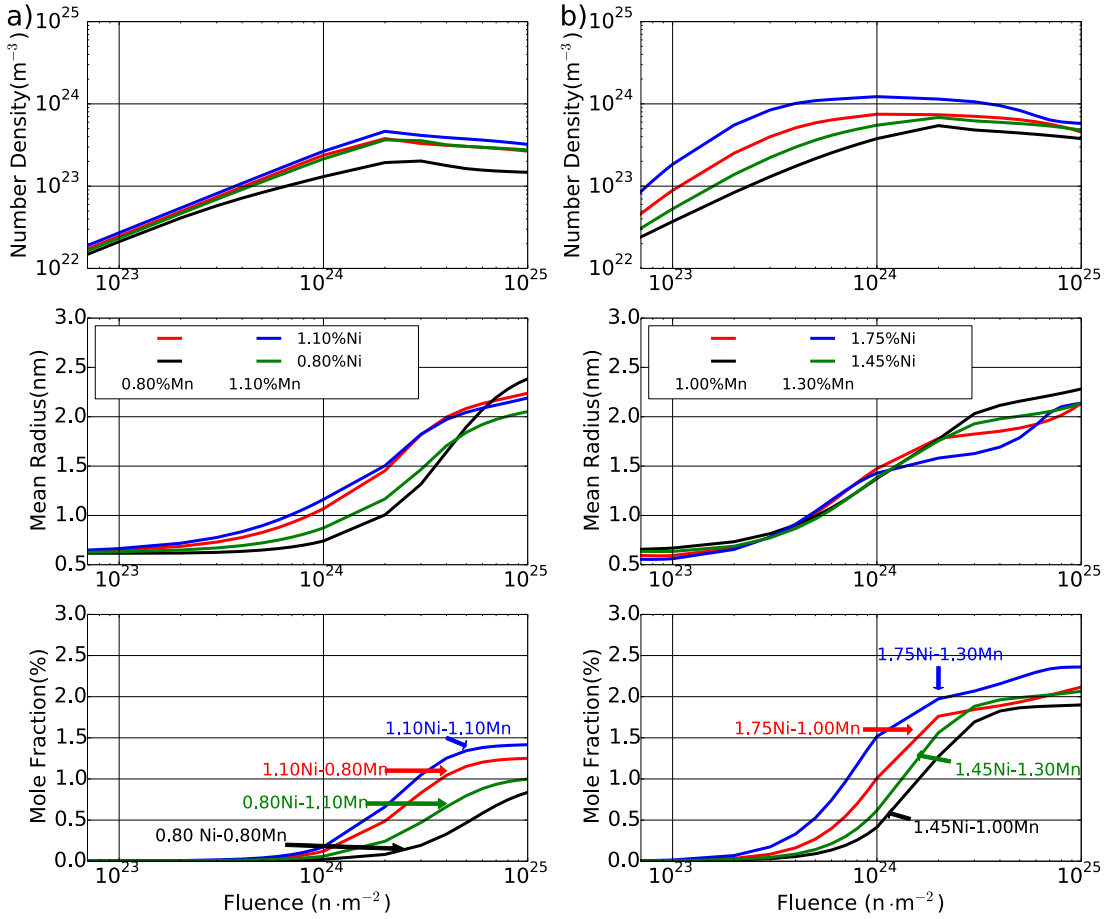


Figure 6-11 The effects of Mn and Ni on the evolution of precipitates at $1\times10^{16}$m$^{-2}$s$^{-1}$ at 290°C for: a) 0.35at.% Si and b) 0.45at.% Si.

Figure 6-11 highlights the compositional sensitivity for irradiations at a flux of $10^{16}$ n·m$^{-2}$s$^{-1}$ at 290°C. Figure 6-11 a) shows the effects of intermediate Ni (0.80, 1.10at%) and lower Mn contents (0.80, 1.10at%), while Figure 6-11 b) is for high Ni (1.45, 1.75at.%) and slightly higher Mn (1.00, 1.30at.%). These values are in the range of the in-service type RPV alloys studied here. As expected, the MNSP $N$ and $f$ systematically increase with Mn and Ni. The corresponding $\bar{r}$ values are somewhat less sensitive to composition variations, especially at higher Ni. Composition also systematically affects both the pre- and post-saturation regimes of MNSP $N$ and $f$. Clearly, higher Ni has a powerful effect on lowering the fluence associated with the rapid MNSP formation

with high *N* and *f*. Further, in both cases, there are only slightly overlapping regions of nucleation and growth, since *N* is nearly saturated (or decreasing slightly) when *f* begins to rapidly increase. This observation rationalizes some of the confusion regarding the character of MNSPs. That is, a high number density of sub nm MNSPs form before they begin to grow rapidly, and are not easily identified as well-formed precipitates. Note the dominant nucleation mechanism also varies between the medium (heterogeneous) and high Ni (homogeneous) regimes.

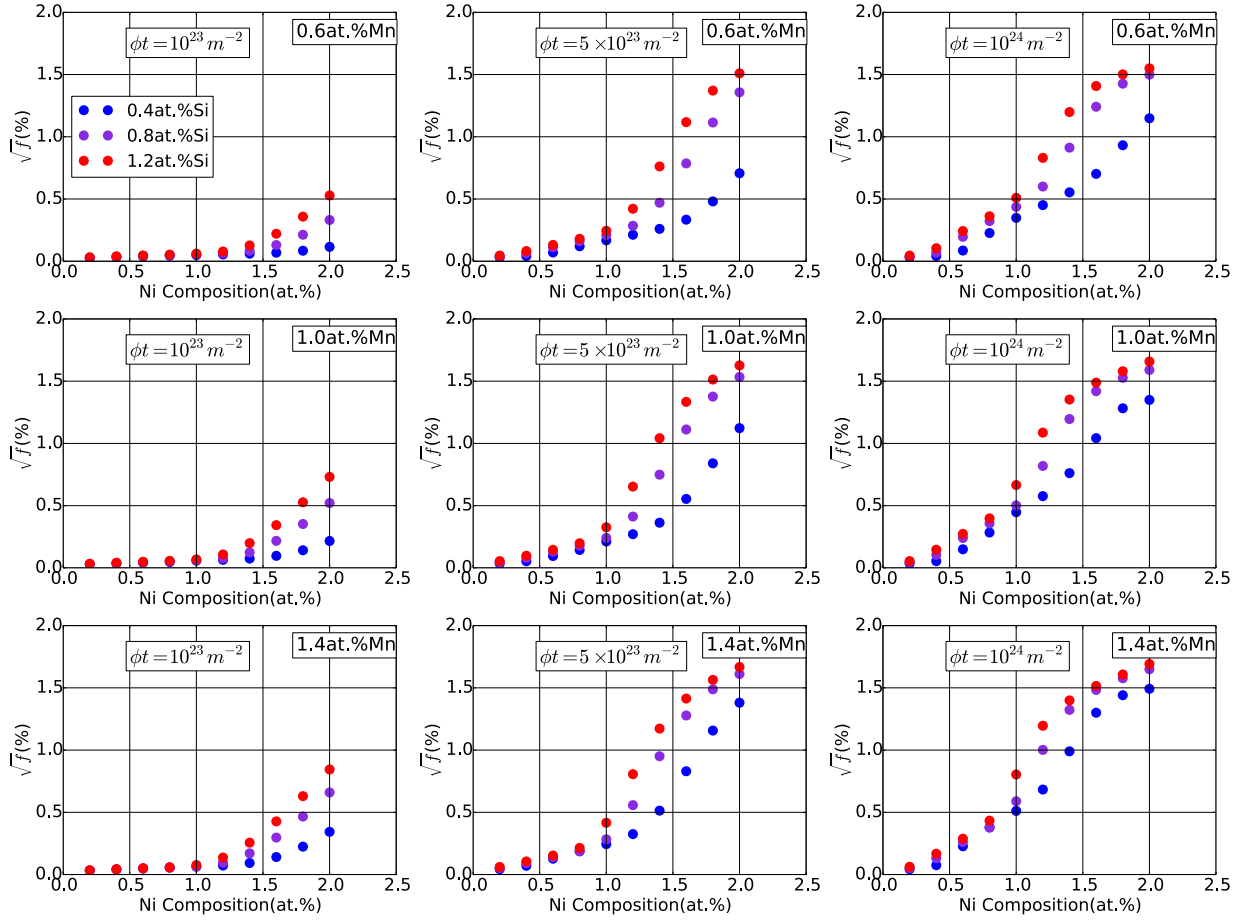


Figure 6-12 The square root of mole fraction ($\sqrt{f}$) as a function of Ni composition for various Mn and Si contents at different fluences.

Figure 6-12 shows cross plots of the $\sqrt{f}$ versus Ni, over the specified range of Mn and Si at $10^{23}$, $5\text{x}10^{23}$ and $10^{24}$ n·m$^{-2}$ at 290°C and a flux of $3\text{x}10^{15}$n·m$^{-2}$s$^{-1}$. As discussed below, the $\sqrt{f}$ is used since it's the primary MNSP characteristic that controls $\Delta\sigma_y$ and $\Delta T$. Clearly Ni has a

dominant effect on $\sqrt{f}$. The effects of Mn and Si are significant but more modest than they are for Ni. The absolute MNSP $\sqrt{f}$ is low at $10^{23}$ n·m$^{-2}$, but increases somewhat starting at ≈ 1.5at.%Ni. The effect of Ni is much stronger at $5x10^{23}$ n·m$^{-2}$ above ≈ 0.5at.%Ni, and $\sqrt{f}$ again increases rapidly above ≈ 1.5at.%Ni. At $10^{24}$ n·m$^{-2}$ $\sqrt{f}$ increases approximately linearly, or with a weak polynomial dependence, between 0.5at.% and 1.6at.%Ni, and at higher Ni the increase in $\sqrt{f}$ begins to taper off.

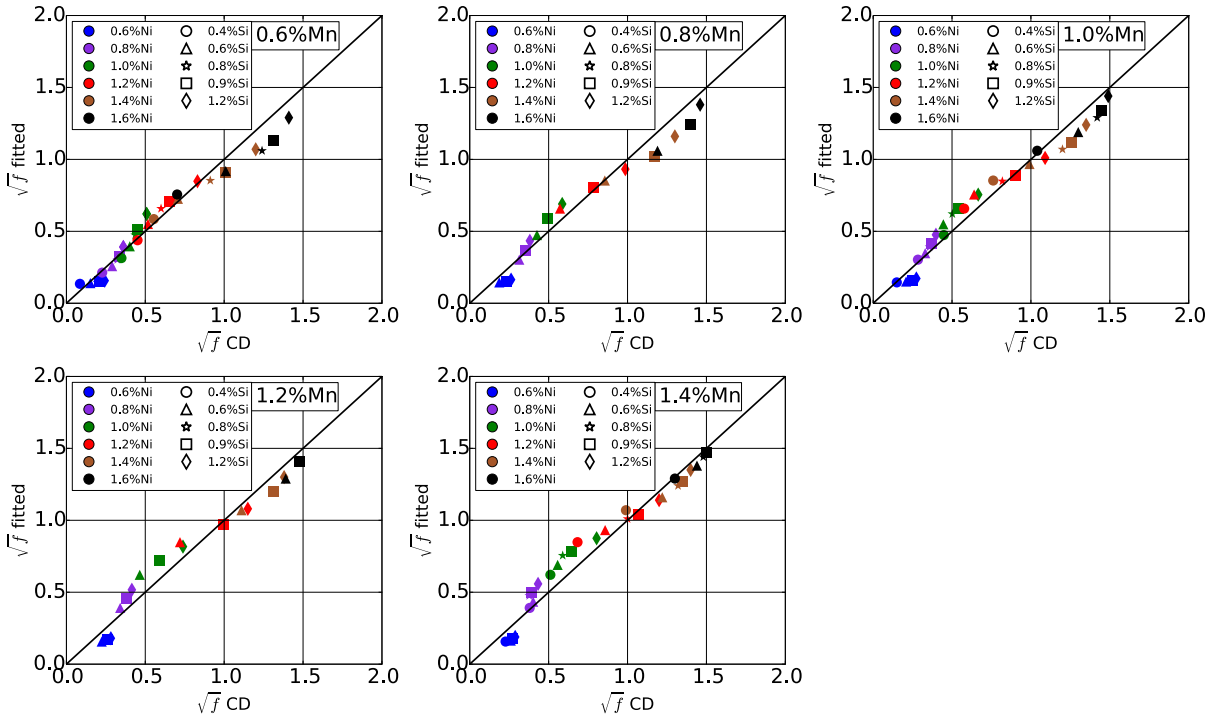


Figure 6-13Comparison between fitted and results from CD for different alloy compositions

For practical purposes the relevant ranges of bulk RPV steel compositions are ≈ 0.6-1.6at.%Ni, ≈ 0.4-1.2at.%Si and 0.6-2.0at.%Mn. However, the dissolved Mn is lower since this solute is also contained in carbides; further, most steels have less ≤ 1.6at.%Mn. Thus a practical range of dissolved Mn is ≈ 0.6-1.4at.%. Further, 1.0at.%Ni is the limit in the US surveillance database for low Cu steels. Here we focus on the peak extended life fluence of $10^{24}$ n·m$^{-2}$. Within

this composition range, which is consistent with the formation of T3 (G) and T6 ($\Gamma_2$) phases, the $\sqrt{f}$ can be fit by a polynomial in the form

$$\sqrt{f} = C_0 + C_1 Ni + C_2 Ni^2 \qquad (6\text{-}16)$$

Here the *C*s are functions of (Mn + Si) where

$C_0 = 0.7249\text{-}0.6392(Mn+Si)\text{-}0.0435(Mn+Si)^2$

$C_1 = \text{-}1.2058+0.9765(Mn+Si)+0.2108(Mn+Si)^2$

$C_2 = 0.3360+0.1641(Mn+Si)\text{-}0.2090(Mn+Si)^2$

Figure 6-13 compares the CD $\sqrt{f}$ to that predicted by Eq. (6-16). The agreement is excellent.

This systematic behavior can be traced to fact that CD model predicts the formation of stoichiometric G and $\Gamma_2$ phases. The $\Gamma_2$ phase has almost 1 (Mn + Si) atom for every Ni atom. The G phase has ≈ 0.81(Mn + Si) atom for every Ni atom. Thus while the overall effects of Mn and Si on the MNSP nucleation and growth at a specified temperature and fluence are more complex, to a first approximation they are associated with a varying balance of G and $\Gamma_2$ phases, that in both cases are reasonably represented by Eq. (6-16). Further, it has been experimentally observed that the effects of Mn and Si are individually relatively weak, due to the fact that their sum is typically approximately constant and roughly equal to the Ni in the MNSP. That is, if Si is low the MNSP is more enriched in Mn and vice versa. Note that non-stoichiometric phase-field effects are not captured in the current CD model, although the composition range of the phase-fields of both G and $\Gamma_2$ are quite small.

However, there is no simple relation between *f* and Ni for all combinations of composition. For example, low values of Mn or Si may be insufficient to form the *f* of G and $\Gamma_2$ phases that would otherwise be associated with very high Ni. Likewise, excess quantities of Mn and Si would remain

in solution once the amounts of these solutes needed to form the modeled phases exceeded that required for a given Ni content.

6.8 Temperature effect

MNSPs evolution is also very sensitive to the irradiation temperature, which is significant for a number of reasons. First the temperatures in this study varied over a nominal range of ≈ 290 to 300°C, and in practice up to ≈ 320°C in the actual as-run condition for ATR-1. Typical in service power reactor vessel temperatures range from ≈ 270°C to 300°C. Further, it is extremely difficult to accurately control and measure temperatures to uncertainties less than ≈ ±10-15°C. Notably, the effects of temperature are also very sensitive to the alloy composition.

Figure 6-14 shows the effect of temperature on the evolution of MNSPs, modeled for two compositions: a high solute 1.45at.%Mn-1.65%Ni-0.45%Si and a low solute 1.00at.%Mn-0.70%Ni-0.35%Si composition, respectively. The results are shown for a flux $10^{16}$n·m$^{-2}$s$^{-1}$ up to $10^{25}$n·m$^{-2}$ at 280, 290 and 300°C. The effect of these variations of temperature mainly occurs during the nucleation and growth stage of precipitation associated with the rapid increase in $N$, which can differ up to five times for high solute alloy and up to 10 times for low solute alloy for only a 20°C temperature difference. The effect of temperature on $N$ is also reflected on mole fraction of MNSPs that can differ up to 1.0% for high solute alloys and 0.5% for low solute alloys. There is only a minor corresponding effect on the mean MNSP radius, $\bar{r}$. These results demonstrate that temperature effects must be carefully considered when comparing experimental with the CD model predictions.

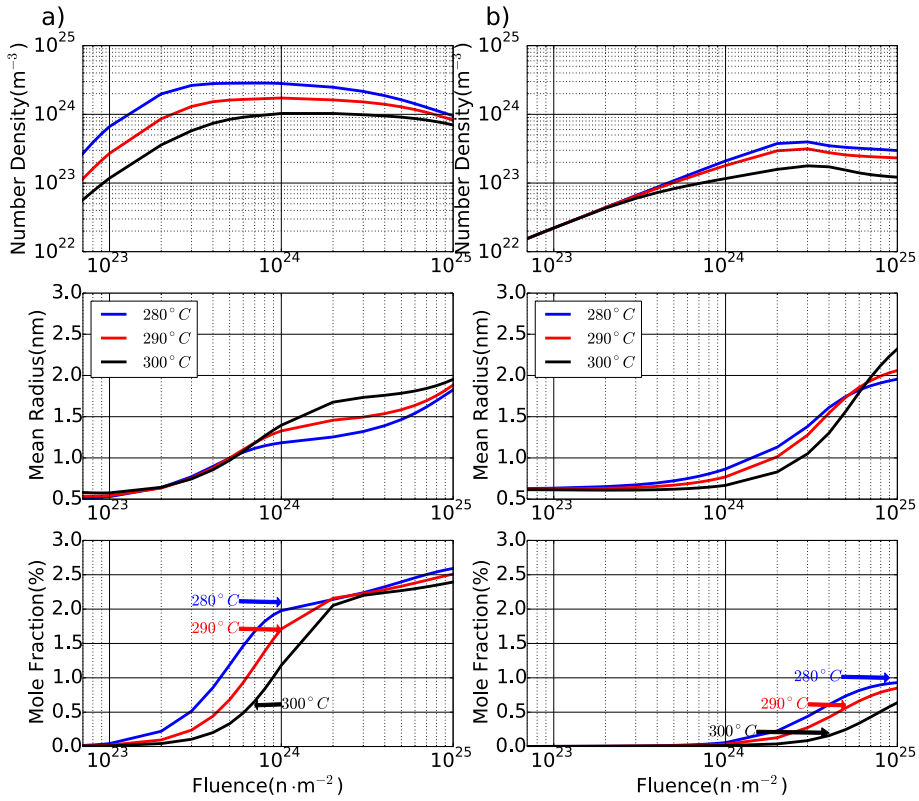


Figure 6-14 The effect of temperature on the evolution of MNSPs for: a) Fe-1.45at.%Mn-1.65%Ni-0.45%Si; and, b) Fe-1.00at.%Mn-0.70%Ni-0.35%Si.

Similar to what discussed in last section for effect of composition on $f$ of MNSPs, the MNSP $f$ also depends strongly on the irradiation temperature ($T$). Figure 6-15 plots $\sqrt{f}$ versus $T$ at Ni = 0.6at.%, 1.0at.%, 1.4at.% for 0.6at.%Si and 1.0at.%Mn at fluences of $5x10^{23}$ and $10x10^{23}$ $n \cdot m^{-2}$. Figure 6-15 a) shows that the absolute $\sqrt{f}$ increases with increasing Ni and decreasing $T$. Figure 6-15 b) shows the same data normalized to 1 at 290°C. In all cases the $\sqrt{f}$ versus $T$ follows an approximately linear relation, and overall the trends are qualitatively similar.

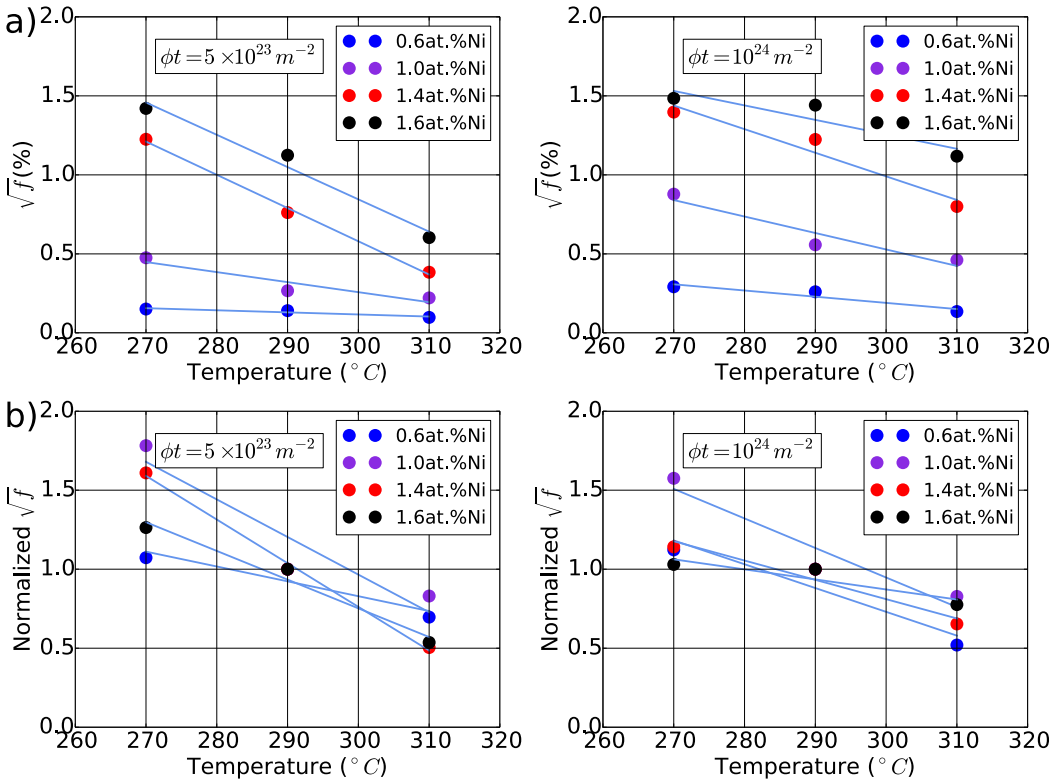


Figure 6-15 The effect of temperature on $\sqrt{f}$ for various alloy Ni contnets with 1.4at.%Mn-0.6%Si and two fluences: a) absolute √f; and, b) normalized to 1 at 290°C.

## 6.9 Ductile to brittle transition temperature shift ($\Delta T$) based on the CD-based precipitation model predictions

As mentioned in Sec. 1.1, the reason we need to study the evolution of MNSPs in RPV steels is because they are one of the main reasons that may cause hardening of RPV steels at high irradiation fluence and as a result increase the ductile to brittle transition temperature of RPV steels. Here and after the increase of the ductile to brittle transition temperature will be denoted as $\Delta T$. Therefore, it will be interesting to see how much these MNSPs can affect the $\Delta T$ in real reactor conditions based on the CD model we developed. Please note we do not claim that these examples represent actual quantitative predictions of anticipated embrittlement behavior, but they can give us the bulk range of $\Delta T$ in 80 years and beyond in real reactors. Here in this section, we first will briefly describe in Sec.6.9.1 the hardening model we used to translate the volume fraction ($f_V$),

number density ($N$) and mean radius ($r$) of precipitates to yield stress increases ($\Delta\sigma_y$) and to the associated $\Delta T$. This model was developed by our collaborator Prof. Odette and his group [17,24,100,101] at University of California - Santa Barbara. Then the results will be shown in Sec.6.9.2.

6.9.1 Hardening model

The model for precipitate hardening used here is based on Russell-Brown model [57]

$$\tau = 0.8\frac{Gb}{L}\left[1-\frac{{E_1}^2}{{E_2}^2}\right]^{1/2} \quad for \quad \sin^{-1}\frac{E_1}{E_2} < 50°$$
$$\tau = \frac{Gb}{L}\left[1-\frac{{E_1}^2}{{E_2}^2}\right]^{3/4} \quad for \quad \sin^{-1}\frac{E_1}{E_2} > 50° \qquad (6\text{-}17)$$

where $G$ (83GPa) is the shear modulus, $b$ (0.248nm) is the Burgers vector, and $L$ is the average spacing of a random distribution of pinning points on a slip plane.

Here $\frac{E_1}{E_2}$ is calculated by

$$\frac{E_1}{E_2} = \frac{E_1^{\infty} log\frac{r}{r_0}}{E_2^{\infty} log\frac{R}{r_0}} + \frac{log\frac{R}{r}}{log\frac{R}{r_0}} \qquad (6\text{-}18)$$

where $E_1^{\infty}/E_2^{\infty}$ (0.5064), $r_0$ (0.492nm) and $R$ (625nm) are obtained by fitting to experimental data measured by UCSB, $r$ is the radius of precipitates.

$L$ is calculated by

$$L = 1.77\frac{r}{\sqrt{f_v}} \qquad (6\text{-}19)$$

where $f_V$ is the volume fraction of precipitates.

The yield stress caused by precipitates $\sigma_p$ is then calculated by

$$\sigma_p = M\tau \qquad (6\text{-}20)$$

where $M$ is the Taylor factor (3.06).

The precipitate hardening contribution must be combined with those from other features including any pre-existing obstacles, like $Mo_2C$, that contribute a strength increment $\sigma_u$, where $\sigma_u$

is the yield stress caused by any pre-existing obstacles before irradiation, here taken as 180MPa [17]. The carbide features are strong obstacles bypassed by dislocation bowing. Here $\Delta\sigma_y$ is approximated using a superposition model as

$$\Delta\sigma_y = (1-\mathrm{S})\sqrt{\sigma_p^2+\sigma_u^2} + \mathrm{S}(\sigma_p+\sigma_u) - \sigma_u \quad (6\text{-}21)$$

where S is calculated by [17,101]

$$S = \max\left(0,\ \alpha_0 - \alpha_m(5.0-3.3\alpha_0)\right) \quad (6\text{-}22)$$

Here $\alpha_0$=0.8 and $\alpha_m$ is calculated by

$$\alpha_m = \left[1-\frac{{E_1}^2}{{E_2}^2}\right]^{1/2} \quad (6\text{-}23)$$

More details regarding superposition model can be found in Chapter 2 of [101].

The $\Delta\sigma_y$ can be approximately related to transition temperature shifts by a constant factor $\Delta T = C\Delta\sigma_y$, where here $C$ was taken as 0.68°C/MPa. Again the actual relation is more complex but this value of $C$ is broadly consistent with both empirical fits to experimental data [130] and the underlying fracture theory [131].

6.9.2 Results

A series of alloy compositions are studied here to cover the typical range of RPV alloy compositions, and the grid of the compositions of each element is listed in Table 6-6. This gridding gives a total of 3×5×2=30 alloy compositions that are studied.

Table 6-6 Composition of alloys studied for $\Delta T$ in real reactor condition

| Element | Compositions (at.%) | | | | |
|---|---|---|---|---|---|
| | 1 | 2 | 3 | 4 | 5 |
| Mn | 0.60 | 1.00 | 1.40 | | |
| Ni | 0.60 | 0.80 | 1.00 | 1.30 | 1.60 |
| Si | 0.4 | 1.2 | | | |

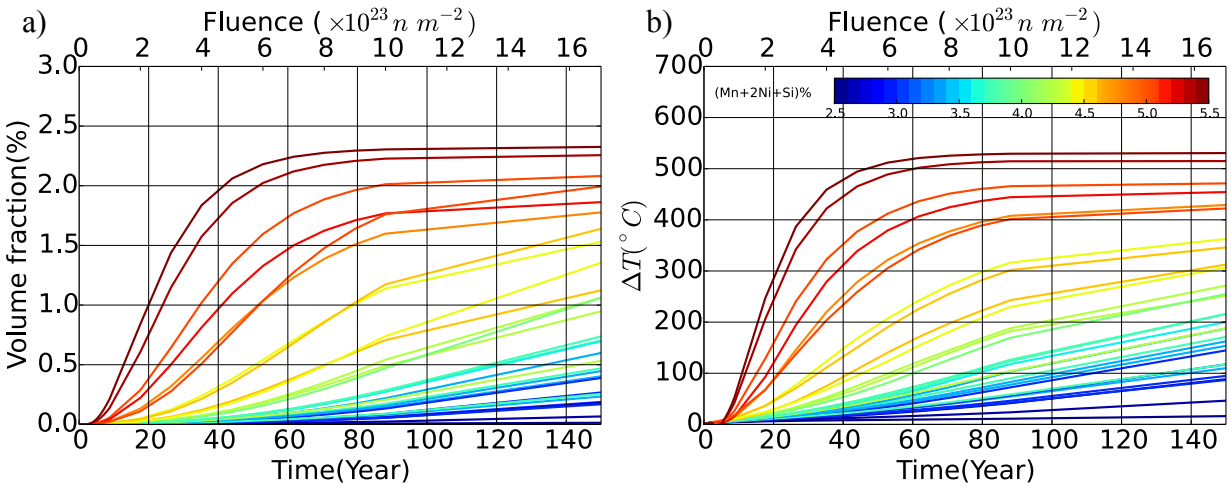


Figure 6-16 Effect of compositions on a) volume fraction and b) ductile-brittle-transition-temperature for typical RPV compositions

Figure 6-16 shows the predicted time and fluence dependence of $f_V$ and $\Delta T$, respectively, for compositions listed in Table 6-6 at 290°C and a flux of $3.6\times10^{14}$m$^{-2}$s$^{-1}$, pertinent to RPV service. Here in these two figures, the different color of each line represent different alloy composition, which is $C_{Mn} + 2C_{Ni} + C_{Si}$, where $C_i$ is the composition of each element in alloy. The reason that we plot this way is because it is found that the volume fraction of precipitates scales almost monotonically with $C_{Mn} + 2C_{Ni} + C_{Si}$, which can be seen from Figure 6-17. Figure 6-16 a) shows that for most of the alloys the MNSPs are still in the nucleation and rapid growth stage from 40 to 80 years. At an extended life fluence of $10^{24}$n·m$^{-2}$ typical RPV steels with 1.0at.%Ni are predicted to contain $f_V \approx$ 0.2% MNSP that is capable of producing $\Delta T \approx$80°C. High 1.6%Ni steels contain $f_V \approx$ 0.9% MNSP at $10^{24}$ n·m$^{-2}$, with corresponding $\Delta T$ of 250°C.

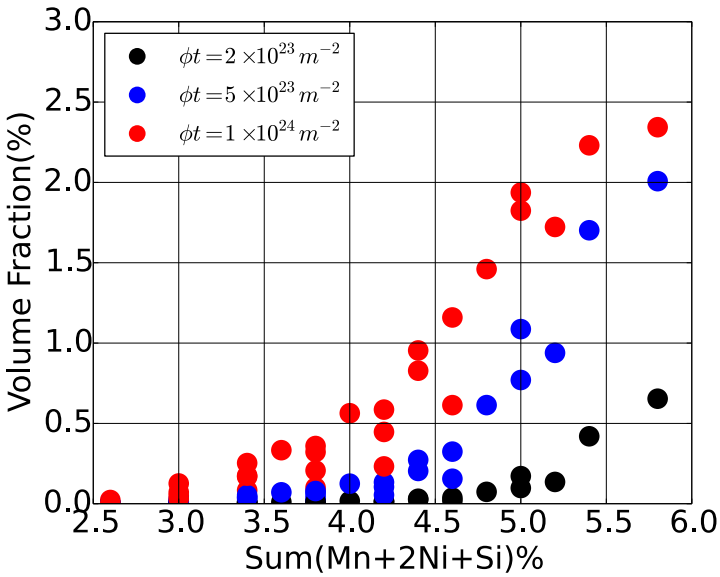


Figure 6-17 Volume fraction of MNSPs as a function of alloy composition Mn+2Ni+Si at different fluences for typical RPV steels

## 6.10 Summary

Based on the cluster dynamics simulation of the evolution of MNSPs under irradiation, the principle conclusions derived from this study include:

1. A thermodynamically-based CD model has been developed to treat MNSP evolution in irradiated low Cu steels that predicts the slow precipitation of G/T3 and $\Gamma_2$/T6 phases at around 290°C, that can reach high mole fractions at high fluence.
2. The CD model is generally in qualitative, or semi-quantitative agreement with experimental APT observations on the composition dependence of MNSP *N*, *r* and *f*.
3. A heterogeneous mechanism for nucleating MNSPs is critical to their formation in intermediate and low solute alloys, although not at the high Ni contents of >1.5at.%Ni, where homogeneous nucleation dominates. Heterogeneous nucleation is not needed at sufficiently high Ni due to a larger free energy difference driving precipitation.

4. The alloy Ni content is the dominant compositional factor in forming MNSPs, while Mn and Si play lesser roles. The dominant role of Ni is due to the fact the G and $\Gamma_2$ phases respectively contain 1 and 0.8 (Mn + Si) atoms for every Ni atom, respectively.
5. The absolute threshold for G and $\Gamma_2$ MNSPs formation appears to be ≈ 0.5at.%Ni.
6. The model suggests that MNSPs in low Cu alloys in RPVs are in a nucleation and growth stage in present reactors, with significant potential for more hardening and associated temperature shifts expected during life-extension.
7. As an illustrative example, at an extended life fluence of $10^{24}$n·m$^{-2}$ typical RPV steels with 1.0at.%Ni and 1.6at.%Ni are predicted to contain $f_V \approx 0.2\%$ and 0.9% MNSPs that are nominally capable of producing $\Delta T \approx 80°C$ and 250°C, respectively.
8. The mole fractions of MNSPs under very high flux at very high fluence (ATR-1) observed from experiments are even higher than the value predicted by CALPHAD model at equilibrium without considering Gibbs-Thomson effect. Thus even with cascade enhanced nucleation, the CD model under-predicted the mole fraction of MNSPs in this case. This suggests that unmodeled other physics, like influence of small amounts of Cu, or segregation resulting in precipitation on small dislocation loops, may play a significant role under this extreme condition where full precipitation is expected.
9. The MNSP mole fraction of medium Ni steels (BR2-TU, BR2-G1 LG and Ginna) are under predicted compared to experiments. The differences may again be due to either thermodynamic model inaccuracies, or un-modeled physics.

# Chapter 7 Modeling of Mn-Ni-Si precipitates under post-irradiation annealing

## 7.1 Chapter Abstract

The CD model has been further validated by comparing simulation results to experimental data under post irradiation annealing conditions. The model successfully predicts the dissolving of precipitates at the beginning of annealing and coarsening of large size (>2nm radius) of precipitates after annealing for a certain time. Good agreements have been obtained between CD results and APT data for number density and mean radius. The model tends to over-predict the mole fraction of precipitates after long annealing time. Yield stress of alloy annealed under different temperatures has also been compared between CD results and experimental data. Good agreements are obtained for higher annealing temperatures (425°C and 450°C) while CD predicts higher yield stress (less recovery) compared to experimental data for lower annealing temperature (350°C, 375°C and 400°C). The over-prediction of the yield stress at lower temperatures is believed due to the recovery of defects in alloys, which is not included in the model.

## 7.2 Introduction and Motivation

Post irradiation annealing (PIA) can provide significant insight into the nature of the MNSPs. If the annealing temperatures are wisely chosen, it can be a good way to confirm if these MNSPs are radiation enhanced or radiation induced. For the modeling benefits, post-irradiation annealing experimental results is a good source of data that can be used to validate the model. Thus, in this chapter, we will apply the CD model developed in Chapter 6 to annealing conditions and compare to experimental data of APT, which is summarized in Sec. 3.2.3, and yield stress data, which is summarized in Sec. 3.3.

7.3 Input and Parameters

The CD model for annealing requires only 4 key input parameters: a) thermal solute diffusion coefficients ($D^{th}$); b) the equilibrium solute product ($\overline{K_{sp}}$), as determined by the free energy difference between the dissolved and precipitated effective solute states or the equilibrium phase diagram; c) the MNSP-Fe interface energy (γ); and, d) the as-irradiated MNSP size distribution. The first three parameters will be taken directly from the irradiation model in Sec. 6.3, no further fitting of parameters will be made in this chapter. The as-irradiated MNSP size distribution will be estimated from the APT measurements. More details regarding how these size distributions were obtained will be illustrated in the next paragraphs.

The reason that the size distribution of precipitates cannot be taken directly from APT measurements of the as-irradiated tip is because composition varies from tip to tip, and the microstructure information depends strongly on the local composition, as discussed in Sec. 6.7, thus the size distribution obtained from the as-irradiated APT samples may not necessarily apply to the annealing samples. Therefore, we must estimate the size distribution of precipitates after irradiation for the annealing samples.

To estimate the size distribution of precipitates, one direct way would be to run the CD model under the irradiation condition before annealing. However, as mentioned in Chapter 3, the annealing experiments were done for alloys irradiated under ATR-1 condition (see Sec. 3.2.2 and Sec. 3.2.3). Based the results from Sec. 6.5, CD results under ATR-1 condition do not agree with experimental results well. Thus, it is not applicable here to estimate the size distribution of precipitates before annealing with CD model.

Therefore, here we will estimate the initial size distribution of MNSPs in the annealing samples based on the size distribution obtained from the as irradiated sample under ATR-1

condition of the same alloy. As a first step, the mole fraction of the precipitates that had formed in the sample need to estimated. Wells et al. [24] developed a correlation between precipitate individual solute mole fraction and local composition for the ATR-1 condition. The results are shown below for the readers' convenience.

$$f_{Ni} = 0.891(C_{Ni} - 0.047) \quad (7\text{-}1)$$

$$f_{Mn} = 0.801(C_{Mn} - 0.169) \text{ (very high Ni)} \quad (7\text{-}2)$$

$$f_{Mn} = 0.360(C_{Mn} + 0.320) \text{ (medium to high Ni)} \quad (7\text{-}3)$$

$$f_{Si} = 0.629(C_{Si} + 0.139) \text{ (high to very high Ni)} \quad (7\text{-}4)$$

$$f_{Si} = 0.801(C_{Si} - 0.074) \text{ (medium Ni)} \quad (7\text{-}5)$$

Here $f_{Ni}$, $f_{Mn}$ and $f_{Si}$ represents the mole fraction of Ni, Mn and Si in precipitates, respectively. And $C_{Ni}$, $C_{Mn}$ and $C_{Si}$ represents the local tip composition of Ni, Mn and Si, respectively. There are two different functions for Mn and Si depending on the local composition of Ni. In this chapter, the mole fraction of precipitates in the annealing samples will be estimated by Eqs. (6-1) - (6-5).

Then the measured size distribution of precipitates in the as-irradiated sample under ATR-1 condition will be scaled based on the ratio between mole fraction calculated from the last step and the measured mole fraction of precipitates in as-irradiated sample. The reason why it can be treated this way is illustrated as followed. Figure 7-1 shows the number density and diameter of precipitates as a function of solute composition in different tips measured by APT for CM6 alloy under ATR-1 condition, from which we can see that while the number density of precipitates increases with the bulk composition, the mean diameter of the precipitates does not change much. Thus we will assume the mean diameter as well as the shape of size distribution won't change from tip to tip. Therefore, the size distribution of precipitates can be calculated based on the mole fraction calculated from Eqs. (6-1) - (6-5).

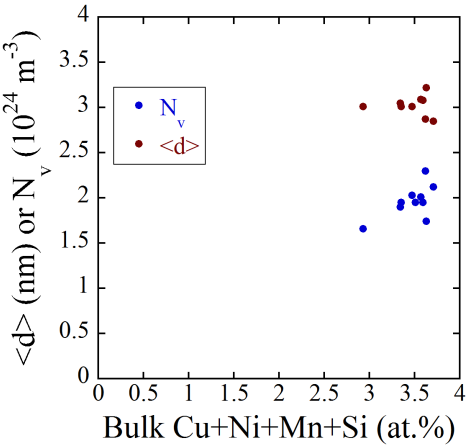


Figure 7-1 Number density and diameter of MNSPs measured by different APT tips for CM6 alloy under ATR-1 condition

## 7.4 Comparison with APT experiments

This subsection further validates the CD model of MNSPs by comparing number density, mean radius and mole fraction of precipitates between simulation and PIA results. Sec. 3.2.3 summarizes the APT experimental data under annealing condition.

Figure 7-2 shows the comparison of precipitate number density, mean radius and mole fraction between CD results and experimental data for ATR1 CM6 annealed at 400°C and 425°C, which shows good agreements between simulation results and experimental data for both number density and mean radius. The agreement for mole fraction appears less good, but all the values are less than 1%, meaning that just a few tenths of a percent error appears quite significant. Overall the agreement appears similar to that seen for the irradiated materials in Sec.6.5. One difference is that here the mole fractions all appear to over-predict those seen experimentally, with the errors usually arising from an over-prediction of both number density and particle size. The exact origin of these errors is not quite clear. One possible source is in the experimental uncertainty induced by the fact that for some cases extensive annealing leaves just a few precipitates in the tips, which can lead to significant uncertainty in the true precipitate mole fraction. Perhaps the most likely

model error is our use of a single constant composition and interfacial energy for the precipitate phases, which could couple strongly to the way the precipitates dissolve and/or coarsen.

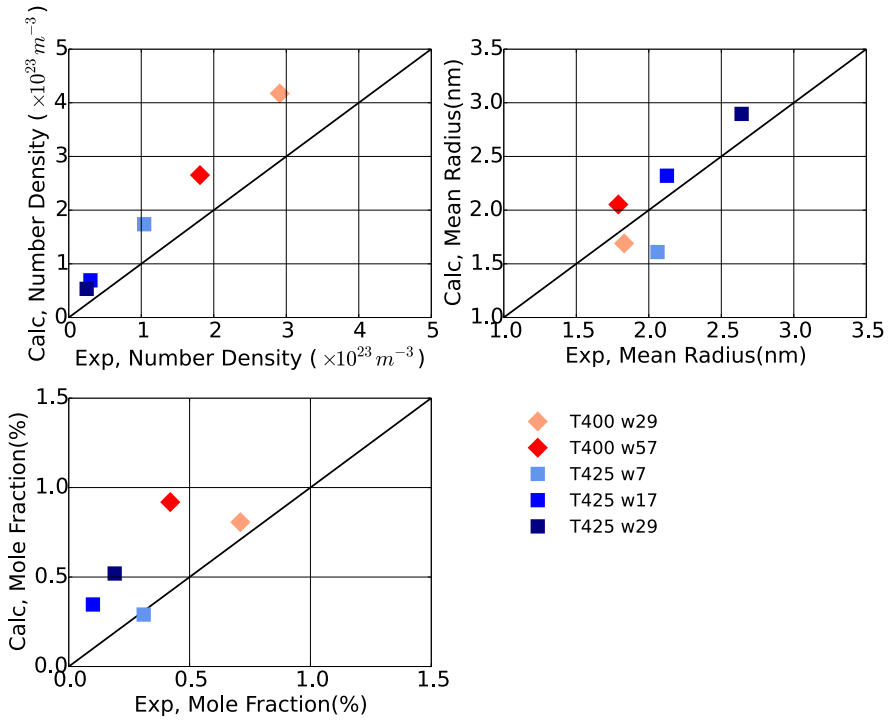


Figure 7-2 Comparison between simulation results and annealing experimental data under 400°C and 425°C

## 7.5 Comparison with Hardening data

Figure 7-3 shows the comparison of yield stress changes due to irradiation between simulation results and experimental data after annealed for 1 week under different temperatures. Yield stress changes were calculated with the same formulas as described in Sec.6.9.1. The large discrepancy between calculation results and experimental data at initial time for LG may either due to the uncertainty of the hardening model we used in Sec. 6.9.1 or due to the fact that there are other hardening mechanisms besides precipitates under irradiation which leads to higher yield stress compared to calculation results from precipitates only. As for the yield stress after annealed for 1 week, the figure shows that simulation results agree well with experimental data for higher

annealing temperature (425°C and 450°C) but predicts higher yield stress (less recovery) compared to experimental data for lower annealing temperature (350°C, 375°C and 400°C). We believe that this quantitative discrepancy between simulation results and experimental data at lower temperature is due to the recovery of defects after annealing, which is not included in the model. This defect recovery is the dominant mechanism at lower temperature, and so there is a systematic error in the model vs. experiment. While this error is still present at higher temperature, the recovery of yield stress from defects is negligible compared to that from precipitate dissolution and so the systematic error is not readily apparent.

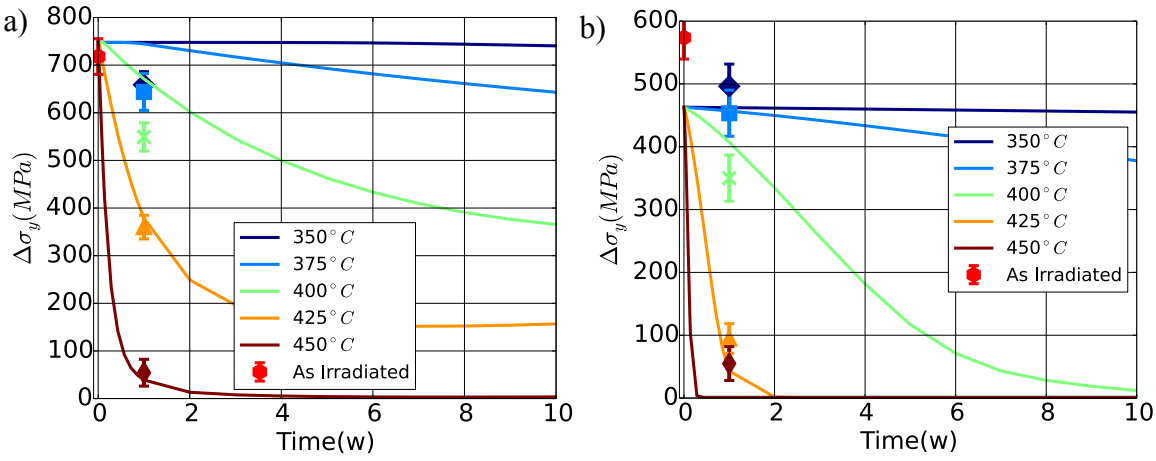


Figure 7-3 Comparison of between simulation results and experimental data under annealed at different temperatures. a) CM6; b) LG.

## 7.6 Summary

In summary, good agreements between CD results and experimental data of both microstructure results and hardening results further validates the CD model developed under irradiation condition. Although there is still some quantitative discrepancy for some conditions, for example, the over-prediction of mole fraction after longer annealing time or the over-prediction of yield stress (under-prediction of recovery) at lower annealing temperatures, multiple reasons can lead to the discrepancies.

# Chapter 8 Concluding Remarks

## 8.1 Summary and Impact of this work

A cluster dynamics model has been developed to study the evolution of Mn-Ni-Si precipitates (MNSPs) in low-Cu RPV steels, which lead to irradiation embrittlement. The model draws upon available thermodynamic and kinetic data, and includes a semi-empirical model for radiation-enhanced diffusion, including treatment of flux effects. The model also includes heterogeneous nucleation on damage created in displacement cascades. The interfacial energies for MNSPs and heterogeneous nucleation rates and nucleated cluster sizes were determined by fitting to a large body of high quality experimental APT data. The model, which was calibrated to 10 alloys (with 36 different APT tip compositions) for a range of irradiation conditions and validated to both microstructure and hardening data under post-irradiation annealing, can semi-quantitatively predict MNSPs evolution in RPV steels.

The major conclusions obtained from this study is:

1. About 1%-3% of MNSPs can form in RPV steels around 300°C at equilibrium state.
2. Two possible phases are predicted by the CALPHAD model: one is T3/G-phase ($Mn_6Ni_{16}Si_7$) and the other is T6/$\Gamma_2$ phase ($Mn(Ni,Si)_2$).
3. Gibbs-Thompson effect can decrease the mole fraction of these nm-scale MNSPs at equilibrium by a large percentage, which makes the prediction of mole fraction of precipitates even lower than what observed from experiments. It indicates either the CALPHAD database we use is not accurate enough for these dilute systems or some radiation induced precipitates form at the very high flux and very high fluence condition the ATR-1 experimental condition.

4. The driving force of the formation of MNSPs decreases as the temperature increases. Precipitates in high Ni (1.6at.%) alloy can persist up until 500°C when increasing temperature while that in medium Ni (0.7at.%) alloy can only persist up until 400°.
5. Based on *ab initio* calculations, solubility of Fe in G-phase formed in bcc Fe is less than 1.0% when substituting either Mn or Ni atom, which indicates that the large amount of Fe in MNSPs observed by APT is highly possible an artifact of APT technique.
6. A heterogeneous mechanism for nucleating MNSPs is critical to their formation, except at the high Ni contents of >1.5at.%Ni, where homogeneous nucleation dominates. Heterogeneous nucleation is not needed at sufficiently high Ni due to a larger free energy difference driving precipitation.
7. The alloy Ni content is the dominant compositional factor in forming MNSPs, while Mn and Si play lesser roles. The dominant role of Ni is due to the fact the G and $\Gamma_2$ phases respectively contain 1 and 0.8 (Mn + Si) atoms for every Ni atom, respectively.
8. The absolute threshold for G and $\Gamma_2$ MNSPs formation appears to be ≈ 0.5at.%Ni.
9. The model suggests that MNSPs in low Cu alloys in RPVs are in a nucleation and growth stage in present reactors, with significantly more hardening and associated temperature shifts expected during life-extension.
10. As an illustrative example, at an extended life fluence of $10^{24}$n·m$^{-2}$ typical RPV steels with 1.0at.%Ni and 1.6at.%Ni are predicted to contain $f_V \approx 0.2\%$ and 0.9% MNSPs that are capable of producing $\Delta T \approx 80$°C and 250°C, respectively.

11. The mole fractions of MNSPs under very high flux at very high fluence (ATR-1) observed from experiments are even higher than the value predicted by CALPHAD model at equilibrium without considering Gibbs-Thomson effect. Thus even with cascade enhanced nucleation, the CD model under-predicted the mole fraction of MNSPs in this case. This suggests that unmodeled other physics, like influence of small amounts of Cu, or segregation resulting in precipitation on small dislocation loops, may play a significant role under this extreme condition.
12. The MNSP mole fraction of medium Ni steels (BR2-TU, BR2-G1 LG and Ginna) are under predicted compared to experiments. The differences may again be due to either thermodynamic model inaccuracies, or un-modeled physics.

The model can be used to interpolate and extrapolate the experimental database on RPV steels, which is both sparse and not well distributed in the high dimensional space of potentially relevant variables. The CD models also provide a foundation for more realistic but complex models, e.g., including Cu and MNSPs, and simpler, but still physical, reduced order models like Avrami-based treatments of the MNSPs evolution as a function of fluence.

## 8.2 Suggestions for future work

The major deficiency in the CD model is for alloys with very high flux and very high fluence (ATR-1), where MNSPs are either under predicted, or do not form, in contrast to experimental observations. In part this is due to the fact that the model under-predicts MNSP formation in the alloys studied here with medium Ni contents around 0.8 wt.%, and comparison to a wider body of data not considered in this work supports that this is a general trend. There are multiple reasons that can lead to this discrepancy, either the thermodynamics of dilute system at low temperature is not accurate enough, or the extreme condition (very high flux and very high fluence) of ATR-1

modifies the local thermodynamic environment in and around cascades. The reason can be further investigated in future work.

Although Cu is not included in the present model, it will serve as a foundation for future modeling of Cu-Mn-Ni-Si precipitation in Cu bearing RPV steels. Further, many simplifications and approximations in the current CD will be improved and additional physics included, especially treating nucleation in a more rigorous fashion. Finally, these detailed physics-based models will guide reduced order model, but still physically based, correlation equations fit to the actual surveillance and test reactor databases. Ultimately, the more detailed models themselves might be fit these databases to provide an even more detailed physical basis for embrittlement prediction interpolation and extrapolation.

# Chapter 9 Reference


[1] US Nuclear Generating Statistics, (2016). http://www.nei.org/Knowledge-Center/Nuclear-Statistics/US-Nuclear-Power-Plants/US-Nuclear-Generating-Statistics.

[2] S. Chu, A. Majumdar, Opportunities and challenges for a sustainable energy future, Nature. 488 (2012) 294–303. doi:10.1038/nature11475.

[3] Country Statistics - United States of America, IAEA - Int. At. Energy Agency. (2015). https://www.iaea.org/PRIS/CountryStatistics/CountryDetails.aspx?current=US (accessed October 10, 2016).

[4] EU Comission, Technology Roadmap, 2015. doi:10.1007/SpringerReference_7300.

[5] J. Busby, Expanded materials degradation assessment volume 1 : Executive summary of EMDA process and results, 1 (2013).

[6] J.T. Busby, P.G. Oberson, C.E. Carpenter, M. Srinivasan, Expanded Materials Degradation Assessment ( EMDA ) Volume 3 : Aging of Reactor Pressure Vessels, 2013.

[7] J.T. Busby, P.G. Oberson, C.E. Carpenter, M. Srinivasan, Expanded Materials Degradation Assessment (EMDA) Volume 2: Aging of Core Internals and Piping Systems, 2014.

[8] J.T. Busby, P.G. Oberson, C.E. Carpenter, M. Srinivasan, Expanded Materials Degradation Assessment ( EMDA ) Volume 4 : Aging of Concrete and Civil Structures, 2013.

[9] J.T. Busby, P.G. Oberson, C.E. Carpenter, M. Srinivasan, Expanded Materials Degradation Assessment ( EMDA ) Volume 5 : Aging of Cables and Cable Systems, 2013.

[10] G. Odette, G. Lucas, Embrittlement of nuclear reactor pressure vessels, JOM J. Miner. Met. Mater. Soc. 53 (2001) 18–22.

[11] Integrity of reactor pressure vessels in nuclear power plants: assessment of irradiation embrittlement effects in reactor pressure vessel steels, report no NP-T-3.11, Vienna, 2009.

[12] W.L. Server, R.K. Nanstad, Reactor pressure vessel (RPV) design and fabrication: the case of the USA, Irradiat. Embrittlement React. Press. Vessel. Nucl. Power Plants. (2015) 3–25. doi:http://dx.doi.org/10.1533/9780857096470.1.3.

[13] J.E. Zelenty, Understanding thermally induced embrittlement in low copper RPV steels utilising atom probe tomography, Mater. Sci. Technol. 31 (2015) 981–988. doi:10.1179/1743284714Y.0000000718.

[14] G.R. Odette, R.K. Nanstad, Predictive Reactor Pressure Vessel Steel Irradiation Embrittlement Models : Issues and Opportunities, JOM J. Miner. Met. Mater. Soc. 61 (2009) 17–23.

[15] NRC, Radiation Embrittlement of Reactor Vessel Materials, Regulatory Guide 1.99 Revision 2, Office of Nuclear Regulatory Research, US Nuclear Regulatory Commission, Washington, D. C., 1998.

[16] G.R. Odette, Radiation Induced Microstructural Evolution in Reactor Pressure Vessel Steels, Microstruct. Irradiat. Mater. Symp. Proc. 373 (1995) 137–148. doi:10.1557/PROC-373-137.

[17] G.R. Odette, G.E. Lucas, Recent progress in understanding reactor pressure vessel steel embrittlement, Radiat. Eff. Defects Solids. 144 (1998) 189–231. doi:10.1080/10420159808229676.

[18] C.L. Liu, G.R. Odette, B.D. Wirth, G.E. Lucas, A lattice Monte Carlo simulation of nanophase compositions and structures in irradiated pressure vessel Fe-Cu-Ni-Mn-Si steels, Mater. Sci. Eng. A. 238 (1997) 202–209.

[19] G.R. Odette, B.D. Wirth, A computational microscopy study of nanostructural evolution in

irradiated pressure vessel steels, J. Nucl. Mater. 251 (1997) 157–171. doi:10.1016/S0022-3115(97)00267-5.

[20] G. Odette, On the dominant mechanism of irradiation embrittlement of reactor pressure vessel steels, Scr. Metall. 17 (1983) 1183–1188.

[21] J.M. Hyde, G. Sha, E. a Marquis, a Morley, K.B. Wilford, T.J. Williams, A comparison of the structure of solute clusters formed during thermal ageing and irradiation., Ultramicroscopy. 111 (2011) 664–71. doi:10.1016/j.ultramic.2010.12.030.

[22] P.D. Styman, J.M. Hyde, K. Wilford, a. Morley, G.D.W. Smith, Precipitation in long term thermally aged high copper, high nickel model RPV steel welds, Prog. Nucl. Energy. 57 (2012) 86–92. doi:10.1016/j.pnucene.2011.10.010.

[23] M.K. Miller, K.F. Russell, Embrittlement of RPV steels: An atom probe tomography perspective, J. Nucl. Mater. 371 (2007) 145–160. doi:10.1016/j.jnucmat.2007.05.003.

[24] P.B. Wells, T. Yamamoto, B. Miller, T. Milot, J. Cole, Y. Wu, et al., Evolution of manganese-nickel-silicon-dominated phases in highly irradiated reactor pressure vessel steels, Acta Mater. 80 (2014) 205–219. doi:10.1016/j.actamat.2014.07.040.

[25] G.R. Odette, T. Yamamoto, D. Klingensmith, The Effect of Dose Rate on Irradiation Hardening of RPV Steels: A Comprehensive Single Variable Database and Model Based Analysis, Washington, D. C., 2003.

[26] P. Auger, P. Pareige, M. Akamatsu, J.-C. Van Duysen, Microstructural characterization of atom clusters in irradiated pressure vessel steels and model alloys, J. Nucl. Mater. 211 (1994) 194–201. doi:10.1016/0022-3115(94)90347-6.

[27] P. Auger, P. Pareige, M. Akamatsu, D. Blavette, APFIM investigation of clustering in neutron-irradiated FeCu alloys and pressure vessel steels, J. Nucl. Mater. 225 (1995) 225–230.

[28] P. Auger, P. Pareige, S. Welzel, J.-C. Van Duysen, Synthesis of atom probe experiments on irradiation-induced solute segregation in French ferritic pressure vessel steels, J. Nucl. Mater. 280 (2000) 331–344. doi:10.1016/S0022-3115(00)00056-8.

[29] G.R. Odette, C.L. Liu, B.D. Wirth, Microstructural Evolution During Irradiation, in: Mater. Res. Soc. Symp. Proc., 1998: p. 457.

[30] G.R. Odette, T. Yamamoto, W. D., Late blooming phases and dose rate effects in RPV steels: integrated experiments and models, in: N.M. Ghoniem (Ed.), Proc. Second Int. Conf. Multiscale Mater. Model., Los Angeles, 2004: p. 355.

[31] M. Miller, M. Sokolov, R. Nanstad, K. Russell, APT characterization of high nickel RPV steels, J. Nucl. Mater. 351 (2006) 187–196. doi:10.1016/j.jnucmat.2006.02.013.

[32] M.K. Miller, A.A. Chernobaeva, Y.I. Shtrombakh, K.F. Russell, R.K. Nanstad, D.Y. Erak, et al., Evolution of the nanostructure of VVER-1000 RPV materials under neutron irradiation and post irradiation annealing, J. Nucl. Mater. 385 (2009) 615–622. doi:10.1016/j.jnucmat.2009.01.299.

[33] M.K. Miller, K. a. Powers, R.K. Nanstad, P. Efsing, Atom probe tomography characterizations of high nickel, low copper surveillance RPV welds irradiated to high fluences, J. Nucl. Mater. 437 (2013) 107–115. doi:10.1016/j.jnucmat.2013.01.312.

[34] P.D. Edmondson, M.K. Miller, K.A. Powers, R.K. Nanstad, Atom probe tomography characterization of neutron irradiated surveillance samples from the R. E. Ginna reactor pressure vessel, J. Nucl. Mater. 470 (2016) 147–154. doi:10.1016/j.jnucmat.2015.12.038.

[35] R. Ngayam-Happy, C.S. Becquart, C. Domain, L. Malerba, Formation and evolution of MnNi clusters in neutron irradiated dilute Fe alloys modelled by a first principle-based

AKMC method, J. Nucl. Mater. 426 (2012) 198–207. doi:10.1016/j.jnucmat.2012.03.033.
[36] R. Ngayam-Happy, C.S. Becquart, C. Domain, First principle-based AKMC modelling of the formation and medium-term evolution of point defect and solute-rich clusters in a neutron irradiated complex Fe–CuMnNiSiP alloy representative of reactor pressure vessel steels, J. Nucl. Mater. 440 (2013) 143–152. doi:10.1016/j.jnucmat.2013.04.081.
[37] C. Pareige, V. Kuksenko, P. Pareige, Behaviour of P, Si, Ni impurities and Cr in self ion irradiated Fe-Cr alloys - Comparison to neutron irradiation, J. Nucl. Mater. 456 (2015) 471–476. doi:10.1016/j.jnucmat.2014.10.024.
[38] V. Kuksenko, C. Pareige, C. Genevois, P. Pareige, Characterisation of Cr, Si and P distribution at dislocations and grain-boundaries in neutron irradiated Fe-Cr model alloys of low purity, J. Nucl. Mater. 434 (2013) 49–55. doi:10.1016/j.jnucmat.2012.11.027.
[39] V. Kuksenko, C. Pareige, P. Pareige, Cr precipitation in neutron irradiated industrial purity Fe-Cr model alloys, J. Nucl. Mater. 432 (2013) 160–165. doi:10.1016/j.jnucmat.2012.07.021.
[40] V. Kuksenko, C. Pareige, C. Genevois, F. Cuvilly, M. Roussel, P. Pareige, Effect of neutron-irradiation on the microstructure of a Fe-12at.%Cr alloy, J. Nucl. Mater. 415 (2011) 61–66. doi:10.1016/j.jnucmat.2011.05.042.
[41] M. Bachhav, G. Robert Odette, E. a. Marquis, Microstructural changes in a neutron-irradiated Fe-15 at.%Cr alloy, J. Nucl. Mater. 454 (2014) 381–386. doi:10.1016/j.jnucmat.2014.08.026.
[42] M. Bachhav, L. Yao, G. Robert Odette, E. a. Marquis, Microstructural changes in a neutron-irradiated Fe-6 at.%Cr alloy, J. Nucl. Mater. 453 (2014) 334–339. doi:10.1016/j.jnucmat.2014.06.050.
[43] E. Meslin, B. Radiguet, M. Loyer-Prost, Radiation-induced precipitation in a ferritic model alloy: An experimental and theoretical study, Acta Mater. 61 (2013) 6246–6254. doi:10.1016/j.actamat.2013.07.008.
[44] L. Messina, Multiscale modeling of atomic transport phenomena in ferritic steels, KTH Royal Institute of Technology, 2015.
[45] E. Vincent, C. Becquart, C. Domain, Microstructural evolution under high flux irradiation of dilute Fe–CuNiMnSi alloys studied by an atomic kinetic Monte Carlo model accounting for both vacancies and self interstitials, J. Nucl. Mater. 382 (2008) 154–159. doi:10.1016/j.jnucmat.2008.08.019.
[46] W. Xiong, H. Ke, R. Krishnamurthy, P. Wells, L. Barnard, G.R. Odette, et al., Thermodynamic models of low-temperature Mn–Ni–Si precipitation in reactor pressure vessel steels, MRS Commun. 4 (2014) 101–105. doi:10.1557/mrc.2014.21.
[47] D.J. Sprouster, J. Sinsheimer, E. Dooryhee, S.K. Ghose, P. Wells, T. Stan, et al., Structural characterization of nanoscale intermetallic precipitates in highly neutron irradiated reactor pressure vessel steels, Scr. Mater. 113 (2016) 18–22. doi:10.1016/j.scriptamat.2015.10.019.
[48] P.B. Wells, H. Ke, P. Edmondson, N. Almirall, D. Morgan, T. Yamamoto, et al., On the Thermal Stability of Mn-Ni-Si Precipitates Formed in Highly Irradiated Reactor Pressure Vessel Steels, In Preparation. (2017).
[49] L. Messina, M. Chiapetto, C. Becquart, L. Malerba, An object kinetic Monte Carlo model for the microstructure evolution of neutron-irradiated reactor pressure vessel steels, Phys. Status Solidi A. 213 (2016) 2974–2980. doi:10.1002/pssa.201600038.
[50] L. Ratke, P.W. Voorhees, Growth and Coarsening: Ostwald Ripening in Material Processing, Springer Science & Business Media, 2013.

[51] R. Sear, Formation energy of a nucleus as a function of radius, (n.d.). https://commons.wikimedia.org/w/index.php?curid=30549437.
[52] M.F. Ashby, H. Shercliff, D. Cebon, Materials: Engineering, Science, Processing and Design, Butterworth-Heinemann, 2007.
[53] J. Friedel, Electron Microscopy and the Strength of Crystals, John Wiley & sons, New York, 1962.
[54] A. Wagner, F. Bergner, R. Chaouadi, H. Hein, M. Hernández-Mayoral, M. Serrano, et al., Effect of neutron flux on the characteristics of irradiation-induced nanofeatures and hardening in pressure vessel steels, Acta Mater. 104 (2016) 131–142. doi:10.1016/j.actamat.2015.11.027.
[55] A.K. Seeger, Theory of radiation damage and radiation hardening, in: Proc. Second UN Conf. Peac. Uses At. Energy 6, New York, United Nations, 1958: pp. 250–273.
[56] D.J. Bacon, U.F. Kocks, R.O. Scattergood, The effect of dislocation self-interaction on the orowan stress, Philos. Mag. 28 (1973) 1241–1263. doi:10.1080/14786437308227997.
[57] K.C. Russell, L.M. Brown, A dispersion strengthening model based on differing elastic moduli applied to the Iron-Copper system, Acta Mater. 20 (1972) 969–974. doi:10.1016/0001-6160(72)90091-0.
[58] S.J. Zinkle, Y. Matsukawa, Observation and analysis of defect cluster production and interactions with dislocations, J. Nucl. Mater. 329–333 (2004) 88–96. doi:10.1016/j.jnucmat.2004.04.298.
[59] F. Kroupa, P.B. Hirsch, Elastic Interaction Between Prismatic Dislocation Loops and Straight Dislocations, Disc. Faraday Soc. 38 (1964) 49–55.
[60] A. Deschamps, M. Perez, Mesoscopic modelling of precipitation: A tool for extracting physical parameters of phase transformations in metallic alloys, Comptes Rendus Phys. 11 (2010) 236–244. doi:10.1016/j.crhy.2010.07.005.
[61] R. Kampmann, R. Wagner, KINETICS OF PRECIPITATION IN METASTABLE BINARY ALLOYS -THEORY AND APPLICATION TO Cu-1.9 at % Ti AND Ni-14 at % Al, Acta Metallurgica Inc., 1984. doi:10.1016/B978-0-08-031651-2.50018-5.
[62] M. Volmer, A. Weber, No Keimbildung in übersättigen gebilden, Zeitschrift Für Phys. Chemie. 119 (1926) 277–301.
[63] K.C. Russell, Phase Transformations, in: H.I. Aaronson (Ed.), Am. Soc. Met., Metals Park, 1968: pp. 219–268.
[64] R. Becker, W. Döring, Kinetische Behandlung der Keimbildung in übersättigten Dämpfen, Ann. Phys. 416 (1935) 719–752. doi:10.1002/andp.19354160806.
[65] M. Perez, M. Dumont, D. Acevedo-Reyes, Implementation of classical nucleation and growth theories for precipitation, Acta Mater. 56 (2008) 2119–2132. doi:10.1016/j.actamat.2007.12.050.
[66] C. Zener, Theory of growth of spherical precipitates from solid solution, J. Appl. Phys. 20 (1949) 950–953. doi:10.1063/1.1698258.
[67] I.M. Lifshitz, V.V. Slyozov, The kinetics of precipitation from supersaturated solid solutions, J. Phys. Chem. Solids. 19 (1961) 35–50. doi:10.1016/0022-3697(61)90054-3.
[68] C. Wagner, Theory of precipitate change by redissolution, Zeitschrift Fuer Elektrochemie Und Angew. Phys. Chemie. 65 (1961) 581–591.
[69] E.E. Finney, R.G. Finke, Nanocluster nucleation and growth kinetic and mechanistic studies: A review emphasizing transition-metal nanoclusters, J. Colloid Interface Sci. 317 (2008) 351–374. doi:10.1016/j.jcis.2007.05.092.

[70] J.W.P. Schmelzer, A.S. Abyzov, J. Moller, Nucleation versus spinodal decomposition in phase formation processes in multicomponent solutions, J. Chem. Phys. 121 (2004) 6900–6917.
[71] J.W.P. Schmelzer, A new approach to nucleation theory and its application to phase formation processes in glass-forming melts, Phys. Chem. Glas. 45 (2004) 116–120.
[72] J.W.P. Schmelzer, A.R. Gokhman, V.M. Fokin, Dynamics of first-order phase transitions in multicomponent systems: a new theoretical approach, J. Colloid Interface Sci. 272 (2004) 109–133.
[73] V. V. Slezov, Kinetics of first order phase transitions, Wiley-VCH, Berlin, 2009.
[74] S.M. Allen, Ground state structures in ordered binary neighbor interactions*, Acta Metall. 20 (1972) 423. doi:10.1016/0001-6160(72)90037-5.
[75] J. Cahn, S. Allen, A microscopic theory for domain wall motion and its experimental verification in Fe-Al alloy domain growth kinetics, Le J. Phys. …. (1977) 51–54. doi:10.1051/jphyscol:1977709.
[76] J.W. Cahn, J.E. Hilliard, Free Energy of a Nonuniform System. I. Interfacial Free Energy, J. Chem. Phys. 28 (1958) 258–267. doi:10.1063/1.1744102.
[77] J.W. Cahn, On spinodal decomposition, Acta Metall. 9 (1961) 795–801. doi:10.1016/0001-6160(61)90182-1.
[78] L.-Q. Chen, Phase-Field Models for Microstructure Evolution, Annu. Rev. Mater. Res. 32 (2002) 113–140. doi:10.1146/annurev.matsci.32.112001.132041.
[79] R.S. Qin, H.K. Bhadeshia, Phase field method, Mater. Sci. Technol. 26 (2010) 803–811. doi:10.1179/174328409X453190.
[80] N. Saunders, CALPHAD (Calculation of Phase Diagrams) A Comprehensive Guide, Burlington : Elsevier Science, 1998., 1998.
[81] J.O. Andersson, T. Helander, L. Höglund, P. Shi, B. Sundman, Thermo-Calc & DICTRA, computational tools for materials science, Calphad Comput. Coupling Phase Diagrams Thermochem. 26 (2002) 273–312. doi:10.1016/S0364-5916(02)00037-8.
[82] CompuTherm, (n.d.). http://www.computherm.com/ (accessed November 17, 2016).
[83] MatCalc, (n.d.). http://matcalc.tuwien.ac.at/ (accessed November 17, 2016).
[84] The TCS Al-based alloy database, TCAL2. Version 2.0. Stockholm: Thermo-Calc SofAB; 2013, The TCS Al-Based Alloy Database, TCAL2. Version 2.0. Stockholm: Thermo-Calc Software AB; (2013).
[85] W. Kohn, L.J. Sham, Self-consistent equations including exchange and correlation effects, Phys. Rev. 140 (1965) 1133–1138. doi:10.1103/PhysRev.140.A1133.
[86] P. Hohenberg, W. Kohn, Inhomogeneous electron gas, Phys. Rev. B. 136 (1964) 864–871. doi:10.1103/PhysRevB.7.1912.
[87] G. Kresse, J. Furthmüller, Efficient iterative schemes for ab initio total-energy calculations using a plane-wave basis set., Phys. Rev. B. Condens. Matter. 54 (1996) 11169–11186.
[88] G. Kresse, J. Hafner, Ab initio molecular dynamics for liquid metals, Phys. Rev. B. 47 (1993) 558–561.
[89] G. Kresse, J. Furthmüller, Efficiency of ab-initio total energy calculations for metals and semiconductors using a plane-wave basis set, Comput. Mater. Sci. 6 (1996) 15–50. doi:10.1016/0927-0256(96)00008-0.
[90] G. Kresse, J. Hafner, Ab initio molecular-dynamics simulation of the liquid-metal–amorphous-semiconductor transition in germanium, Phys. Rev. B. 49 (1994) 14251–14269. doi:10.1103/PhysRevB.49.14251.

[91] J.P. Perdew, A. Zunger, Self-interaction correction to density-functional approximations for many-electron systems, Phys. Rev. B. 23 (1981) 5048–5079. doi:10.1103/PhysRevB.23.5048.
[92] D.C. Langreth, J.P. Perdew, Theory of nonuniform electronic systems. I. Analysis of the gradient apporoximation and a generalization that works, 21 (1980).
[93] C. Domain, C. Becquart, Ab initio calculations of defects in Fe and dilute Fe-Cu alloys, Phys. Rev. B. 65 (2001) 1–14. doi:10.1103/PhysRevB.65.024103.
[94] G. Bonny, D. Terentyev, E.E. Zhurkin, L. Malerba, Monte Carlo study of decorated dislocation loops in FeNiMnCu model alloys, J. Nucl. Mater. 452 (2014) 486–492. doi:10.1016/j.jnucmat.2014.05.051.
[95] J. Kočík, E. Keilová, J. Čížek, I. Procházka, TEM and PAS study of neutron irradiated VVER-type RPV steels, J. Nucl. Mater. 303 (2002) 52–64. doi:10.1016/S0022-3115(02)00800-0.
[96] B. a. Gurovich, E. a. Kuleshova, Y.I. Shtrombakh, D.Y. Erak, a. a. Chernobaeva, O.O. Zabusov, Fine structure behaviour of VVER-1000 RPV materials under irradiation, J. Nucl. Mater. 389 (2009) 490–496. doi:10.1016/j.jnucmat.2009.02.002.
[97] E.A. Kuleshova, B.A. Gurovich, Y.I. Shtrombakh, D.Y. Erak, O. V Lavrenchuk, Comparison of microstructural features of radiation embrittlement of VVER-440 and VVER-1000 reactor pressure vessel steels, J. Nucl. Mater. 300 (2002) 127–140.
[98] K. Fujii, K. Fukuya, N. Nakata, K. Hono, Y. Nagai, M. Hasegawa, Hardening and microstructural evolution in A533B steels under high-dose electron irradiation, J. Nucl. Mater. 340 (2005) 247–258. doi:10.1016/j.jnucmat.2004.12.008.
[99] T. Hamaoka, Y. Satoh, H. Matsui, One-dimensional motion of self-interstitial atom clusters in A533B steel observed using a high-voltage electron microscope, J. Nucl. Mater. 399 (2010) 26–31. doi:10.1016/j.jnucmat.2009.12.014.
[100] E.D. Eason, G.R. Odette, R.K. Nanstad, T. Yamamoto, A physically-based correlation of irradiation-induced transition temperature shifts for RPV steels, J. Nucl. Mater. 433 (2013) 240–254. doi:10.1016/j.jnucmat.2012.09.012.
[101] E.D. Eason, G.R. Odette, R.K. Nanstad, T. Yamamoto, A Physically Based Correlation of Irradiation-Induced Transition Temperature Shifts for RPV Steels, Oak Ridge, 2007. doi:10.2172/941022.
[102] G.R. Odette, T. Yamamoto, D. Klingensmith, On the effect of dose rate on irradiation hardening of RPV steels, Philos. Mag. 85 (2005) 779–797. doi:10.1080/14786430412331319910.
[103] G.R. Odette, T. Yamamoto, E.D. Eason, R.K. Nanstad, On the metallurgical and irradiation variable dependence of the embrittlement of RPV steels: converging physically based predictions and critical unresolved issues, in: Proc. Res. Aging Manag. Light Water React. Its Futur. Trend, Inst. Nucl. Saf. Syst., Tsuruga City, Japan, 2007: pp. 279–307.
[104] L.T. Stephenson, M.P. Moody, P.V. Liddicoat, S.P. Ringer, New techniques for the analysis of fine-scaled clustering phenomena within atom probe tomography (APT) data., Microsc. Microanal. 13 (2007) 448–463. doi:10.1017/S1431927607070900.
[105] K.P. Gupta, The Mn-Ni-Si (Manganese-Nickel-Silicon) System, J. Phase Equilibria Diffus. 27 (2006) 529–534. doi:10.1361/154770306X136520.
[106] B. Hu, H. Xu, S. Liu, Y. Du, C. He, C. Sha, et al., Experimental investigation and thermodynamic modeling of the Mn–Ni–Si system, Calphad. 35 (2011) 346–354. doi:10.1016/j.calphad.2011.05.001.

[107] G. Bonny, D. Terentyev, a. Bakaev, E.E. Zhurkin, M. Hou, D. Van Neck, et al., On the thermal stability of late blooming phases in reactor pressure vessel steels: An atomistic study, J. Nucl. Mater. 442 (2013) 282–291. doi:10.1016/j.jnucmat.2013.08.018.
[108] P. Blöchl, Projector augmented-wave method, Phys. Rev. B. 50 (1994).
[109] G. Kresse, D. Joubert, From ultrasoft pseudopotentials to the projector augmented-wave method, Phys. Rev. B. 59 (1999) 11–19.
[110] J. Perdew, K. Burke, M. Ernzerhof, Generalized Gradient Approximation Made Simple., Phys. Rev. Lett. 77 (1996) 3865–3868.
[111] J.P. Perdew, K. Burke, M. Ernzerhof, Generalized Gradient Approximation Made Simple-ERRATA, Phys. Rev. Lett. 78 (1997) 1396.
[112] H.J. Monkhorst, J.D. Pack, special points for Brillouin-zone integrations, Phys. Rev. B. 13 (1976) 5188–5192. doi:10.1103/PhysRevB.16.1748.
[113] G. Bergman, J.L.T. Waugh, The crystal structure of the intermetallic compound Mg 6 Si 7 Cu 16, Acta Crystallogr. 6 (1953) 93–94. doi:10.1107/S0365110X53000223.
[114] L. Ruch, D.R. Sain, H.L. Yeh, L.A. Girifalco, Analysis of diffusion in ferromagnets, J. Phys. Chem. Solids. 37 (1976) 649–653. doi:10.1016/0022-3697(76)90001-9.
[115] H.H. Potter, The magneto-Caloric effect and other magnetic phenomena in Iron, (n.d.). doi:10.1098/rspa.1983.0054.
[116] D.W. James, G.M. Leak, Self-diffusion and diffusion of cobalt in alpha and delta-iron, Philos. Mag. 14 (1966) 701–713. doi:10.1080/14786436608211966.
[117] G. Hettich, H. Mehrer, K. Maier, Self-diffusion in ferromagnetic α-iron, Scr. Metall. II (1977) 795–802.
[118] Y. Iijima, K. Kimura, K. Hirano, SELF-DIFFUSION AND ISOTOPE EFFECT IN a-IRON, Acta Metall. 36 (1988) 2811–2820.
[119] F.S. Buffington, K. Hirano, M. Cohen, Self diffusion in iron, Acta Metall. 9 (1961) 434–439. doi:10.1016/0001-6160(61)90137-7.
[120] D. Graham, Mass dependence of self-diffusion in iron, J. Appl. Phys. 40 (1969) 2386–2390. doi:10.1063/1.1658000.
[121] J. Bernardini, The role of solute segregation in grain boundary diffusion, Proc. R. Soc. Lond. A. Math. Phys. Sci. 379 (1982) 159–178.
[122] M. Lubbehusen, H. Mehrer, Self-diffusion in α-iron: The influence of dislocations and the effect of the magnetic phase transition, Acta Metall. Mater. 38 (1990) 283–292. doi:10.1016/0956-7151(90)90058-O.
[123] K. Nohara, K. Hirano, Diffusion of Mn(54) in iron and iron-manganese alloys, in: Int. Conf. Sci. Technol. Iron Steels, Vol. 7 Iron Steel Inst. Japan, 1971: p. 1267.
[124] K. Hirano, M. Cohen, B.L. Averbach, Diffusion of Ni into Iron, Acta Metall. 9 (1961) 440–445. doi:10.1039/c1pp05319a.
[125] L. Messina, M. Nastar, T. Garnier, C. Domain, P. Olsson, Exact ab initio transport coefficients in bcc Fe−X (X=Cr, Cu, Mn, Ni, P, Si) dilute alloys, Phys. Rev. B. 90 (2014) 1–15. doi:10.1103/PhysRevB.90.104203.
[126] L. Messina, M. Nastar, N. Sandberg, P. Olsson, Systematic electronic-structure investigation of substitutional impurity diffusion and flux coupling in bcc iron, Phys. Rev. B - Condens. Matter Mater. Phys. 93 (2016) 1–18. doi:10.1103/PhysRevB.93.184302.
[127] R.J. Borg, Diffusion in α-Fe[Single Bond]Si Alloys, J. Appl. Phys. 41 (1970) 5193. doi:10.1063/1.1658644.
[128] F. Christien, Modelling of copper precipitation in iron during thermal aging and irradiation,

J. Nucl. Mater. 324 (2004) 90–96. doi:10.1016/j.jnucmat.2003.08.035.
[129] B. Gault, M.P. Moody, J.M. Caimey, S.P. Ringer, Atom probe microscopy, Springer New York Heidelber Dordrecht London, New York, 2012.
[130] M.A. Sokolov, R.K. Nanstad, Comparison of irradiation-induced shifts of KJc and Charpy impact toughness for reactor pressure vessel steels, in: R.K. Nanstad, M.L. Hamilton, F.A. Garner, A.S. Kumar (Eds.), Eff. Radiat. Mater. 18th Int. Symp. ASTM STP 1325, West Conshohocken, PA, 1999: p. 167.
[131] G.R. Odette, M.Y. He, Cleavage toughness master curve model, J. Nucl. Mater. 283–287 (2000) 120–127. doi:10.1016/S0022-3115(00)00334-2.